Analysis of antenna transient radiation

Pablo Rodriguez Ulibarri

August, 2010
Supervisors: Prof. Alexander Yarovoy
Dr. Diego Caratelli

International Research Centre for Telecommunications and Radar
Department of Electrical Engineering
Delft University of Technology
P.O. Box 5031, 2600 GA Delft
The Netherlands

Abstract

Recently a new formalism has been developed for modeling time domain radiation processes in complex antennas. Using this formalism the radiated electromagnetic field can be expressed in terms of non uniform spherical wave contributions relevant to the resonant phenomena occurring in the structure. The developed algorithm consists of a dedicated two-step vector fitting procedure. Firstly, the spherical harmonic expansion of the time-domain equivalent electric and magnetic currents is performed. Then, by using the Singularity-Expansion-Method (SEM), the time-variant spherical harmonic expansion coefficients are represented in terms of dumped exponential terms. In this way, by using the incomplete modified spherical Bessel functions, an analytical description of the transient wave radiation phenomena is achieved. In this study several canonical radiating structures such as dipole, bow-tie and loop antennas, have been analyzed using the afore-mentioned formalism in order to gain a physical insight into the natural resonant processes occurring in the antenna and find a relation with the relevant geometrical characteristics.

Acknowledgements

After all this year a lot of people have contributed in a certain way to this thesis work. Firstly, I would like to thank my supervisor, Prof. Alexander Yarovoy, and tutor, Dr. Diego Caratelli for all the support given to me. I would like to thank Alexander for giving me the opportunity to work in this project as well as all his trust, enthusiasm and knowledge put in this project. I also would like to thank Diego all his help and support with the numerical procedure specially with all the difficulties experienced during my work. I could not forget his dedication and time spent in the debugging procedure of the algorithm. I would like to express my gratitude to them for letting me no surrender to the difficulties.

I could not forget my fellows from the 22nd floor, specially Hussein,Mark and Wyger. I will always appreciate your warm welcoming and the chatting during lunch-time and breaks. I strongly believe that it would be much more difficult to carry out this work without people like you. I also would like to thank every IRCTR member and specially to the secretary staff that have always been helpful in all my requests and doubts.

It would not be fair if I did not mention the CST support team. Specially I must thank to Mr. Tallini and Mr. Hanninen for his helpful and always kind replies.

Finally, apart from the technical and scientific field, I can not forget the emotional support given by my parents and brothers: Fernando and Javier. Thank you for your unlimited love and being the main reason for coming back home. I would like to extent this gratitude to all my family and friends.

The only true wisdom is in knowing you know nothing.
Socrates

Contents

List of Figures

List of Tables

Chapter 1

Introduction

1.1 Summary

Transient radiation (radiation in time domain) of antennas has been studied by some researchers in electromagnetism field. For a number of basic antennas transient radiation has been simulated and measured. At the same time a fully analysis of transient radiation has not been done so far. Recently a new formalism has been developed by the IRCTR modeling time-domain radiation in complex antennas. Using this formalism, the antenna complex resonator frequencies can be determined from analysis of the near-field transient radiation. Relation between these complex resonant frequencies and antenna geometry, dimensions and environment is not clear at the moment. In this research project analysis of transient radiation from a number of classical antennas including a dipole, bow-tie and loop antenna is performed. Complex resonant frequencies should be determined and related to antenna geometry and dimensions. In order to achieve this goal, basic antennas has been analyzed carefully such as dipole antenna. By changing some parameters as the length of the arm and the radius of the wire, differences in the complex resonant frequencies should be observed.

1.2 Motivation

Ultra-Wide Band (UWB) is a promising technology for many wireless applications due to its large bandwidth, good ratio of transmission data and low power cost. Typically, the study of UWB antennas radiation has been done in the frequency domain. Generally, the antenna radiation is described as a set of patterns at different frequencies, but this does not provide a physical insight understanding of the origin of the radiation. Therefore, a wide study of the complex radiation processes occurring in the structure will provide us a better understanding and the chance to relate the complex resonant frequencies to the geometry and dimensions of different antennas. Furthermore, thinking about a series of three-dimensional radiation patterns over a large frequency band, the study in frequency domain will require large computational resources and storage of a large amount of data. Another motivation for working in the transient domain is the limited work so far in this field as well as the physical insight previously mentioned. In addition, acquiring a better understanding of the radiation origin (physics involved) the design of UWB antennas for different applications would be considerably improved.

1.3 Objectives and Outline of this Thesis

The main goal of this work is to provide a relationship between the complex resonances occurring in the antenna and its relevant physical characteristics. In order to achieve this goal a new formalism will be implemented which provides an analytical expression for radiated fields where the time dependence of the wave amplitudes is determined by resonant processes occurring in the structure. Next, some important issues are presented which must be taken into account and achieved during this thesis.

- Implement IRCTR developed algorithm working at every antenna case.
- Carefully and deep study of the algorithm in order to figure out an appropriate and suitable election of the parameters involved.
- Test and validation of the algorithm.
- Analyze time-domain behavior of dipole antenna at different physical configurations.
- Analyze time-domain behavior of circular loop antenna at different physical configurations.
- Analyze time-domain behavior of bow-tie antenna at different physical configurations.

- Determine a relationship between the complex resonant frequencies occurring in the structure and its geometry and dimensions.

1.4 Organization of the thesis

This report is divided into nine chapters:

Chapter 2 provides a brief overview of Ultra-Wide Band characteristics and a new time-domain perspective of the antenna radiation is introduced. Moreover, the adopted model under study in this work is presented.

The aim of Chapter 3 is to present analytically the pole/residue algorithm used along all the thesis work.

In Chapter 4, the software tools used in this work are presented and briefly described.

Chapter 5 takes care of the numerical procedure developed to carry out the algorithm described in Chapter 3. Numerical approaches and selection of parameters are discussed in these lines.

In Chapters 6, 7 and 8 a thorough and deep study of the transient radiation and poles distribution in the complex plane is done for the dipole, bow-tie and loop antenna respectively.

Chapter 2

Background

In this chapter it will be provided the basis for a clear understanding of the rest of the thesis work. First able, UWB definition, its applications and advantages should be pointed out in a brief way. Next, a time domain perspective introduced in [1] of the electromagnetic radiation will be studied thoroughly. Finally, the model under study that will be used from now on will be presented.

2.1 UWB Technology

As defined by the Federal Communications Commission (FCC), UWB technology is meant to transmit and receive information over a large bandwidth [2]. UWB implementations modulate an extremely short duration impulse that has a very sharp rise and fall time, thus resulting in a waveform that occupies several GHz of bandwidth (see Fig.2.1 and Fig.2.2). These are the two conditions of UWB technology:

$$B_W \geq 500MHz \tag{2.1}$$

or

$$\frac{B_W}{f_c} \geq 0.2 \tag{2.2}$$

where f_c is the central frequency and B_W is the bandwidth. UWB can operate between 3.1 and 10.6 GHz at limited transmission powers for indoor

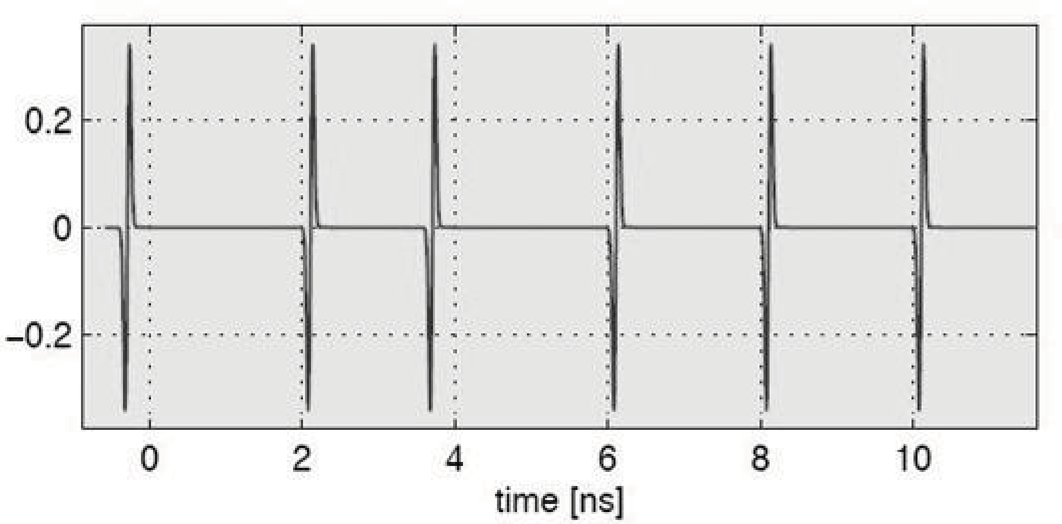

Figure 2.1: UWB Transmission with pulses

communications, as defined in FCC [2]. However, for our purpose, the frequency range of interest will lie between 300 MHz and 6GHz. It must be noticed that the frequency band of interest will depend on the antenna type and this issue should be taken into account in this research.

2.1.1 Advantages

Among others, we can identify the following advantages:

- Possibility of high data rates.
- High resolution localization, due to the very short pulse duration.
- Channel fading resistant, due to the large number of resolvable multipath components.
- Carrier-less signal propagation.
- Overlay with existing frequency allocation, due to the low power spectral density (Fig.2.2).
- Multiple-access capabilities, due to the wide bandwidth of transmission.

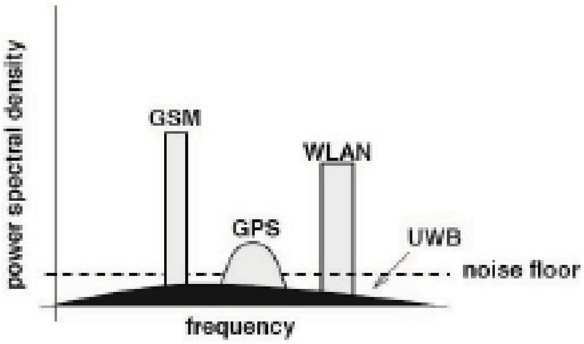

Figure 2.2: Ultra Wide-band and other technologies spectrum

- Propagation through solid materials, due to the presence of energy at different frequencies.

- Possibility of converting communications, with low probability of interception, due to the low power spectral density.

- Simplicity in implementation, low cost of devices.

2.1.2 Applications

A combination of the UWB advantages allows some interesting applications:

- High Resolution Radar. It is one of the first UWB applications, because of the fine positioning characteristics of narrow pulses. They can offer a very high resolution radar.

- Wireless Personal Area Networks (WPAN). UWB is an ideal technology to replace the wires of the personal computers and their peripherals, without interfering with your local wireless network.

- Wireless Body Area Network (WBAN). It consists on a set of autonomous wireless sensors with ultra-low-power requirements spread over the human body or even implanted inside the body.

- Sensor Networks. Networks with sensors placed inside an area or volume. Low- cost and long-life battery-operated devices are very important requirements for this application.

- Location aware communications. The good performance of UWB devices in multi- path channels can provide accurate geolocation capability for indoor and obscured environments where GPS does not work.

- Military communications. The probability to detect or intercept UWB pulses are very low. Thus, the covert military communications are ideal for that purpose.

- Imaging systems, like ocean imaging, medical diagnostic and surveillance devices. UWB reflections of the target exhibit not only changes in amplitude and time shift, but also changes in the pulse shape.

- Vehicular radar systems. Detection of the position and movement of objects near the vehicle are more accurate thanks to UWB devices.

- Emergency Situations. UWB signals can penetrate obstacles because of the wide frequency spectrum. This property is very useful to detect and rescue survivors under rubble in disaster situations.

2.2 Time-Domain Perspective

In this section the main goal is to introduce to the reader a time domain perspective in the study of electromagnetism. A quick and colloquial explanation for the radiation of an antenna that might be heard in a electromagnetism course could be: ”something radiates when there is moving charge involved”. Thinking about it, a simplistic result of this statement yields to the well-known fact that antenna radiates when a time-varying current (moving charge) excite it. Coming back to the charge moving case it is known that the radiation at every point in space is related with the motion of the charge at a particular,earlier time. The directional characteristics of the radiation field depend upon the relative orientation of the velocity and the acceleration. This is illustrated for two cases: bremsstrahlung in Fig.2.3 **a)** where a (acceleration) is parallel to v (velocity) , and synchrotron radiation in Fig.2.3 **b)** where a is perpendicular to v.

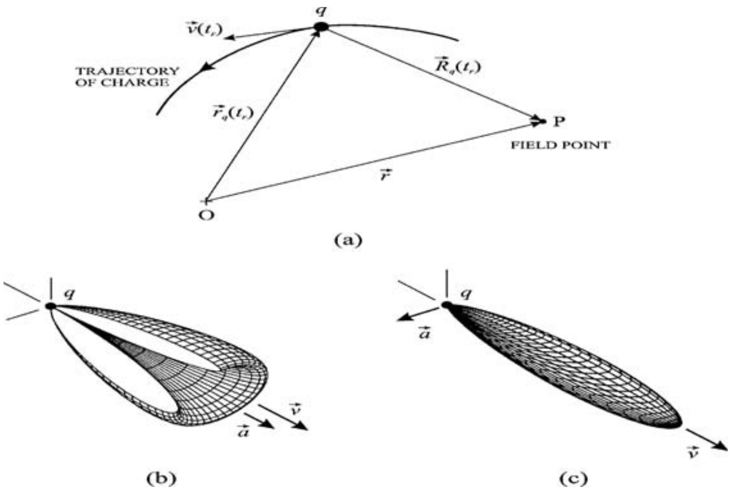

Figure 2.3: (a) Trajectory for the moving point charge and the coordinates used in evaluating the electromagnetic field. Directional characteristics (power radiated per unit solid angle) for the radiation from the point charge when (b) the acceleration is parallel to the velocity, and (c) the acceleration is perpendicular to the velocity. $\beta = \nu/c$

In the case of an antenna such a dipole, something similar can be inferred. If we excite a dipole with a Gaussian pulse, every time this pulse leaves the source or reaches the termination of the wire a wave will arise centering either the source or the termination. Furthermore, if the pulse encounter a bend in the wire a new wave will be propagate due to this phenomena. Therefore, the analogy between the radiation produced by a moving charge and the produced by an antenna is quite clear. In order to reach a better understanding, let us point out a new concept introduced in [1] called: basic traveling-wave element.

2.2.1 The Basic Traveling-Wave Element

The geometry for the basic traveling-wave element and the associated coordinates are shown in Fig.2.4. The element of length h is aligned with the z axis. There is a source of current $I_s(t)$ at the bottom of the element and a perfect termination at the top of the element. This element can be considered as the building block out of which antennas are constructed. Further, this issue will be discussed and electromagnetic fields of an antenna will be evaluated as the superposition of electromagnetic fields of every single element. It is assumed that a traveling wave of current (a pulse) leaves the source and propagates

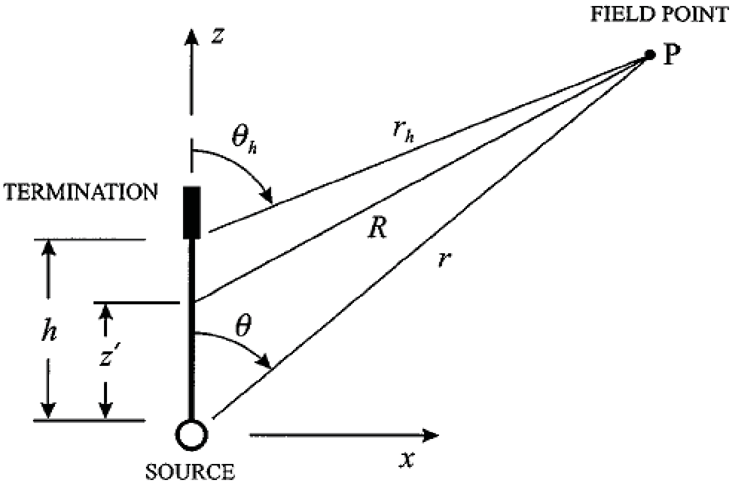

Figure 2.4: Schematic drawing showing the traveling wave element.

along the element at the speed of light, c, until it reaches the termination, where it is totally absorbed. Therefore, the current distribution along the element can be expressed as:

$$I(z,t) = I_s(t - z/c)[U(z) - U(z-h)] \tag{2.3}$$

and the charge per unit length on the element results:

$$Q(z,t) = Q_s(z,t)[U(z) - U(z-h)] + q_0(t)\delta(z) + q_h(t)\delta(z-h) \tag{2.4}$$

$$Q_s(z,t) = I_s(t)/c \, q_0(t) = -\int_{t'=-\infty}^{t} I_s(t')dt', \tag{2.5}$$

$$q_h(t) = -\int_{t'=-\infty}^{t} I_s(t'-h/c)dt', \tag{2.6}$$

and δ is the Dirac delta function. The three terms in Eq.(2.4) represent a traveling wave of positive charge, Q_s, propagating along the element at the speed of light, negative charge, q_0, that is left at the bottom of the element as the positive charge pulse leaves the source and positive charge,q_h, that accumulates at the upper end as the pulse reaches the termination. Notice that the element is always electrically neutral since the same amount of charge positive and negative is accumulated at the upper and bottom ends

respectively.
The complete electromagnetic field of this currents/charge is obtained as follows:

$$\begin{aligned} E(r,t) =& \frac{1}{4\pi\epsilon_0}\left[\frac{q_0(t-r/c)}{r^2}\hat{r} + \frac{q_h(t-r_h/c)}{r_h^2}\hat{r}_h + \frac{\cot(\theta/2)I_s(t-r/c)}{cr}\hat{\theta}\right. \\ & \left. -\frac{\cot(\theta/2)I_s(t-h/c-r_h/c)}{cr_h}\hat{\theta}_h\right] \end{aligned} \tag{2.7}$$

$$H(r,t) = \frac{\mu_0}{4\pi}\left[\frac{\cot(\theta/2)I_s(t-r/c)}{r}\hat{\theta} - \frac{\cot(\theta/2)I_s(t-h/c-r_h/c)}{r_h}\hat{\theta}_h\right]\hat{\varphi} \tag{2.8}$$

In the far distance, $r \rightarrow \infty$, more precisely as $r/c\tau \rightarrow \infty$, being τ the characteristic time associated with the duration of the current, the far-field or radiated field can be written as follows:

$$\begin{aligned} E^r(r,t) =& \frac{\mu_o c \sin\theta}{4\pi r(1-\cos\theta)}\left\{I_s(t-r/c)\right]- \\ & \left[I_s(t-r/c-(h/c)(1-\cos\theta))\right]\right\}\hat{\theta} \end{aligned} \tag{2.9}$$

$$B^r(r,t) = \frac{1}{c}r \times E^r(r,t) \tag{2.10}$$

Following, it will be displayed some results of the electromagnetic fields. In those examples, the excitation signal chosen has been set to a Gaussian pulse as:

$$I_S(t) = I_0 e^{-(\frac{t}{\tau})^2} \tag{2.11}$$

where τ is the characteristic time. The time for light to travel the length of the element is $\tau_a = h/c$. In the examples shown, the relation between the characteristic time and the time for light to travel the element has been chosen to be as $\tau/\tau_a = 0.076$ resulting a pulse width in space is approximately one-fourth of the length of the element (four pulses fit along the element). In Fig.2.5 might be observed the electric field surrounding the traveling-wave element at three different times: $\tau/\tau_a = 0.5, 1.5$ and 2.5. The pulse of current/charge travels up the element until it reaches the termination where it is absorbed.

Basing on previous discussion in Sec.(2.2), a spherical wave front W_1 , centered at $z = 0$, is produced when the pulse leaves the source, and a second spherical wave front W_2 , centered at $z = h$, is produced when the pulse is absorbed by the termination. These wave fronts travel outward from the ends of the element at the speed of light. As can be seen in Fig.2.5 there are strong electric fields near the source and termination independent from the wave fronts. Those static electric fields are produced by negative and positive charges remaining at the source and termination, respectively.

Fig.2.6 **a)** is a drawing detailing the scheme used for plotting the radiated field [1]. A spherical surface of radius r is centered at the source and different observers are stationed at points given by different elevation angles $\theta = 0^o, 22.5^o, 45^o, ...$ Fig.2.6 **b)** shows the radiated field recorded by the aforementioned observers.

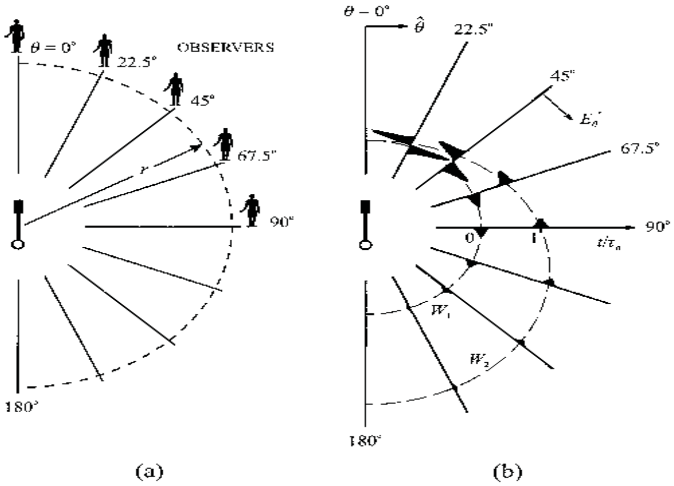

Figure 2.6: (a) Schematic drawing showing the observers that record the time domain wave forms for the radiated field. (b) Radiated or far-zone electric field of the basic traveling-wave element.

As it might be observed different field values are evaluating at each spatial point. Two pulses of electric field are noticed, one belonging to each wave front presented before. The separation between the times of arrival for these pulses changes with the angle of observation θ. Fig.2.7 easily explained this phenomena. The pulses associated with wave fronts W_1 and W_2 will arrive at roughly same time as elevation angle θ approaches to zero, and will be separate exactly $\Delta t = h/c = \tau_a$ when $\theta = 90^o$.

In conclusion, an analogy can be drawn between the radiation from the pulse-excited, basic traveling-wave element and the radiation from a moving

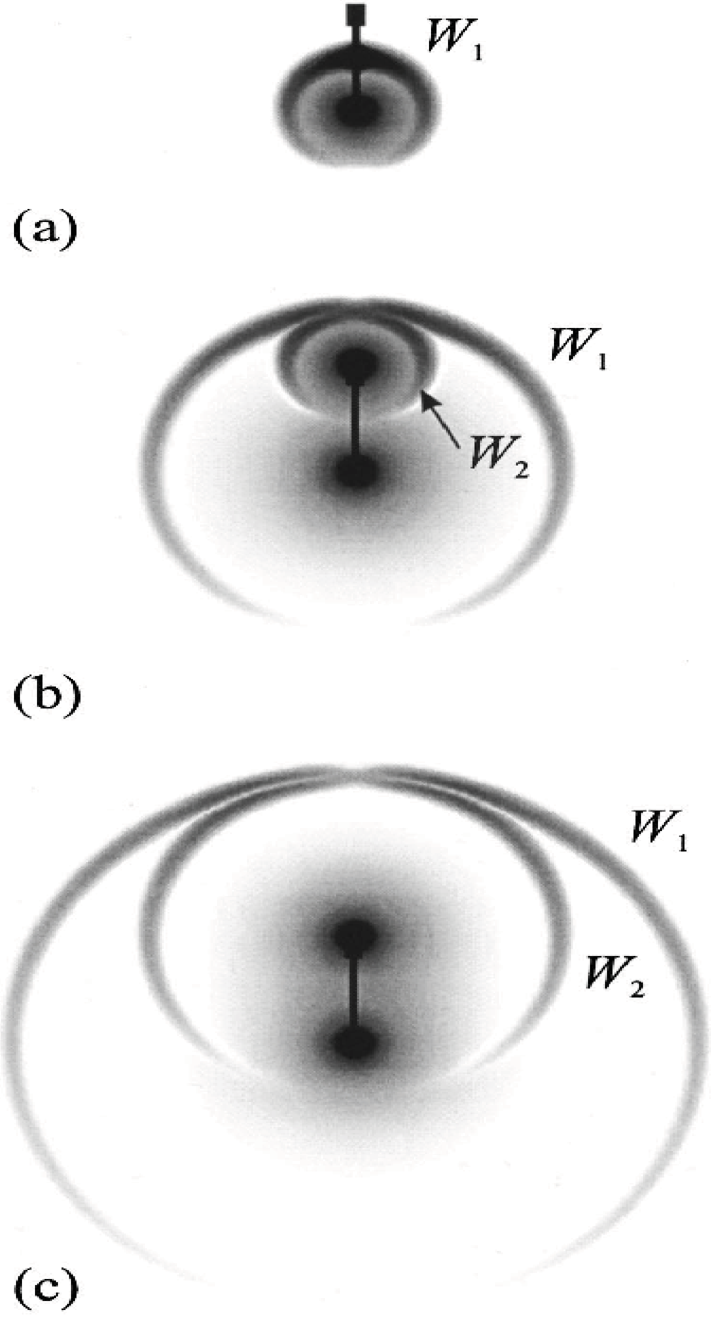

Figure 2.5: The magnitude of the electric field surrounding the basic traveling wave element at three times: (a) $t/\tau_a = 0.5$, (b) $t/\tau_a = 1.5$, and (c) $t/\tau_a = 2.5$.

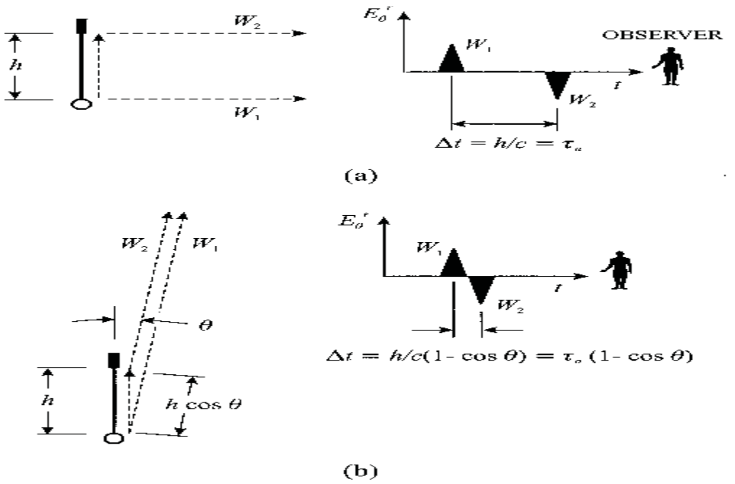

Figure 2.7: Schematic drawings used to describe the difference in the times of arrival for the two pulses in the radiated electric field of the basic traveling-wave element.

point charge. At the time the pulse of charge leaves the source, radiation is produced (spherical wave front with positive electric field) as would do a point charge undergoing acceleration in the direction of velocity. On the other hand, every time the pulse reaches the termination of the element, radiation is again produced (spherical wave front with negative electric field) but as would do it a point charge undergoing deceleration in the direction of velocity. Furthermore, as the pulse is propagating along the element no radiation occurs since there is not any discontinuity in the wire (bends, truncation,...).

Finally, looking back to Fig.2.3 b) and comparing with Fig.2.6 b) it can be observed that similar results are obtained since radiation Fig.2.6 b) is also zero in the direction of the motion of the pulse charge ($\theta = 0^o$) and maximum at a small angle to this direction.

To summarize, it has been presented results obtained for a pulse-excited wave-travel element electromagnetic fields both analytically (equations) and qualitatively (figures). Furthermore, it has been introduced a new concept, traveling-wave element which might be considered a building block for a real antenna. Therefore, the electromagnetic fields could be evaluated as superposition of the contributions of every single element forming the antenna under study.

2.2.2 The Standing-Wave Dipole Antenna

In this section, a brief example based on previous reading will be discussed. The standing wave-dipole as defined in [1] might be looked as a superposition of four basic traveling-wave elements. So, the electromagnetic field can be evaluated as:

$$\mathbf{E}(\mathbf{r},t)=\sum_{i=1}^{4}\mathbf{E}_i(\mathbf{r},t),\ \ \mathbf{B}(\mathbf{r},t)=\sum_{i=1}^{4}\mathbf{B}_i(\mathbf{r},t), \tag{2.12}$$

In this case, a wave front W_1 arises when the pulse leaves the source, W_2 and $W_{2'}$ arise when the pulse is absorbed at the upper and bottom ends respectively and a third one, W_3 when the pulses are absorbed at the source. It must be pointed out that now the electric field about the source and open ends is negligible since there is no accumulation of charge. This is due to the amount of positive and negative charge leaving and entering the source and open ends are equal (see Fig.2.8). The excitation selected in this case is a Gaussian pulse with $t/\tau_a = 0.076$ where $\tau_a = h/c$ being h the length of the arm and c the speed of light.

In Fig.2.9, it is shown the radiated field evaluated at different spatial points depending on elevation angle θ. In this case, it can be observed how at $\theta = 90^o$ wave fronts W_2 and $W_{2'}$ interfere constructively. Thus, as might be expected from frequency-domain antenna study, the maximum of radiation of the dipole is located at $\theta = 90^o$.

2.2.3 Circular Loop Antenna

In this section it will be shown a example of a loop antenna formed by several basic traveling-wave elements. Then, an example of radiation due to the bend of the wire will be considered. In this case, besides the already known wave fronts arising whenever a pulse of charge leaves the source or reaches a termination (W_1 and W_3), a third one W_2 is continuously produced as the pulse propagates around the loop. The cause of the latter wave front is the curvature of the loop (see Fig.2.10). The excitation selected in this case is a Gaussian pulse with $t/\tau_a = 0.076$ where $\tau_a = 2b/c$ being b the radius of the loop and c the speed of light. It is well-known that for a moving point charge radiation occurs whenever there is acceleration and in this case, acceleration is changing in direction but not in magnitude. Therefore, the

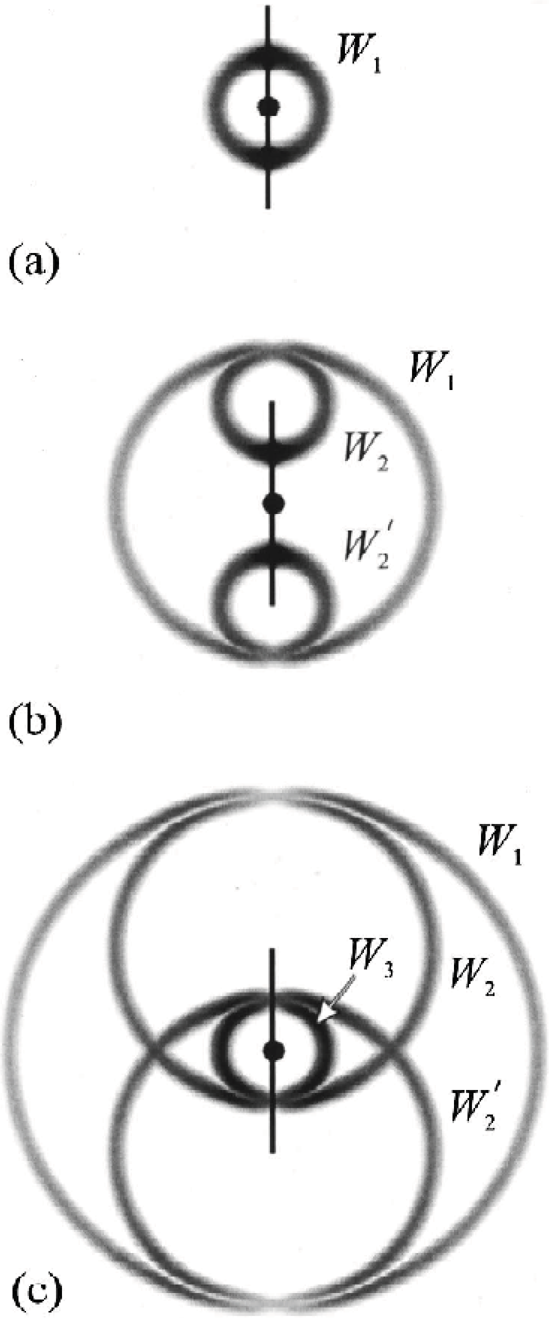

Figure 2.8: The magnitude of the electric field surrounding the standing-wave dipole at three times: (a) $t/\tau_a = 0.5$, (b) $t/\tau_a = 1.5$, and (c) $t/\tau_a = 2.5$.

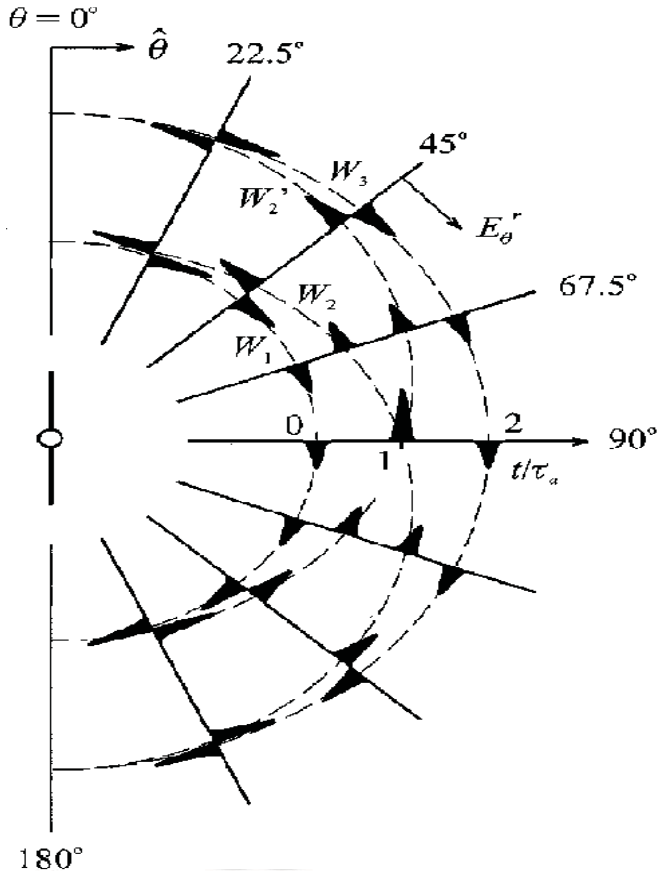

Figure 2.9: Radiated or far-zone electric field of the standing-wave dipole.

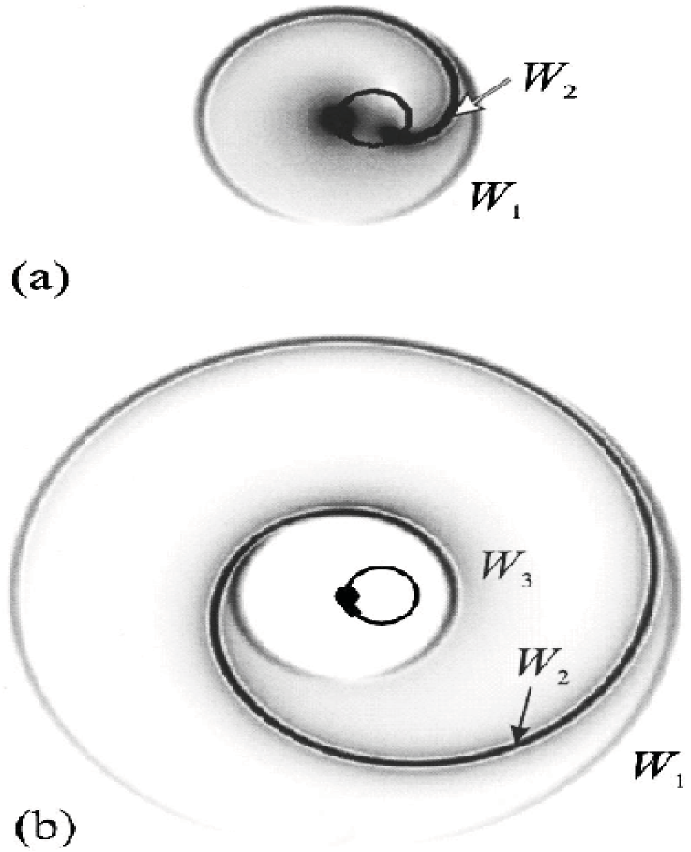

Figure 2.10: The magnitude of the electric field surrounding the traveling-wave, circular loop antenna at two times: (a) $t/\tau_a = 5\pi/8 = 1.96$, (b) $t/\tau_a = 3\pi/2 = 4.71$.

radiation will be similar as the case of a point charge moving of a curve trajectory at constant speed.

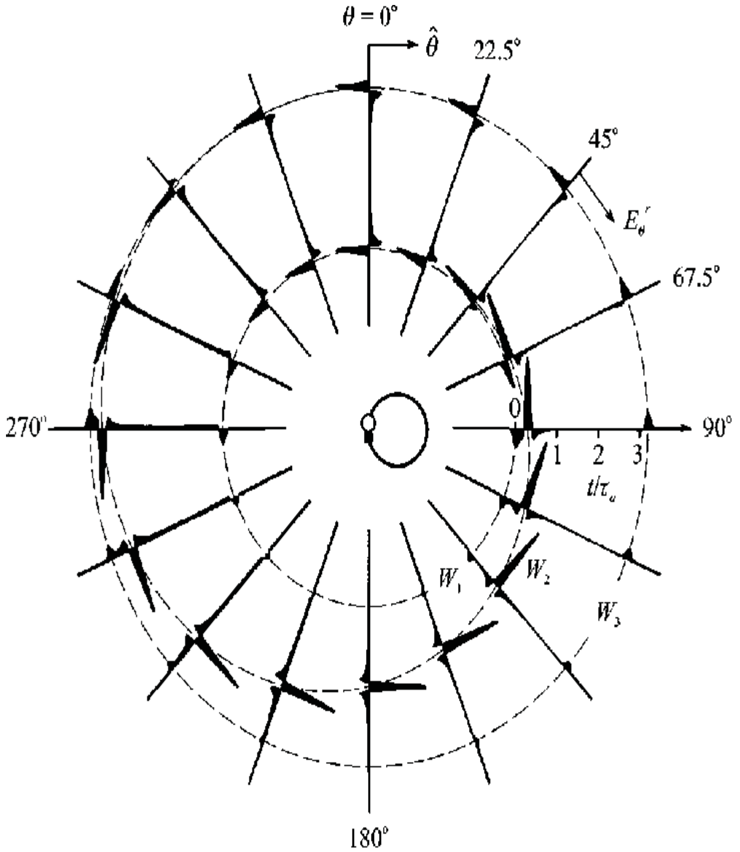

Figure 2.11: Radiated or far-zone electric field of the traveling-wave, circular loop antenna.

2.3 Model under study

Once introduced some basics in previous section, let us now focus on our model under study. In few words, there are three clearly differentiated elements: excitation signal, antenna and algorithm. In order to picture up our mind the following analogy will be drawn. As it might be known, a tuning fork is an acoustic resonator which main use is as a standard of pitch to tune musical instruments. Usually, this instrument is hit and supposed to perform

Figure 2.12: Analogy drawing of the model under study.

a pure tone at a certain frequency depending on the length of its two prongs. However, sometimes the energy of the sound is not high enough for the human ear, therefore a resonant box is used in order to amplify the signal. In our case of study, the Gaussian pulse will play the role of the quick hit to the tune fork, our antenna under study will play the role of the tuning fork and the algorithm will be the amplifier/human ear combination which allow us "hearing" the frequencies resonating in that antenna. (see Fig. 2.12)

2.3.1 Excitation signal: Gaussian Pulse

Since the field of study in this work is UWB technology, Gaussian pulses come up as excitation signals. In UWB applications short pulses are transmitted by the antenna. The shorter the pulse is in time-domain the wider will be in frequency domain. Therefore, the larger amount of resonant frequencies will be excited. In our case, we have chosen the usual Gaussian pulse (non-derivative) covering the frequency range of interest. The Gaussian waveforms are a class of waveforms with a definition similar to the Gauss function:

$$G(x) = \frac{1}{\sqrt{2\pi\sigma^2}} e^{-x^2/2\sigma^2} \tag{2.13}$$

where σ is the standard deviation. The generator of the Gaussian waveforms is a Gaussian pulse

$$g_1 = K_1 e^{(t-\tau)^2/2T^2} \tag{2.14}$$

where $-\infty < t < \infty$, T is a time scaling factor affecting the signal duration, τ determines the signal temporal position and K_1 is a constant which determines the energy of the signal. Further waveforms can be created by differentiation of the Gaussian pulse. However, the original Gaussian waveform will be used as excitation signal in this research. The Gaussian waveforms are useful for:

- Modeling the excitation of UWB systems: the Gaussian pulse and its derivatives can be simply realized using a pulse generator and some differentiator circuit.

- Numerical analysis of radiating elements: a Gaussian waveform is the typical signal excitation of commonly used electromagnetic simulation tools, such as the FDTD, because of its large bandwidth that permits a broadband analysis of the antenna response.

In this study, the excitation signal will be set as the usual Gaussian pulse. Since a wide study in quest of complex frequencies excited in different antennas is required, it will be needed a pulse which excites all the frequencies in a certain range. In order to extract a good understanding it will fixed the same pulse for the different antennas of a certain type. Therefore by changing different geometrical parameters of the antenna it will be seen the impact of the pulse propagating along the structure.

2.3.2 Structure under analysis: Antenna

Since this study in time-domain has not been performed thoroughly, a good beginning could be to analyze basic antennas. Although dipole is a radiator that likely is not considered an UWB antenna, its simple geometry and well-known radiation patterns and time domain behavior give us a starting point in this study. However, it is known that even though dipole is a resonant antenna by increasing the thickness of the conductor wire the resonant frequency range can be enlarged approaching it to an UWB behavior.

In addition, as discussed in previous section would be interesting analyze the behavior of a loop antenna since its curvature produces a different type of radiation as the dipole antenna. Besides, again two parameters can be considered as the radius of the loop and the diameter of the wire.

Furthermore, another interesting antenna to take into account is the bowtie antenna. As we know this structure is family of the previous antenna mentioned. Bow-tie antenna is a sort of dipole consisting on two planar conductor flairs. There are two parameters to take into account: the length of the antenna and the angle of the flare. Analyzing the response of the antenna variating this two parameters we will be able to make up a relationship between complex frequencies occurring in the structure and physical and geometrical characteristics.

Since this work focuses mainly in UWB technology, our frequency range taken into account will spread from 0.3 GHz to 6 GHz depending on the type of the antenna.

(a) Dipole Antenna (b) Loop Antenna (c) Bow-Tie Antenna

Figure 2.13: Examples of real antennas that would be considered in the research.

2.3.3 Algorithm: New formalism

In this section a new formalism based on singularity-expansion-method should be introduced. This approach is proposed for the accurate time- and frequency-domain analysis and modeling of electromagnetic field radiation from ultra-wideband antennas. By means of this approach transient electromagnetic field radiation in Fraunhofer region is presented in analytical closed form as the superposition of outgoing propagating non-uniform spherical waves. Time dependence of the wave amplitudes will be determined by the radial distance and the resonant processes occurring in the structure.

To this end, any time-domain integral-equation or finite-difference technique can be adopted to evaluate the full wave analysis within a spherical volume surrounding the antenna (Huygens Sphere), and determine a spherical harmonic expansion of the equivalent and magnetic currents excited on a suitable Huygens surface enclosing the structure under study. Next, a pole/residue representation of the electric and magnetic currents is derived in a specially developed time-domain vector fitting procedure. Then, a new class of special functions, namely incomplete modified spherical Bessel functions, is introduced in order to get simple analytical expressions for the radiated field. Formulation and implementation of this algorithm will be exhaustively studied in following chapters along this thesis work.

Chapter 3

Algorithm: Pole/Residue Modeling

The aim of this chapter is to introduce to the reader a new formalism for expressing radiated electromagnetic fields in terms of dumped exponential functions. This procedure is a two-step data fitting algorithm which firstly a spherical harmonic expansion method is performed and next a SEM (Singular Expansion Method) is used providing a SEM-based expression of complex poles and vector residues. In that way, exponential terms accounting for the damped natural resonant processes are outlined and used in the radiated field evaluation.

3.1 Pole/Residue Modeling

In this section, a deep study of the algorithm mentioned in previous chapter should be done. To this end, let us consider an antenna operating in free space enclosed by a spherical surface S_h having radius R_h. Denoting by $\mathbf{E}(\mathbf{r},t), \mathbf{H}(\mathbf{r},t)$ the electric and magnetic field respectively, excited by the considered radiating structure at any observation point $\mathbf{r} \equiv \{r, \vartheta, \varphi\}$ and at any time $t \geq 0$, the Huygens density currents can be easily evaluated as:

$$\mathbf{J}_s(r,\vartheta,\varphi) = \hat{\mathbf{r}} \times \mathbf{H}(R_h,\vartheta,\varphi,t), \tag{3.1}$$

$$\mathbf{M}_s(r,\vartheta,\varphi) = \mathbf{E}(R_h,\vartheta,\varphi,t) \times \hat{\mathbf{r}}. \tag{3.2}$$

As known from theory [5], the spatial distribution of the electromagnetic radiated field for $r \gg R_h$ can be readily determined by convolving the equivalent currents densities $\mathbf{J}_s(r,\vartheta,\varphi), \mathbf{M}_s(r,\vartheta,\varphi)$ excited along the Huygens sphere with the radiative components of the dyadic Green's functions:

$$\underline{\mathbf{g}}_{\mathbf{J}}^{\mathbf{E}}(\mathbf{r}|\mathbf{r}',t) = \eta_0^2 \underline{\mathbf{g}}_{\mathbf{M}}^{\mathbf{H}}(\mathbf{r}|\mathbf{r}',t) = -\eta_0(\underline{\mathbf{1}} - \hat{\mathbf{R}}\hat{\mathbf{R}})\partial_t g_0(R,t)/c_0 \tag{3.3}$$

$$\underline{\mathbf{g}}_{\mathbf{M}}^{\mathbf{E}}(\mathbf{r}|\mathbf{r}',t) = -\underline{\mathbf{g}}_{\mathbf{J}}^{\mathbf{H}}(\mathbf{r}|\mathbf{r}',t) = \hat{\mathbf{R}} \times \underline{\mathbf{1}}\partial_t g_0(R,t)/c_0 \tag{3.4}$$

with $g_0(R,t) = \delta(t - R/c_0)/(4\pi R)$, where $\underline{\mathbf{1}} = \hat{\mathbf{r}}\hat{\mathbf{r}} + \hat{\boldsymbol{\vartheta}}\hat{\boldsymbol{\vartheta}} + \hat{\boldsymbol{\varphi}}\hat{\boldsymbol{\varphi}}$, $\mathbf{R} = \mathbf{r} - \mathbf{r}'$,$R = |\mathbf{R}|$ and $\hat{\mathbf{R}} = \mathbf{R}/R$. As usual, the quantities $\{\mathbf{r} \equiv r,\vartheta,\varphi\}$ and $\{\mathbf{r}' \equiv r',\vartheta',\varphi'\}$ denote the observation and source points respectively, c_0 is the speed of light, and η_0 is the free-space wave impedance. Being mainly interested in the radiated-field antenna behavior, it might be used the following approximation:

$$R \simeq r - \hat{\mathbf{r}} \cdot \mathbf{r}' = r - R_h \cos\gamma \tag{3.5}$$

with:

$$\cos\gamma = \sin\vartheta \sin\vartheta' \cos(\varphi - \varphi') + \cos\vartheta \cos\vartheta', \tag{3.6}$$

in order to evaluate the previously mentioned convolution integrals. As discussed in [6], that approximation can be only performed once the time-domain Fraunhofer condition is achieved:

$$r \gg \frac{4R_h^2}{c_0 T_g}, \tag{3.7}$$

T_g being the pulse-length of the antenna excitation signal.
Therefore, under the considered condition, the transient (time-domain) radiative electromagnetic field excited by the antenna outside the surface S_h delimited by Huygens radius R_h is meant to be, after some algebra, as the following vector slant-stack transform (SST) of the surface equivalent current densities:

$$\begin{aligned}\mathbf{E}(\mathbf{r},t) \simeq & \frac{1}{4\pi r c_0} \int\int_{S_h} \hat{\mathbf{r}} \times [\eta_0 \hat{\mathbf{r}} \times \dot{\mathbf{J}}_{\mathbf{s}}(\vartheta',\varphi',\tau + t_h\cos\gamma) + \\ & + \dot{\mathbf{M}}_{\mathbf{s}}(\vartheta',\varphi',\tau + t_h\cos\gamma)]dS',\end{aligned} \tag{3.8}$$

$$\mathbf{H}(\mathbf{r},t) \simeq \frac{1}{\eta_0}\hat{\mathbf{r}} \times \mathbf{E}(\mathbf{r},t), \tag{3.9}$$

where $t_h = R_h/c_0$, and $\tau = t - r/c_0$ is the spherical-wave delayed time. The radiation integral appearing in Eq.(3.8) provides a fast and accurate evaluation of the far-field in transient domain. However, do not provide a physical information about the resonant processes occurring in the structure. Therefore, this equation can be conveniently rewritten by applying a two-step data-fitting procedure aimed to the expansion of the equivalent currents in terms of time-variant vector spherical harmonics functions with proper coefficients. At any time $t \geq 0$, the afore-mentioned density currents can be expressed as the linear combination of orthonormalized surface harmonics [7], defined as:

$$Y_n^m(\vartheta,\varphi) = \sqrt{\frac{2n+1}{4\pi}\frac{(n-m)!}{(n+m)!}}P_n^m(\cos\vartheta)e^{-jm\varphi}, \tag{3.10}$$

$P_n^m(z)$ being the associated Legendre function of the first kind of degree n and order m [17]. Furthermore, the following identity holds [7]:

$$Y_n^{-m}(\vartheta,\varphi) = (-1)^m Y_n^{m^*}(\vartheta,\varphi), \tag{3.11}$$

where the superscript * denotes complex conjugation.

$$\left\{\begin{array}{c}\mathbf{J}_s(\vartheta,\varphi,t)\\ \mathbf{M}_s(\vartheta,\varphi,t)\end{array}\right\} = \sum_{n=0}^{N}\sum_{m=-n}^{n}\left\{\begin{array}{c}\boldsymbol{\alpha}_{n,m}(t)\\ \boldsymbol{\beta}_{n,m}(t)\end{array}\right\}Y_n^m(\vartheta,\varphi), \tag{3.12}$$

where the vector coefficients $\alpha_{n,m}(t)$ and $\beta_{n,m}(t)$ are computed as:

$$\begin{aligned}\left\{\begin{array}{c}\boldsymbol{\alpha}_{n,m}(t)\\ \boldsymbol{\beta}_{n,m}(t)\end{array}\right\} &= \left\langle\left\{\begin{array}{c}\mathbf{J}_s(\vartheta,\varphi,t)\\ \mathbf{M}_s(\vartheta,\varphi,t)\end{array}\right\}, Y_n^m(\vartheta,\varphi)\right\rangle\\ &= \int_0^{2\pi}\int_0^{\pi}\left\{\begin{array}{c}\mathbf{J}_s(\vartheta,\varphi,t)\\ \mathbf{M}_s(\vartheta,\varphi,t)\end{array}\right\}Y_n^{m^*}(\vartheta,\varphi)\sin\vartheta d\vartheta d\varphi.\end{aligned} \tag{3.13}$$

The series expansion in Eq.(3.12) will be exact as long as n goes to infinity. Therefore unavoidable truncation errors will arise when limiting the sum over n to a finite discrete angular bandwidth N. However, this problem can be mitigated, according to the theory of the optimal interpolation of radiated electromagnetic fields over a sphere [13]-[14], by selecting parameter N to be as:

$$N = \left\lceil\frac{2\pi\chi R_h}{c_0 T_g}\right\rceil, \tag{3.14}$$

$\lceil\cdot\rceil$ being the usual ceiling function [17]. In Eq.(3.14) the excess bandwidth factor χ is selected to control the approximation error which decreases more

than exponentially with $\chi - 1$ [13]. In the following section, a dedicated procedure to compute expansion integrals in Eq.(3.12) has been developed and analytical details will be thoroughly investigated.
Since the considered antenna is excited by a finite-duration signal (Gaussian pulse), the current expansion in Eq.(3.12) can be expressed using the SEM-based formula:

$$\left\{ \begin{array}{c} \boldsymbol{\alpha}_{n,m}(t) \\ \boldsymbol{\beta}_{n,m}(t) \end{array} \right\} = \sum_{k=1}^{K} \left\{ \begin{array}{c} \mathbf{a}_{n,m,k} \\ \mathbf{b}_{n,m,k} \end{array} \right\} e^{s_{n,m,k} t} u(t) + \left\{ \begin{array}{c} \mathbf{A}_{n,m,k} \\ \mathbf{B}_{n,m,k} \end{array} \right\} \tag{3.15}$$

where $s_{n,m,k} = -\sigma_{n,m,k} + j\omega_{n,m,k}$ and $\mathbf{a}_{n,m,k}$, $\mathbf{b}_{n,m,k}$ are the complex poles and vector residues of the exponential terms accounting for the damped natural resonant processes occurring in the structure. In Eq.(3.15) $u(t)$ is the usual Heaviside unit-step distribution.

From the SEM theory it is known that the entire functions $\mathbf{A}_{n,m}(t), \mathbf{B}_{n,m}(t)$ are needed to accurately describe the early-time behavior of the antenna. However, as discussed in [11]-[12], such terms are usually neglected, and their contribution efficiently taking into account by means of a modified pole/residue representation. Therefore, substituting equations Eq.(3.12) and Eq.(3.15) into equations Eq.(3.8) and Eq.(3.9) yields:

$$\begin{array}{l} \left\{ \begin{array}{c} \mathbf{E}(r,\vartheta,\varphi,t) \\ \mathbf{H}(r,\vartheta,\varphi,t) \end{array} \right\} \simeq \dfrac{R_h^2}{4\pi r c_0} \displaystyle\sum_{n=0}^{N} \sum_{m=-n}^{n} \sum_{k=1}^{K} s_{n,m,k} e^{s_{n,m,k}\tau} \left\{ \begin{array}{c} \mathbf{e}_{n,m,k} \\ \mathbf{h}_{n,m,k} \end{array} \right\} \cdot \\ \qquad\qquad \cdot \displaystyle\int\!\!\int_{\Omega_h} e^{s_{n,m,k} t_h \cos\gamma} Y_n^m(\vartheta',\varphi') \sin\vartheta' d\vartheta' d\varphi', \end{array} \tag{3.16}$$

where:

$$\left\{ \begin{array}{c} \mathbf{e}_{n,m,k} \\ \mathbf{h}_{n,m,k} \end{array} \right\} = \hat{\mathbf{r}} \times \left\{ \begin{array}{c} \eta_0 \hat{\mathbf{r}} \times \mathbf{a}_{n,m,k} + \mathbf{b}_{n,m,k} \\ -\mathbf{a}_{n,m,k} + \hat{\mathbf{r}} \times \mathbf{b}_{n,m,k}/\eta_0 \end{array} \right\} \tag{3.17}$$

Reached this point, a new class of functions is introduced in order to evaluate the radiation integrals in equation Eq.(3.16). This function namely incomplete modified spherical Bessel can be defined as:

$$i_n(\xi,\omega) = \frac{1}{2} \int_{-\omega}^{1} e^{\xi z} P_n(z) dz \tag{3.18}$$

and setting for shortness:

$$\hat{i}_n\left(\xi,\omega\right) = i_n\left(\xi, min\left\{1,\omega\right\}\right) \quad (\omega \in \mathrm{R}) \tag{3.19}$$

Consequently, the time-domain electromagnetic field radiated can be obtained as the following superposition of outgoing propagating non-uniform spherical waves attenuating along with the radial distance and time according to the real part of the complex poles:

$$\begin{aligned}\left\{\begin{array}{c}\mathbf{E}(r,\vartheta,\varphi,t)\\ \mathbf{H}(r,\vartheta,\varphi,t)\end{array}\right\} \simeq \frac{t_h R_h}{r}\sum_{n=0}^{N}\sum_{m=-n}^{n}\sum_{k=1}^{K} s_{n,m,k} e^{s_{n,m,k}\tau} u\left(\frac{c_0\tau}{R_h}\right)\cdot \\ \cdot\hat{i}_n\left(s_{n,m,k}t_h,\frac{\tau}{t_h}\right) Y_n^m\left(\vartheta,\varphi\right)\left\{\begin{array}{c}\mathbf{e}_{n,m,k}\\ \mathbf{h}_{n,m,k}\end{array}\right\}\end{aligned} \tag{3.20}$$

Adopting Eq.(3.20) can be conveniently determined the antenna characteristics such gain and directivity and far-field response to any arbitrary excitation.

3.1.1 Spherical Harmonics

As discussed in Sec.(3.1), spherical harmonics functions are used as a mathematical tool to project a spherical function (density currents) at any time, as linear combination of surface harmonics. Spherical harmonics are actually a angular portion of a set of solutions of Laplace's equation represented in spherical coordinates forming an orthogonal system. Besides, interesting properties of those functions might be exploited. For instance, symmetry property Eq.(3.11) might be used for saving computation time in the expansion coefficients evaluation. Spherical harmonics has been used in many different applications such as computer graphics.

In Fig.3.1, can be observed spherical harmonics corresponding to $n = 1$ and $m = -1, 0, 1$. As expected, when m=0 the azimuth distribution of the spherical harmonics do not change. In addition, Eq.(3.11) holds and can be checked looking at Fig.3.1 where the real and imaginary part of harmonics with $n = 1, m = -1$ and $n = 1, m = 1$ are opposite and equal respectively.

3.1.2 Incomplete Modified Spherical Bessel Function

Incomplete modified spherical Bessel functions are firstly introduced in [4]. Therefore, special attention must be paid to them. Besides providing a analytical way of evaluating radiation integrals in Eq.(3.16), those functions provide a physical insight into the wave phenomena concerning truncated

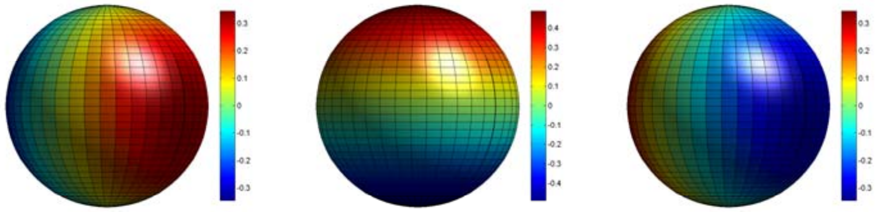

(a) Real part: n=1, m=-1 (b) Real part: n=1, m=0 (c) Real part: n=1, m=1

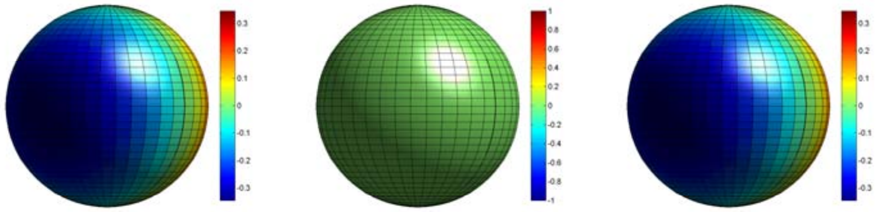

(d) Imag. part: n=1, m=-1 (e) Imag. part: n=1, m=0 (f) Imag. part: n=1, m=1

Figure 3.1: Spherical Harmonics with band coefficient *n=1*

spherical structures. Recalling Eq.(3.16), $\Omega_h = \Omega_h(\vartheta', \varphi', \vartheta, \varphi.\tau/t_h)$ denotes the angular domain of the equivalent currents along the Huygens Sphere contributing, at the normalized time τ to the radiated electromagnetic field at the observation point $\{r > R_h, \vartheta, \varphi\}$. Hence, Ω_h can be expressed as:

$$\Omega_h = \{(\vartheta', \varphi') \in [0, \pi] \times [0.2\pi) : \cos\gamma > -\tau/t_h\} \tag{3.21}$$

In order to evaluate the radiation integrals in Eq.(3.16), Laplace integral representation of the Heaviside distribution is used:

$$u(t) = \mathcal{L}^{-1}\left\{\frac{1}{p}\right\} = \frac{1}{2\pi j}\int_{\sigma-\infty}^{\sigma+\infty} \frac{e^{pt}}{p} dp \ \ (\sigma \in \mathbb{R}^+) \tag{3.22}$$

Then, by exploiting the following projection property of the surface harmonics [19]:

$$\int_0^{2\pi}\int_0^{\pi} e^{\xi\cos\gamma} Y_n^m(\vartheta', \varphi') \sin\vartheta' d\vartheta' d\varphi' = 4\pi i_n(\xi) Y_n^m(\vartheta, \varphi) \tag{3.23}$$

$i_n(\xi) = \sqrt{\frac{1}{2}\pi/\xi}\, I_{n+1/2}(\xi)$ being the canonical modified spherical Bessel function of the first kind and order n. So then, radiation integrals in Eq.(3.16), can be evaluated as:

$$\begin{aligned}\iint_{\Omega_h} e^{s_{n,m,k}t_h\cos\gamma} Y_n^m(\vartheta',\varphi')d\Omega' = \int_0^{2\pi}\int_0^{\pi} u(\tau + t_h\cos\gamma)e^{s_{n,m,k}t_h\cos\gamma} \\ Y_n^m(\vartheta',\varphi')d\Omega' = 4\pi\mathcal{L}^{-1}\left\{\frac{1}{p}i_n[t_h(p+s_{n,m,k})]\right\}(\tau)Y_n^m(\vartheta,\varphi)\end{aligned} \tag{3.24}$$

where $d\Omega' = \sin\vartheta' d\vartheta' d\varphi'$ is the infinitesimal solid angle, and:

$$\begin{aligned}\mathcal{L}^{-1}\left\{\frac{i_n(p+\xi)}{p}\right\}(\Phi) =& \frac{1}{4\pi}\int_0^{2\pi}\int_0^{\pi} u(\Phi + \cos\vartheta)e^{\xi\cos\vartheta}\frac{Y_n(\vartheta,\varphi)}{Y_n(0,0)} \\ &\sin\vartheta d\vartheta d\varphi = i_n(\xi, \min\{1,\Phi\})\mathrm{u}(\Phi)\end{aligned} \tag{3.25}$$

Then the final solution of the radiation integrals look like:

$$\begin{aligned}\iint_{\Omega_h} e^{s_{n,m,k}t_h\cos\gamma} Y_n^m(\vartheta',\varphi')\sin\vartheta' d\vartheta' d\varphi' =& 4\pi\hat{i}_n(s_{n,m,k}t_h, \tau/t_h) \\ & u(\tau/t_h)Y_n^m(\vartheta,\varphi)\end{aligned} \tag{3.26}$$

It must be noticed, that those incomplete modified spherical functions account for the very early transient when only a portion of the surface S_h corresponding to the intersection of the solid angle Ω_h and the half space $\tau + \hat{\mathbf{r}}\cdot\mathbf{r}/c - 0 > 0$ gives contributions to the electromagnetic field excited in the observation point $\mathbf{r} = \{r > R_h, \vartheta, \varphi\}$. As τ approaches to t_h each term $i_n(s_{n,m,k}t_h, \min\{1, \tau/\mathrm{t_h}\})$ will approach to a time-independent canonical spherical Bessel function-related quantity, meaning that the observation point starts to collect wave contributions from the whole Huygens sphere. In order to check the goodness of the afore-mentioned functions, let us perform a numerical example. Two routines has been developed performing right-hand side and left-hand side of Eq.(3.26). Despite inputs such as n, m, ϑ, φ or $\xi = s_{n,m,k}t_h$ has not been chosen following any criteria, τ/t_h has been spread from 0 to 1.2 in order to observe similarity at different values. In addition, previous behavior described when $\tau \to t_h$ can be observed (see Fig.3.2). Beyond that value, incomplete Bessel function approaches to a time-independent canonical spherical Bessel function.

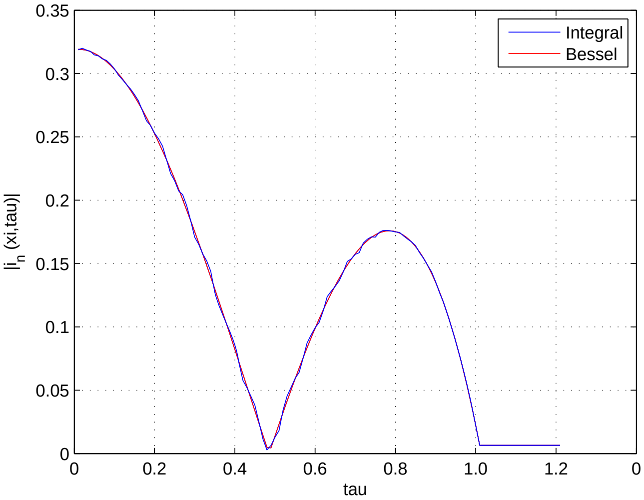

Figure 3.2: Comparison between radiation integrals and incomplete Bessel functions results. Parameters: $n = 3, m = 1, \xi = 0.5, \vartheta = \pi/7$ and $\varphi = \pi/4$

3.2 Analytical Evaluation of Spherical Expansion coefficients

In this research, the electromagnetic field distribution over the Huygens surface S_h enclosing the structure under analysis has been evaluated by means of a full-wave time-domain procedure, specifically FIT which is used by the commercial software CST Microwave Studio. Therefore, it can be assumed that the electromagnetic field $\mathbf{F}(\mathbf{r}, t) = [\mathbf{E}(\mathbf{r}, t)\, \mathbf{H}(\mathbf{r}, t)]$ is known at any discrete node $\bar{\mathbf{r}}|_{i,j,k} \in \mathcal{M}$ being $\mathcal{M} \subset \mathbb{R}^3$ a suitable three-dimensional space lattice.

Under such hypothesis and setting for shortness $\mathbf{F}\ |_{i,j,k}^{t} = \mathbf{F}(\bar{\mathbf{r}}\ |_{i,j,k}, t)$, the field distribution excited along the Huygens sphere can be conveniently evaluated by using a interpolation technique such as local inverse weighting distance (IDW) as:

$$\mathbf{F}(\mathbf{r}, t) \simeq \frac{\sum_{i,j,k} w(\bar{\mathbf{r}}\ |_{i,j,k} - \mathbf{r})\mathbf{F}\ |_{i,j,k}^{t}}{\sum_{i,j,k} w(\bar{\mathbf{r}}\ |_{i,j,k} - \mathbf{r})}, \tag{3.27}$$

the summation being carried out over the triplets $(i, j, k) \in \mathbb{Z}^3$ relevant to the field samples located in the neighborhood of the observation point $\mathbf{r} \in S_h$

and where $w(\mathbf{R}) = |\mathbf{R}|^{-2}$ denotes the adopted weighting function. In the code developed, the neighborhood region is determined by the number of neighbors n, in other words, the summation will be carried out by the field value of the n nearest neighbors. Once electromagnetic field is evaluated over the observations points, Huygens currents can be readily obtained as:

$$\mathbf{J}_s(\vartheta,\varphi,t) = \mathbf{H}(R_h,\vartheta,\varphi,t)\times\hat{\mathbf{r}} \tag{3.28}$$

$$\mathbf{M}_s(\vartheta,\varphi,t) = \hat{\mathbf{r}}\times\mathbf{E}(R_h,\vartheta,\varphi,t) \tag{3.29}$$

According to the theory of the optimal interpolation of radiated fields over a sphere [14], the following cardinal series (CS) representation holds:

$$\begin{aligned}\mathbf{I}_S(\vartheta,\varphi,t) \simeq & \mathbf{I}_S(0,\varphi,t)\Pi_N(\vartheta) + \sum_{n=1}^{N}\Bigg\{\Pi_N(\vartheta-\vartheta_n)\cdot\sum_{m=-M_n}^{M_n}\mathbf{I}_S(\vartheta_n,\varphi_{n,m},t)\cdot \\ & \Pi_{M_n}(\varphi-\varphi_{n,m}) + \Pi_N(\vartheta+\vartheta_n)\sum_{m=-M_n}^{M_n}\mathbf{I}_S(\vartheta_n,\varphi_{n,m},t)\cdot \\ & \Pi_{M_n}(\varphi+\pi-\varphi_{n,m})\}\end{aligned} \tag{3.30}$$

with:

$$\Pi_k(z) = \frac{\operatorname{sinc}\left(\frac{2k+1}{2}z\right)}{\operatorname{sinc}(z/2)} = \frac{1}{1+2k}\sum_{i=-k}^{k}e^{jiz} \tag{3.31}$$

and where a trivial reasoning about the vector transformation in spherical coordinates leads to the conclusion that:

$$\mathbf{I}_S(0,\varphi,t) = \lim_{\vartheta\to 0^+}\mathbf{I}_S(\vartheta,\varphi,t) = \hat{\mathbf{I}}_S^+(t)e^{j\varphi} + \hat{\mathbf{I}}_S^-(t)e^{-j\varphi} \tag{3.32}$$

In Eq.(3.30) the expansion orders N and M_n are given, respectively, by Eq.(3.14) and:

$$M_n = \left\lceil\frac{2\pi R_h[1+(\chi-1)\sin^{-\frac{2}{3}}(\vartheta_n)]}{c_o T_g}\right\rceil \geq N, \tag{3.33}$$

so that the elevation and azimuth sampling angles will be evaluated as:

$$\vartheta_n = \frac{2\pi n}{2N+1}, \tag{3.34}$$

$$\varphi_{n,m} = \frac{2\pi m}{2M_n+1}, \tag{3.35}$$

for each $m = -M_n, -M_n + 1, \ldots, M_n$ and $n = 1, 2, \ldots, N$. As discussed in [13], the CS representation is exact as far as $\mathbf{I}_S(\vartheta, \varphi, t)$ is strictly band limited to $2\pi\chi R_h/(c_o T_g)$. Anyway, aliasing errors due to unavoidable violation of such assumption can be controlled by proper selection of the excess bandwidth factor χ [13]-[14].In this work, χ will be set as $\chi = 1.1$.
Finally, the general time-variant spherical harmonic expansion coefficients $\boldsymbol{\psi}_{n,m} = [\boldsymbol{\alpha}_{n,m}(t)\ \boldsymbol{\beta}_{n,m}(t)]$ relevant to the surface equivalent currents can be evaluated by combining equations Eq.(3.30),Eq.(3.31) and Eq.(3.32) with Eq.(3.13) and after some algebra yields:

$$\begin{aligned}\boldsymbol{\psi}_{n,m}(t) =& \langle \mathbf{I}_S(\vartheta, \varphi, t), Y_n^m(\vartheta, \varphi)\rangle = \Lambda^+_{n,m}\hat{\mathbf{I}}^+_S + \Lambda^-_{n,m}\hat{\mathbf{I}}^-_S \\ &+ \sum_{\nu=1}^{N} \sum_{\mu=-M_\nu}^{M_\nu} \boldsymbol{\Phi}^{\nu,\mu}_{n,m} \mathbf{I}_S(\vartheta_\nu, \varphi_{\nu,\mu}, t),\end{aligned} \tag{3.36}$$

where:

$$\begin{aligned}&\boldsymbol{\Phi}^{\nu,\mu}_{n,m} = \langle \Pi_N(\vartheta - \vartheta_\nu)\Pi_{M_\nu}(\varphi - \varphi_{\nu,\mu}) - \Pi_N(\vartheta + \vartheta_\nu)\cdot \\ &\Pi_{M_\nu}(\varphi + \pi - \varphi_{\nu,\mu}), Y_n^m(\vartheta, \varphi)\rangle = \frac{1}{1+2N} \sum_{i=-N}^{N} \ell^{\nu,\mu}_{i,-m} \mathbf{Z}^i_{n,m},\end{aligned} \tag{3.37}$$

$$\Lambda^{\pm}_{n,m} = \langle \Pi_N(\vartheta) e^{\pm j\varphi}, Y_n^m(\vartheta, \varphi)\rangle = \frac{\delta_{m,\mp 1}}{1+2N} \sum_{i=-N}^{N} Z^i_{n,\mp 1}, \tag{3.38}$$

with $\delta_{i,k}$ being Kronecker's delta and:

$$\ell^{\nu,\mu}_{i,k} = \frac{e^{-j(i\vartheta_\nu + k\varphi_{\nu,\mu})} + (-1)^{k+1} e^{j(i\vartheta_\nu - k\varphi_{\nu,\mu})}}{1 + 2M_\nu} \tag{3.39}$$

$$\mathbf{Z}^i_{n,m} = \sqrt{\frac{(2n+1)(n-m)!}{(n+m)!}}\pi \int_{-1}^{1} [T_i(z) + jU_{i-1}(z) \cdot \sqrt{1-z^2}] P_n^m(z) dz, \tag{3.40}$$

It is worth noting that the symbolic computation of expansion coefficients $\Lambda^{\pm}_{n,m}, \Phi^{\nu,\mu}_{n,m}$ can be carried out before the time marching scheme starts. Indeed, in this research coefficients $\mathbf{Z}^i_{n,m}$ has been calculated once and storage for next computations of $\boldsymbol{\Lambda}^{\pm}_{n,m}$, $\boldsymbol{\Phi}^{\nu,\mu}_{n,m}$. In that way, computation time is saved since those coefficients would not change from one case of study to another.

3.3 Time-Domain Vector Fitting Procedure

Reached this point, let us focus on the modified pole/residue representation of the general time-variant spherical harmonic expansion coefficient $\boldsymbol{\psi}_{n,m} = [\boldsymbol{\alpha}_{n,m}(t)\, \boldsymbol{\beta}_{n,m}(t)]$ relevant to the surface equivalent currents excited on S_h:

$$\boldsymbol{\psi}_{n,m} = \sum_{k=1}^{K} \mathbf{c}_{n,m,k} e^{s_{n,m,k} t} u(t), \tag{3.41}$$

where $\mathbf{c}_{n,m,k} = [\mathbf{a}_{n,m,k}\ \mathbf{b}_{n,m,k}]$. Due to the vectorial nature of the residues $\mathbf{c}_{n,m,k}$, the matrix pencil method [15]-[16], or the modified Prony's algorithms can not be applied to perform the fitting of $\boldsymbol{\psi}_{n,m}(t)$ by complex exponential functions as in [11]-[12]. Therefore, to overcome this limitation, a dedicated non-conventional time-domain vector-fitting (TD-VF) has been specifically developed. This procedure, originally introduced in [8]-[10] to extract frequency-independent equivalent circuits of multiport interconnect structures, is aimed to the derivation of a rational approximation of the Laplace transform of $\boldsymbol{\psi}_{n,m}(t)$, that is:

$$\boldsymbol{\Psi}_{n,m}(p) = \mathcal{L}\{\boldsymbol{\psi}_{n,m}(t)\} = \sum_{k=1}^{K} \frac{\mathbf{c}_{n,m,k}}{p - s_{n,m,k}}. \tag{3.42}$$

To this end, a scalar weight function:

$$\boldsymbol{\Upsilon}_{n,m}(p) = 1 + \sum_{k=1}^{K} \frac{R_{n,m,k}}{p - q_{n,m,k}} = \frac{\prod_{k=1}^{K}(p - \zeta_{n,m,k})}{\prod_{k=1}^{K}(p - q_{n,m,k})}, \tag{3.43}$$

with assigned initial poles $\{q_{n,m,k}\}$ and unknown residues $\{R_{n,m,k}\}$ is introduced. In addition, it is assumed that the following approximation holds:

$$\boldsymbol{\Upsilon}_{n,m}(p)\boldsymbol{\Psi}_{n,m}(p) \simeq \sum_{k=1}^{K} \frac{\mathbf{M}_{n,m,k}}{p - q_{n,m,k}}. \tag{3.44}$$

Since the right-hand side term of Eq.(3.44) features the same complex poles $\{q_{n,m,k}\}$ as the weight function, a cancellation between the zeros $\{\zeta_{n,m,k}\}$ and the poles $\{s_{n,m,k}\}$ of $\{\boldsymbol{\Psi}_{n,m}(p)\}$ must occur. This afore-mentioned condition provides a way to estimate $\{s_{n,m,k}\}$ by solving in a least square sense, for the unknown residues $\{R_{n,m,k}\}$, the following time-domain equation:

$$\begin{aligned}\sum_{k=1}^{K}\mathbf{M}_{n,m,k} =&\mathcal{L}^{-1}\left\{\sum_{k=1}^{K}\frac{\mathbf{M}_{n,m,k}}{p-q_{n,m,k}}\right\} \simeq \mathcal{L}^{-1}\left\{\Upsilon_{n,m}(p)\boldsymbol{\Psi}_{n,m}(p)\right\}\\ =&v_{n,m}(t) * \boldsymbol{\psi}_{n,m}(t) = \boldsymbol{\psi}_{n,m}(t) + \sum_{k=1}^{K} R_{n,m,k}\Theta_{n,m,k}(t),\end{aligned} \tag{3.45}$$

where $v_{n,m}(t) = \mathcal{L}^{-1}\{\ \Upsilon_{n,m}(p)\}$, and:

$$\boldsymbol{\Theta}_{n,m,k}(t) = \mathcal{L}^{-}1\left\{\frac{\boldsymbol{\Psi}_{n,m}(p)}{p-q_{n,m,k}}\right\} = \int_0^t e^{q_{n,m,k}(t-t')}\psi_{n,m}(t')dt' \tag{3.46}$$

is the transient waveform resulting from the inverse Laplace transform of the k-th partial fraction term appearing on the left-hand side of expansion Eq.(3.44). The convolution integral in Eq.(3.46) can be accurately approximated by applying a suitable discretization of the convolution integrals. We use here a linear interpolation between the raw samples, leading to:

$$\boldsymbol{\Theta}_{n,m,k}(t) \simeq \alpha_n\boldsymbol{\Theta}_{n,m,k}(t_k) + \beta_n^{(0)}\psi_{n,m}(t_{k+1}) + \beta_n^{(1)}\psi_{n,m}(t_k), \tag{3.47}$$

with weighting coefficients:

$$\alpha_n = e^{q_n\Delta t}, \tag{3.48}$$

$$\begin{aligned}\beta_n^{(0)} &= \frac{-1-q_n\Delta t+\alpha_n}{q_n^2\Delta t},\\ \beta_n^{(1)} &= \frac{1+(q_n\Delta t-1)\alpha_n}{q_n^2\Delta t},\end{aligned} \tag{3.49}$$

$t_k = k\Delta t$ denoting the time sample where k is the sample and Δt is the time step adopting in the full-wave numerical procedure to evaluate the spatial distribution of the electromagnetic field along surface S_h. In the next chapter it will be pointed out the criteria followed to set this parameter.

Since the evaluation of the residues $\{R_{n,m,k}\}$ is performed, the poles can be determined by enforcing $s_{n,m,k} = \zeta_{n,m,k}$, where the zeros $\{\zeta_{n,m,k}\}$ are computed using known matrix algebra theory. The described method, known as *pole relocation* avoids the use of ill-conditioned non linear least squares methods for the direct fitting of Eq.(3.41) and Eq.(3.42). In particular, the pole relocation can be iterated using the estimated poles $\{s_{n,m,k}\}$ as initial poles $\{q_{n,m,k}\}$ of the scalar weight function $\Upsilon_{n,m,k}(p)$ at the next iteration. The resulting procedure is stable by construction, but might be non passive due to the least squares solution of Eq.(3.45), which does not guarantee passivity a priori. Therefore, in order to avoid instability of the model, the passivity must be checked and enforced at each iteration if unstable poles appear:

$$\sigma_{n,m,k} = -|Re\{s_{n,m,k}\}|, \tag{3.50}$$

for all indexes n, m, k. The convergence of the described procedure is usually obtained in a few iterations but it depends on the election of the starting poles along the frequency spectra. In order to provide a nice accuracy in the exponential fitting the stop criterion for the pole relocation loop is set as:

$$\frac{\sum_{k=1}^{K} |s_{n,m,k} - q_{n,m,k}|^2}{\sum_{k=1}^{K} |q_{n,m,k}|^2} < \varepsilon^2, \tag{3.51}$$

where ε is a suitable convergence parameter. It is must be a trade-off between accuracy and computation time. In this research, ε is selected to be equal to 10^{-3} in the numerical procedure. Finally, once the poles $\{s_{n,m,k}\}$ are known, the vector residues $\{\mathbf{c}_{n,m,k}\}$ can be evaluated by solving Eq.(3.41) in a least square sense. In addition, the set of poles and residues to be used for the evaluation of the radiated electromagnetic field distribution in time domain can be reduced according to the level of the *energy* indicators defined as follows:

$$\boldsymbol{\varepsilon}_{n,m,k} = \frac{1}{\eta_0} \int_0^{+\infty} |e^{s_{n,m,k}\tau} \mathbf{e}_{n,m,k}|^2 d\tau. \tag{3.52}$$

Therefore, summation in Eq.(3.20) will be restricted to those poles among all the $\{s_{n,m,k}\}$ whose energy level $\boldsymbol{\varepsilon}_{n,m,k}$ satisfies the condition $\boldsymbol{\varepsilon}_{n,m,k}/\boldsymbol{\varepsilon}_{max} \geq \delta_{\varepsilon}$, where $\boldsymbol{\varepsilon}_{max} = \mathrm{max}_{\mathrm{n,m,k}}\{\boldsymbol{\varepsilon}_{\mathrm{n,m,k}}\}$ and δ_{ε} is a given threshold. In order to achieve a reasonable numerical accuracy, δ_{ε} might be set to 10^{-3}. In this work, this threshold will be set to larger values in the pole distribution analysis phase, in order to retrieve those poles more meaningful involved in the resonant processes occurring in the structures under study.

Chapter 4

Simulation Tools

The aim of this chapter is to present the different software tools used during the whole thesis work. In addition, it will be pointed out the criteria considered to decide between the possibilities available. Firstly, two different simulation tools were considered: CST Microwave Studio and FEKO. Both were suitable in the case of study but only one has been chosen for the thesis work. Finally, after a brief study and discussion the software chosen for the full-wave time-domain computation was CST Microwave Studio 2009. Besides, all the equations and procedures described in previous chapters have been carried out using Matlab 7.5.0 (R2007b) developed by *The Mathworks*.

4.1 Software Characteristics

As mentioned, two simulation tools were available in order to evaluate electromagnetic fields excited over a certain surface enclosing a radiator structure, CST Microwave Studio and FEKO. Although both possibilities allow us to compute the electromagnetic fields excited over a spherical surface, there are several differences between them. Firstly, different methods are used to approximate Maxwell equations. While CST is using the finite integration technique (FIT) that actually, for Cartesian grids can be rewritten as a standard finite difference time domain (FDTD) method, FEKO uses the method of moments (MoM).

So, CST includes a transient solver that provides directly the electromagnetic fields values in time domain, whereas FEKO does not have this solver and the collected data should be transformed from frequency to time domain. Using CST Fourier transform implementation is avoided. Besides, a post-processing template is already done in CST which allow us to evaluate the electromagnetic fields along a sphere by fixing a radius from the axes origin. However, it is not possible to control the location of the spatial points. This limitation is overcome as discussed in Chapter 3 by using a IDW interpolation technique to evaluate the electromagnetic field at any discrete point along Huygens sphere. In FEKO could be possible to select the specific sampling points, but assuming the drawback of getting the data in frequency domain. In addition, since CST use Gaussian pulse as excitation signal a proper wide-band study can be done. Actually, FDTD is the preferred method for wideband systems. Finally, by reason of the matters aforesaid CST has been chosen as simulation tool for the analysis of the antennas under study.

4.1.1 FDTD/FIT Method

Since CST is based on the FIT technique, a brief study of its fundamentals characteristics should be done. Unlike most numerical methods, FIT discretizes the integral form of Maxwell's equations instead of the differential one. In order to evaluate Maxwell's equations numerically a finite calculation domain enclosing the application problem is considered. Then, this space domain is split up in small elements (see Fig.4.1). Next, Maxwell's equations are formulated and evaluated for each element as shown in Fig.4.2 [21].

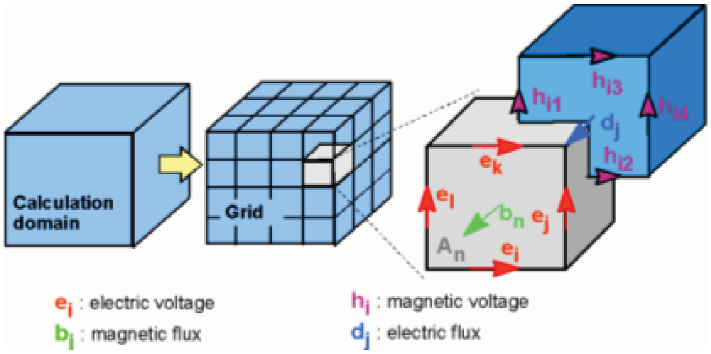

Figure 4.1: Calculation domain and grid cell in CST

In this research, CST Microwave Studio has been used basically for computation of electromagnetic fields in time domain. To this end, a transient

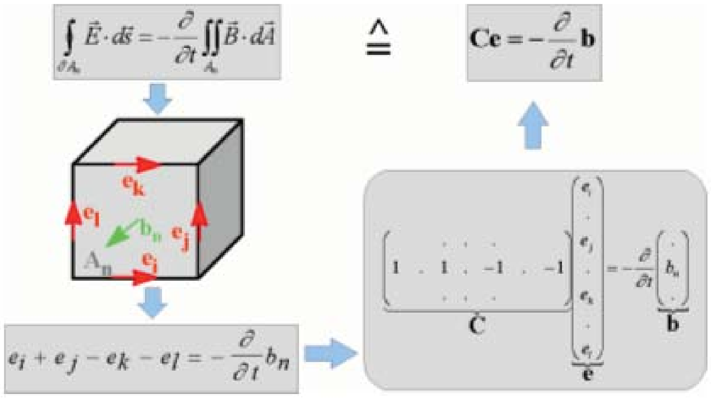

Figure 4.2: Formulation and discretization of Maxwell's equations in CST

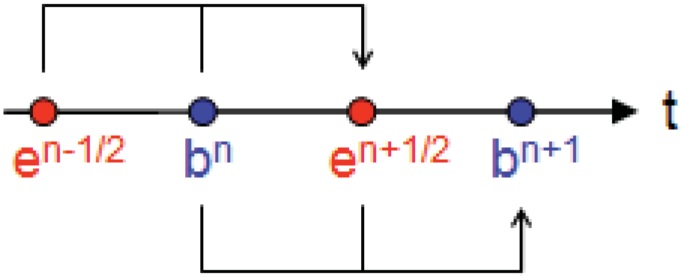

Figure 4.3: Schematic drawing of time domain sampling in CST

solver has been utilized. In Fig.4.3 can be shown how CST evaluates the magnetic flux from the magnetic flux at the previous time-step and the electric voltage at half a time-step before. Finally, as mentioned before FIT can be rewritten as a FDTD technique. Then, a brief review pointing out the strong points and weaknesses of this method will be done. The strong points of the FDTD are the following [18]:

- Simple implementation for a full-wave solver.
- Straightforward treatment of material inhomogeneities.
- Fairly accurate geometrical modeling ability.
- Wideband data potentially available in one run (time domain method).

Since in this research a commercial software already developed has been used only the fourth point may be highlighted. On the other hand, the main drawbacks are the following:

- Inflexible meshing.
- Uncertainty about the precise position of boundaries.
- Dispersive materials require considerable effort to implement correctly.
- Less efficient than MoM when modeling entirely or highly conducting radiators.

4.2 Matlab

In this research several mathematical tools and equations has been presented so far. As usually, an interface between equations written down in papers and computers "language" must be used. In this case, all the routines involving the two-step data fitting procedure mentioned in Chapter 3 have been developed and tested with the well-known software tool Matlab (2007b version specifically). Therefore, most of the charts and graphics presented in this work have been carried out in this software tool.

Matlab, as its name says works mainly with matrix. This functionality allow engineers to treat a wide range of problems in a fast and accurate way. Nevertheless, in order to achieve a high performance there are some issues to take into account:

- Try to avoid *while* and *for* loops and use instead matrix systems.
- Regarding how Matlab reserves memory for new variables is convenient to define previously each variable as zero values of the size desired.
- Although Matlab can operate with symbolic variables its performance is not as good as other simulation tools.

Those tips have been kept in mind during this work but unfortunately sometimes the usage of symbolic variables and *for* loop was unavoidable and therefore the computation time of some functions is affected.

Chapter 5

Numerical Procedure

The aim of this chapter is to provide the reader a practical way to carry out the procedure developed in Chapter 3. Numerical procedures and parameters selected should be studied thoroughly in following pages.

5.1 Evaluating Density currents

As pointed out earlier, in order to compute electromagnetic fields CST Microwave Studio has been chosen as software tool. Different antennas have been built in the simulation tool and a special post-processing template result has been used in order to evaluate electromagnetic fields along Huygens Sphere. Before proceeding with the simulation several parameters and issues must be taken into account:

Gaussian Pulse: Proper selection of the excitation signal. It must be stressed that the same pulse should be considered for each sort of antenna. In other words, all dipole antennas will be excited by the same Gaussian pulse. Anyway, this issue will be discussed later in each antenna case.

Huygens Radius: Selection of R_h, Huygens radius parameter.

Time-step: Selection of time-step for the electromagnetic fields computation in time domain.

In Fig.5.1 it can be seen the spatial grid used in CST to evaluate the electromagnetic fields excited along Huygens sphere. Unfortunately, it is not

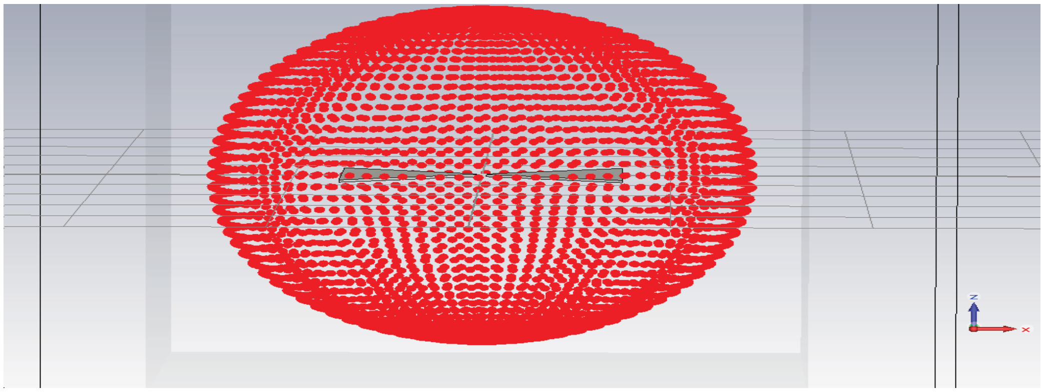

Figure 5.1: CST image of a bow-tie antenna within Huygens Sphere. Red picks denote the sampling points where electromagnetic fields are evaluated

possible to fix those sampling points manually in order to evaluate the electromagnetic fields at the observation points of interest given by Eq.(3.34)-Eq.(3.35) (see Sec.(3.2)). However, this limitation can be overcome by applying a Inverse Distance Weighting (IDW) interpolation technique. To this end, a Matlab routine has been implemented which taking CST data (electromagnetic fields and spatial coordinates of the evaluated points) as input, provides electromagnetic fields distribution at the observation points desired. By adopting a weighting function such as $w(R) = |R|^{-2}$ where R is the distance between the computed and the observation points, the summation is carry out over the n (parameter selected by the user) nearest field samples from the observation point. Parameter n has been chosen to be as 4, 8... depending on the number of field values and observation points. Generally, CST grid is well-fitted and therefore the number of field values are larger than the observation points needed.

Once electromagnetic fields at desired points are known, density currents can be easily carried out by performing Eq.(3.2). It must be noticed that electromagnetic fields time distributions collected are expressed in Cartesian components and therefore, in order to evaluate Eq.(3.2) unit vector $\hat{\mathbf{r}}$, must be expressed as follows:

$$\hat{\mathbf{r}} = \sin\theta\cos\phi\hat{\mathbf{x}} + \sin\theta\sin\phi\hat{\mathbf{y}} + \cos\theta\hat{\mathbf{z}} \tag{5.1}$$

5.1.1 Huygens Radius

Firstly, it must be noticed that the antenna must be enclosed by this spherical surface namely Huygens sphere. Therefore, the Huygens radius must be at least half of the maximum overall dimension. It is worth pointing out that this becomes true as long as the drive point of the antenna is centered on the Huygens sphere. Nevertheless, that is the case under study in most part of the work. So, in order to avoid strange results at the end fire of the antennas under study (such as poles in the half-wavelength dipole), a $\lambda/4$ length will be added to the half of the maximum overall dimension distance.

5.1.2 Time-step

A proper value of the time-step adopted of the full-wave numerical procedure must be selected. Since the excitation signal is a narrow Gaussian pulse, usual Nyquist criteria $\Delta t = 1/2f_{max}$ does not provide enough smoothness in the waveforms obtained. In order to get smoother representations of the field distribution in time domain, another criteria must be taken into account. Therefore, a good approach could be to ensure that at least ten time-samples are considered in the raising slope of the time Gaussian excitation. To this end, the FWHM of the time excitation signal was measured in CST and divided by 10 (see Fig.5.2). However, in some cases where the size of the antenna simulated is large compare to the wavelength of the highest frequency of the excitation signal, this condition is relaxed due to the large amount of memory space and computation time needed.

5.2 Expansion Coefficients

As discussed in previous chapters, N parameter is selected to be according to the theory of optimal spherical interpolation of radiated electromagnetic fields as Eq.(3.14). Having already discussed R_h selection , attention should be paid now to the bandwidth excess factor χ and pulse-length parameter T_g. Given the expansion order, the next step will consist of evaluating the expansion coefficients outlined in equations Eq.(3.37)-Eq.(3.40).

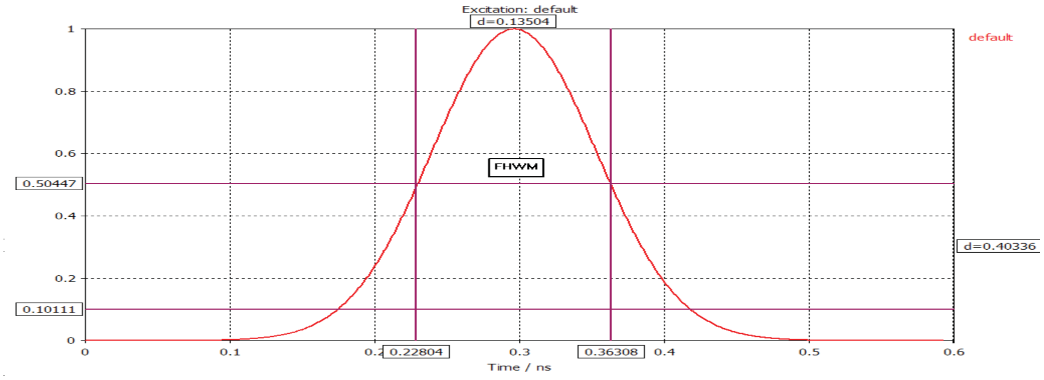

Figure 5.2: Excitation Signal used in CST. The FHWM highlighted is divided by a factor of 10.

5.2.1 Excess bandwidth factor χ

Excess bandwidth factor χ as discussed in [13], is used to control the approximation error which decreases more than exponentially with $\chi - 1$. In this research, regarding literature about the topic and looking for a compromise between accuracy and computation time χ factor has been set to be equal to 1.1.

5.2.2 T_g parameter

T_g is the pulse length of the antenna excitation signal. A study of this parameter in terms of accuracy and time computation should be done. Different T_g can be chosen depending on the energy cut limit set in the Gaussian pulse. For instance, 50 %, 90 %, 95 % of Gaussian pulse energy might be reasonable energy levels to look at. In [20] T_g is set as five times the characteristic time of the Gaussian pulse, which means that almost the 100 % of the energy is taken into account. Following, some numerical results are presented in different tables. Those results has been obtained from a excitation signal selected as follow:

- Non derivative Gaussian pulse.
- Characteristic time: $\tau = 6.33e^{-11}$ s.
- FWHM: $1.05e^{-10}$ s.

Criteria	T_g (ns)
50 %	0.10371
90 %	0.19003
95 %	0.21754
5τ	0.31650

Table 5.1: Results of T_g pulse-length parameter for different criteria

In Tab.(5.1) T_g values are shown corresponding with different criteria. In Eq.(5.2) and Tab.(5.3) different values are presented. This experiment has been done considering a half-wave dipole antenna. Frequency tab denotes the operation frequency and R_h denotes the Huygens radius considered. N1, N2,N3 and N4 correspond with different T_g selection criteria previously mentioned. Indeed, being more restrictive at setting T_g parameter more accurate results will be obtained. However, computation time will increase since the number of expansion coefficients and sampling points is larger. In Fig.5.3 it can be seen the relation between those parameters and expansion order N. It can be derived that computation time increases exponentially as expansion order N does. Therefore, a proper selection of N should be done. In dipole antennas where the radiation patterns are simple and symmetrical T_g selection can be done in the less restrictive way ($T_g = 5\tau$). On the other hand, more complicated structures may need a expansion order N larger enough in order to achieve fair results.

Frequency (GHz)	$R_h = \lambda/2$ (m)	N1	N2	N3	N4	Number of time-coefficients			
						N1	N2	N3	N4
6	0.025	6	4	3	2	49	25	16	9
3	0.05	12	7	6	4	169	64	49	25
1	0.15	34	19	16	11	1225	400	289	144
0.3	0.5	112	61	53	37	12769	3844	2916	1444

Table 5.2: Number of time-variant coefficients to evaluate for different T_g criteria selection and R_h.

Frequency (GHz)	$R_h = \lambda/2$ (m)	N1	N2	N3	N4	Number of sampling points			
						N1	N2	N3	N4
6	0.025	6	4	3	2	80	36	21	10
3	0.05	12	7	6	4	310	107	80	36
1	0.15	34	19	16	11	2496	777	568	275
0.3	0.5	112	61	53	37	27270	8101	6159	2965

Table 5.3: Number of sampling points needed for different T_g criteria selection and R_h.

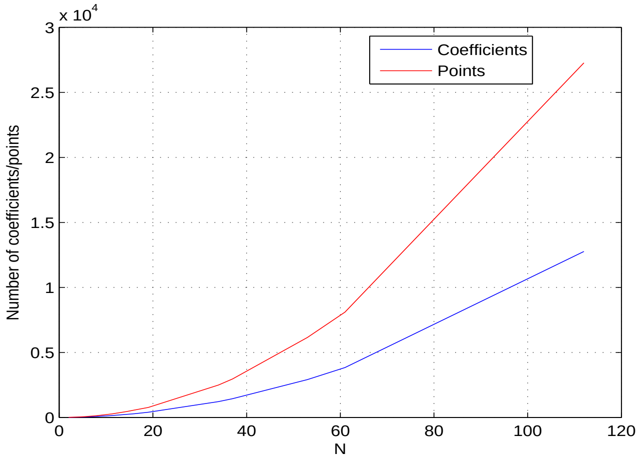

Figure 5.3: Dependence of the number of coefficients/sampling points on the expansion order N

5.2.3 $\Lambda^{\pm}_{n,m}$ and $\Phi^{\nu,\mu}_{n,m}$ coefficients

Recalling Eq.(3.37)-Eq.(3.40) it is worth nothing that the symbolic computation of $\Lambda^{\pm}_{n,m}$ and $\Phi^{\nu,\mu}_{n,m}$ can be conveniently carried out before the time marching scheme starts. In that way, it might be inferred that $Z^{i}_{n,m}$ coefficients can be evaluated once and then just taking the appropriate number of them according to parameter N. It is worth noting that the symmetry property of spherical harmonics allows us to compute positive m indexes only. Therefore, taking advantage of latter property $Z^{i}_{n,m}$ coefficients have been evaluated uniquely for m going from 0 to n (only positive values) for an expansion order N=37 which ensures a wide range of coefficients possibly needed. This would save us a considerable amount of time. Once $\Lambda^{\pm}_{n,m}$ and $\Phi^{\nu,\mu}_{n,m}$ are evaluated they must be properly combined with the density currents excited along Huygens sphere. Regarding Matlab recommendations in Sec.(4.2), summation in Eq.(3.36) can be carried out as a common matrix product.

$$\boldsymbol{\psi'}_{n,m}(t) = \sum_{\nu=1}^{N} \sum_{\mu=M_\nu}^{M_\nu} \Phi_{n,m}^{\nu,\mu} \mathbf{I}_S(\vartheta_\nu, \varphi_{\nu,\mu}, t) \tag{5.2}$$

Thus, by building conveniently a matrix with every single value of $\Phi_{n,m}^{\nu;\mu}$ as described in Tab.(5.4), Eq.(5.2) can be rewritten as:

$$\begin{array}{cccc} \{\Phi_{n,m}^{\nu,\mu}\} & \{\mathbf{I}_S(\vartheta_\nu, \varphi_{\nu,\mu}, t)\} & = & \{\boldsymbol{\psi'}_{n,m}\} \\ L \times K & K \times T & & L \times T \end{array} \tag{5.3}$$

Being K the number of sampling points, L the number of coefficients and T the number of time-steps. As shown in Tab.(5.4), $\Phi_{n,m}^{\nu,\mu}$ is organized by columns according to the sampling points and by rows according to the time-variant spherical harmonic expansion coefficient indexes (going from $n = 1$ to $n = N$ and from $m = -n$ to $m = n$). Once reached this point, let us focus now in $\Lambda_{n,m}^{\pm}$ evaluation. Looking at Eq.(3.38) and being Kronecker's delta defined as:

ϑ_ν	$\varphi_{\nu,\mu}$	$\Phi_{n,m}^{\nu,\mu}$					
		(0,0)	(1,-1)	(1,0)	(1,1)	$\cdots$	(n,m)
$\vartheta_\nu(1)$	$\varphi_{\nu,\mu}(1, -M_\nu)$	x	x	x	x	$\cdots$	x
$\vartheta_\nu(1)$	$\varphi_{\nu,\mu}(1, -M_\nu + 1)$	x	x	x	x	$\cdots$	x
$\vartheta_\nu(1)$	$\cdots$	x	x	x	x	$\cdots$	x
$\vartheta_\nu(1)$	$\varphi_{\nu,\mu}(1, M_\nu - 1)$	x	x	x	x	$\cdots$	x
$\vartheta_\nu(1)$	$\varphi_{\nu,\mu}(1, M_\nu)$	x	x	x	x	$\cdots$	x
$\cdots$	$\cdots$	x	x	x	x	$\cdots$	x
ϑ_ν(N)	$\varphi_{\nu,\mu}(N, -M_\nu)$	x	x	x	x	$\cdots$	x
ϑ_ν(N)	$\cdots$	x	x	x	x	$\cdots$	x
ϑ_ν(N)	$\varphi_{\nu,\mu}(N, M_\nu)$	x	x	x	x	$\cdots$	x

Table 5.4: Matrix construction of $\Phi_{n,m}^{\nu,\mu}$ coefficients. Observation points are given by rows and the spherical harmonic orders are given by columns.

$$\delta_{i,j} = \left\{ \begin{array}{ll} 1, & \text{if i} = \text{j} \\ 0, & \text{if i} \neq \text{j} \end{array} \right\} \tag{5.4}$$

again it only worth computing a certain number of coefficients since most of them will be equal to zero. Now, attention must be paid to:

$$\begin{aligned}\boldsymbol{\psi}''_{n,m}(t) &= \Lambda^{+}_{n,m}\hat{\mathbf{I}}^{+}_{S}(t)\\ \boldsymbol{\psi}'''_{n,m}(t) &= \Lambda^{-}_{n,m}\hat{\mathbf{I}}^{-}_{S}(t)\end{aligned} \tag{5.5}$$

According to Eq.(3.32) dependence on φ azimuth angle goes with the exponential function. Then, $\hat{\mathbf{I}}^{+}_{S}(t)$ and $\hat{\mathbf{I}}^{+}_{S}$(t) must be a function varying in time. Performing spherical-to-rectangular transformation when $\vartheta = 0$ and using Euler's formula yields to:

$$\begin{aligned}\hat{\mathbf{I}}^{+}_{S_x} &= \tfrac{I_\vartheta}{2} - \tfrac{I_\varphi}{2j} \quad & \hat{\mathbf{I}}^{-}_{S_x} &= \tfrac{I_\vartheta}{2} + \tfrac{I_\varphi}{2j}\\ \hat{\mathbf{I}}^{+}_{S_y} &= \tfrac{I_\vartheta}{2j} + \tfrac{I_\varphi}{2} \quad & \hat{\mathbf{I}}^{-}_{S_y} &= -\tfrac{I_\vartheta}{2j} + \tfrac{I_\varphi}{2}\end{aligned} \tag{5.6}$$

Then, handling properly Eq.(5.5) results are same-size matrix as Eq.(5.2). Consequently, final time-variant spherical harmonic expansion coefficients are evaluated as simple matrix summations:

$$\boldsymbol{\psi}_{n,m}(t) = \boldsymbol{\psi}'_{n,m}(t) + \boldsymbol{\psi}''_{n,m}(t) + \boldsymbol{\psi}'''_{n,m}(t) \tag{5.7}$$

5.3 Pole Relocation Procedure

Having already evaluated time-variant spherical harmonic expansion coefficient, pole relocation technique implementation should be discussed. In Sec.(3.3) analytical description of the procedure has been discussed. One might reach to the conclusion that the critical point lies on the least square problem. Therefore, this part of the implementation as well as different parameters chosen should be thoroughly discussed in next pages. In this research, it has been taken as reference previous implementations of this technique in frequency domain and scalar functions [22]-[24] though. It must be remembered that in this study this technique should work in time-domain and handling vectorial functions.

5.3.1 Least Square problem

As pointed out earlier in this chapter, the pole relocation technique derives at the end to a least square problem sense as shown in Eq.(3.45). Handling latter equation it can be expressed readily in a more clear way as:

$$\begin{pmatrix} e^{q_{n,m,1}t_1} & \cdots & e^{q_{n,m,K}t_1} & -\Theta_{n,m,1}(t_1) & \cdots & -\Theta_{n,m,K}(t_1) \\ . & & . & . & & . \\ e^{q_{n,m,1}t_j} & \cdots & e^{q_{n,m,K}t_j} & -\Theta_{n,m,1}(t_j) & \cdots & -\Theta_{n,m,K}(t_j) \\ . & & . & . & & . \\ e^{q_{n,m,1}t_T} & \cdots & e^{q_{n,m,K}t_T} & -\Theta_{n,m,1}(t_T) & \cdots & -\Theta_{n,m,K}(t_T) \end{pmatrix} \begin{pmatrix} \mathbf{M}_{n,m,1} \\ . \\ . \\ . \\ \mathbf{M}_{n,m,K} \\ \mathbf{R}_{n,m,1} \\ . \\ . \\ . \\ \mathbf{R}_{n,m,K} \end{pmatrix}$$

$$= \begin{pmatrix} \boldsymbol{\psi}_{n,m}(t_1) \\ . \\ . \\ . \\ \boldsymbol{\psi}_{n,m}(t_j) \\ . \\ . \\ . \\ \boldsymbol{\psi}_{n,m}(t_T) \end{pmatrix} \tag{5.8}$$

where $k = 1, ..., K$ is the pole index being K the number of total poles, and t_j , $j = 1, ..., T$ being t_j the time-step and T the total time. As it can be noticed, Eq.(5.8) resembles to $[A][x] = [b]$ matrix system. It is worth noting that a vector function is fitting, then $[A]$ and $[b]$ outlined in Eq.(5.8) must be repeated for each vector component. In this case, since Cartesian components are used, the time-variant harmonic expansion coefficients have six components (belonging to electric and magnetic density currents in Cartesian components). Therefore, fitted vector components of time-variant coefficients will be expressed as a summation of exponential functions sharing the same poles $s_{n,m,k}$ and of course, having different residues values $\mathbf{c}_{n,m,k} = [\mathbf{a}_{n,m,k}\ \mathbf{b}_{n,m,k}]$ Thus, solving Eq.(5.8) unknown residues $R_{n,m,k}$ become known values and then calculating zeros in Eq.(3.43) is feasible. Those zeros can be evaluated as the eigenvalues of the matrix:

$$H = A - b\tilde{c}^T \tag{5.9}$$

where A is a diagonal matrix containing the starting poles and b is a column vector of ones. $\tilde{c}^T$ is a row-vector containing the residues previously calculated $R_{n,m,k}$. Dealing with complex pair of poles the corresponding submatrices are modified as follows:

$$\hat{A} = \begin{bmatrix} a' & a'' \\ -a'' & a' \end{bmatrix}, \hat{b} = \begin{bmatrix} 2 \\ 0 \end{bmatrix}, \hat{c} = [\tilde{c}' \; \tilde{c}''] \tag{5.10}$$

denoting superscripts ’ and ” real and imaginary part respectively. This modification has the effect that H becomes a real matrix and so its complex eigenvalues come out as perfect complex conjugate pairs. Then, once poles $s_{n,m,k}$ are known, the vector residues $\mathbf{c}_{n,m,k}$ can be readily determined by solving Eq.(3.41) in a least square sense.

As discussed in Sec.(3.3), this procedure is iterating until the stop criterion in Eq.(3.51), governed by ε and selected to be equal to 10^{-3}, is satisfied.

5.3.2 Pole Order K

Proper selection of expansion order K is not a clear issue at the moment. Despite in [25] it is proposed the WT rule $(K = WT)$, being W the frequency bandwidth of the excitation signal and T the duration over the response is desired, in this research K has been set heuristically. In that way, a certain degree of accuracy in the modeling of resonant processes occurring in the antennas is achieved.

5.3.3 Starting poles selection

In order to save computation time a proper selection of initial poles in the pole relocation technique must be considered. As pointed out in [22]-[24] for functions with resonance peaks, the initial poles should be complex conjugate with weak attenuation and imaginary parts covering the frequency range of interest. The weak attenuation assures that the least square sense problem to be solved has a well-conditioned system matrix. In addition, the distribution of the pairs over the frequency range will decrease the probability that poles are relocated long distances in the complex plane. The pairs should normally be chosen as follows :

$$a_n = -\alpha + j\beta, \;\; a_{n+1} = -\alpha - j\beta \tag{5.11}$$

where

$$\alpha = \beta/100, \tag{5.12}$$

Typically, β is specified to be linearly spaced over the frequency range of interest

5.3.4 Coefficients filtering

Poles filtering according to its energy level has been considered to the final evaluation of radiated field as described in Sec.(3.3). In this research, a priori filtering of the time-variant coefficients has also been considered. Since some harmonics account in higher levels than others one might think to consider only those ones with a certain energy level.

$$\Gamma_{n,m} = \int_o^\infty ||-\eta_0 \psi^J_{n,m}(t) + \psi^M_{n,m}(t)||dt \tag{5.13}$$

being $\psi^J_{n,m}(t)$ and $\psi^M_{n,m}(t)$ time-variant spherical harmonic coefficients accounting for electrical current (superscript J) and magnetic current (superscript M) respectively. Then, those harmonics whose energy level holds $\Gamma_{n,m}/\Gamma_{max} > \delta$ being δ a fixed threshold, are retrieved.

Chapter 6

Dipole Antenna

In this chapter transient radiation of a dipole antenna should be thoroughly studied. Using the formalism described in previous chapters for the electromagnetic fields representation, poles distribution in the complex plane must be analyzed. This task will be done for different dipoles antennas by varying its physical parameters such as length of the dipole and thickness of the wire.

6.1 Geometry

Dipole antenna is for many reasons one of the most versatile antenna in RF applications. It simple geometry provides radiation patterns easily derived from mathematical equations. In this research, half-wavelength dipole antenna oriented along z axis would be considered (see Fig.6.1). Regarding dipole configuration two physical parameters can be readily taken in consideration: length of the dipole l and radius of the wire a.

Half-wavelength dipole $\lambda/2$ is meant to resonate at frequency corresponding with λ. By increasing the length of the dipole and keeping the same excitation signal (Gaussian pulse) more resonances will occur at different frequencies such as $3\lambda/2, 5\lambda/2$... (see Fig.6.2). In terms of transient radiation, as the length of the dipole increases the traveling time of the Gaussian pulse along the wire also increases. Moreover, the reflections occurred at the end fires and source point will cover more distance and then consequences in transient radiation would be observed.

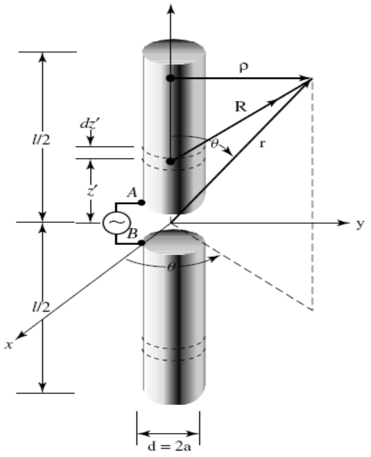

Figure 6.1: Dipole antenna configuration.

6.2 Gaussian Pulse selected

Recalling 2.2.2 and [1] the Gaussian pulse selected was set to be as $\tau/\tau_a = 0.076$ in a way that four pulses fit in one arm of the dipole. Proceeding like this, wavefronts originated from reflections at end fire terminations of the dipole are easily noticed. Taking a look to equations Eq.(6.1)-Eq.(6.3) the pulse width in frequency domain will be set. It is evaluated for a dipole operating at the lower limit of the frequency range, 0.3 GHz. In Tab.(6.1), f_{max} refers to the maximum simulation frequency set up in CST Microwave Studio.

$$\tau/\tau_a = 0.076, \tau_a = h/c_0 \tag{6.1}$$

$$FWHM = 2\sqrt{\ln 2}\tau \tag{6.2}$$

$$g(t) = I_s e^{-(t/\tau)^2} \xrightarrow{TF} G(f) = I_s e^{-(f\tau\pi)} \tag{6.3}$$

$h = \lambda/4$ (m)	Frequency (GHz)	τ_a (ns)	τ (ns)	f_{max}(GHz)	FWHM (ns)
0.25	0.3	8.33 e^{-1}	6.33 e^{-2}	7.63	1.05 e^{-1}

Table 6.1: Pulse excitation signal parameters.

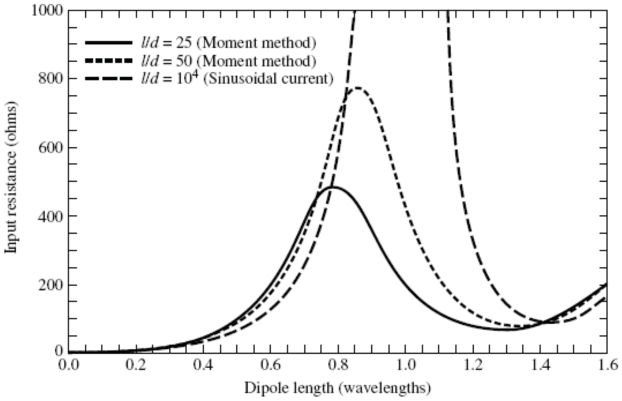

(a) Input resistance

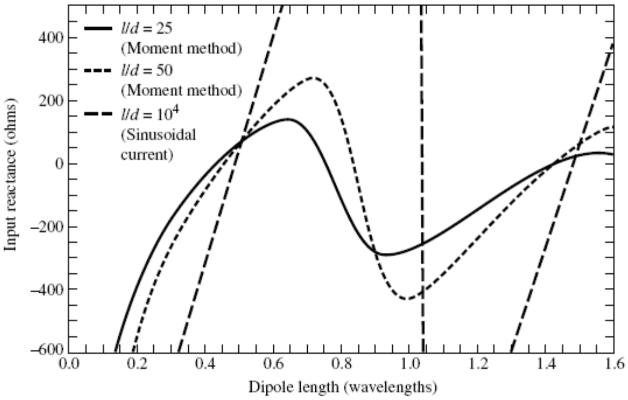

(b) Input reactance

Figure 6.2: (a) Input resistance and (b) reactance of wire dipoles.

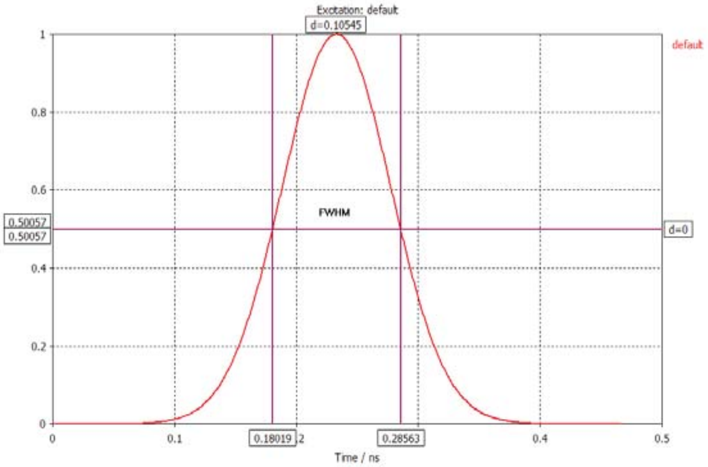

Figure 6.3: Gaussian Pulse selected. FHWM=0.10545 ns

where τ is the characteristic time, τ_a is the time for light to travel the arm of the dipole being h the length of the arm and c_0 the speed light. From a brief study of how CST excitation signals are built, it was inferred that CST Microwave Studio set as maximum simulation frequency the -10 dB cut-off frequency. Thus, handling properly equations in Eq.(6.1)-Eq.(6.3), knowing the characteristic time desired the cut off frequency can be obtained performing Fourier Transform and working out its value. Therefore by setting in CST as minimum frequency 0 GHz and as maximum 7.63 GHZ the excitation signal obtained is shown in Fig.6.3. As it can be observed FHWM value is equivalent to the one obtained in Tab.(6.1).

6.3 Arm-length study

Reached this point where the excitation signal is fixed for the dipole antenna, a physical parameter of such structure must be studied. It can be easily inferred that the length of the arm has direct relation with radiation patterns in frequency domain as well as in time domain. Thus, poles distribution of pole/residue version of radiated fields must change according to the length of the antenna. As commented in Sec.(6.1), the characteristic time τ of the Gaussian pulse is fixed following afore-mentioned criteria. Then, increasing h, arm-length of the dipole, relation τ/τ_a being $\tau_a = h/c_0$ will change and consequently radiation behavior of the structure (see Fig.6.4 and Tab.(6.2)).

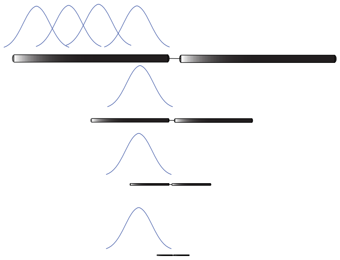

Figure 6.4: Scheme drawing of different dipole antennas with various arm-length/pulse-length ratio.

Dipole-length $l = \lambda/2$ (m)	Operating Frequency (GHz)	τ/τ_a
0.5	0.3	0.076
0.15	1	0.253
0.05	3	0.760
0.025	6	1.52

Table 6.2: Dipole-length and pulse-length relation.

6.3.1 Poles Distribution in frequency complex plane

As it can be observed in Fig.6.5 resonances occur at roughly the frequencies desired. Actually, resonance in 6 GHz dipole is occurring at 5.5 GHz and in 3 GHz dipole at 2.75 GHz and so on... This shifting phenomena is due to resonance does not appear exactly at 0.5λ but does at $0.47\lambda - 0.48\lambda$. Moreover, inaccuracies in the time-domain solver can derive in this shifting phenomena. Anyway, as could be expected as long as the length of the dipole increases more resonances arise.

Let us now focus the attention in the pole distribution of those structures. As discussed along this thesis, radiated field can be expressed in terms of

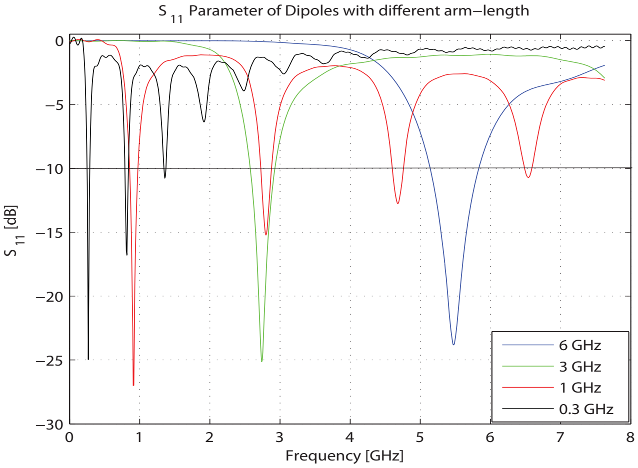

Figure 6.5: S_{11} parameter of half-wave dipoles operating at different frequencies.

complex exponential functions which real part accounts for the attenuation phenomena. Moreover, the imaginary part of this poles will have to do with the resonances occurring in the resonating structures. Looking at Fig.6.6, it can be pointed out several comments. Poles enclosed by ellipses are the dominant ones since they own the smallest damping coefficients. As it can be seen, dominant poles are situated roughly at resonant frequencies: $f_{6GHz} \simeq 5 - 6GHz$, $f_{3GHz} \simeq 2.5 - 3GHz$, $f_{1GHz} \simeq 1GHz$ ... In addition, glancing at Fig.6.5 it can be noticed that 3GHz and 1GHz dipoles share a impedance matching region. This can be also noticed in Fig.6.6 since the second group of dominant poles of 1GHz dipole support this resonant behavior at the frequency of 3 GHz. Unfortunately, dominant poles of the 0.3 GHz dipole can not be appreciated properly. Its extremely low damping coefficients do not allow to compare its distribution with the former ones. Zoom in at the lowest attenuation region dominant poles seem to appear at more frequencies besides 0.3 GHz (see Fig.6.7). Anyway, three pairs of complex conjugate poles lay on the position of the complex plane corresponding with the main resonant frequency.

Taking uniquely into account dominant poles of the different antennas, a study of the real and imaginary part of those poles has been done. As it is shown in Fig.6.8, the attenuation (real part) decreases as length of the dipole increases providing longer time domain responses. In addition, imaginary part (in absolute value) of those poles responsible of the resonant behavior

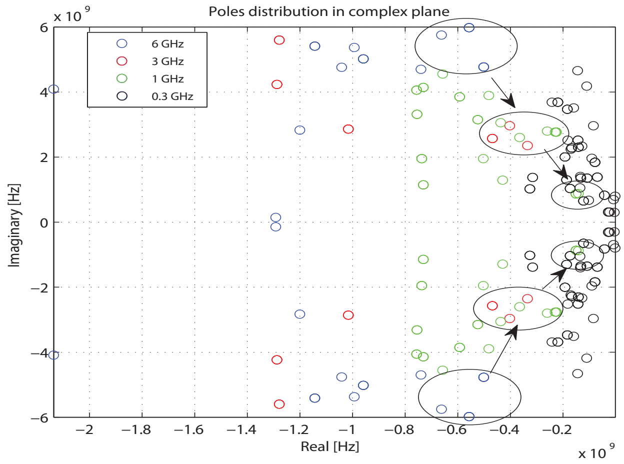

Figure 6.6: Poles distribution in complex frequency plane. Poles which energy holds $\varepsilon_{n,m,k}/\varepsilon_{max} \geq 0.1$ are displayed.

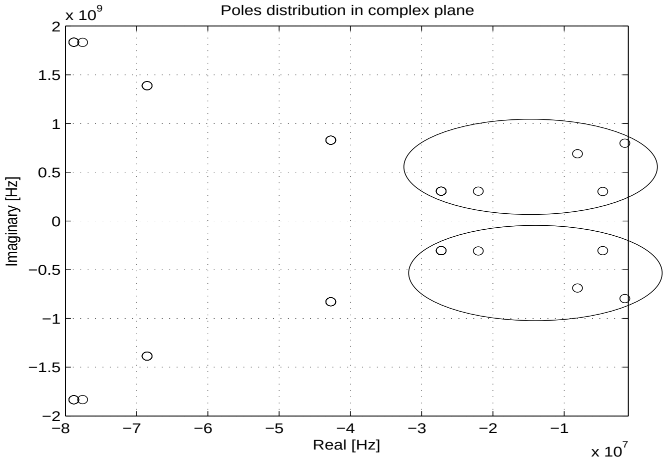

Figure 6.7: Zoom in of poles distribution in complex frequency plane of 0.3 GHz dipole. Poles which energy holds $\varepsilon_{n,m,k}/\varepsilon_{max} \geq 0.1$ are displayed

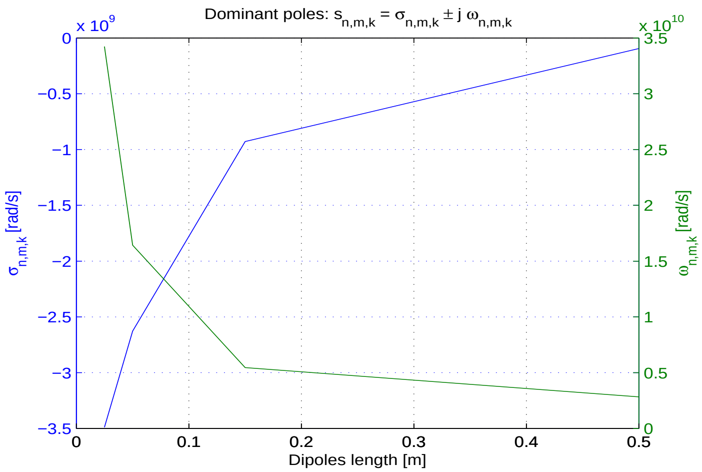

Figure 6.8: Real and imaginary part of dominant poles related with dipole length.

increases decreases as dipole's length increments.

Let us now focus the attention in one specific distribution of poles. Poles distribution in frequency complex plane for the dipole operating around 6 GHz is shown in Fig.6.9. Dominant poles are those with weaker damped coefficients (enclosed within the ellipse). Different colors denote the harmonic in matter of each group of poles. In this case, the dominant poles belong to harmonics $n = 1, m = -1$ and $n = 1, m = -1$ in green and $n = 0, m = 0$ in blue.

It can be interesting to study the contribution of those poles to the final radiated time-signal. In Fig.6.10a contributions of the three dominant poles are illustrated individually. The dashed-green line correspond to the strongest pole. This contribution is evaluated applying radiated time field equation Eq.(3.20) previously discussed. In the figures the time domain axis starts at the time-step holding $\tau/t_h > 0$, in other words when the Heaviside step function is equal to 1. In Fig.6.10b, the contribution of those poles has been added and as it can be observed, it seems that those poles are mainly responsible of the late time response. Of course, poles with stronger attenuation that are not considered here, will account for the very early time. Moreover, a higher order of poles must be used to recover the signal at the very early time since more modes are propagating.

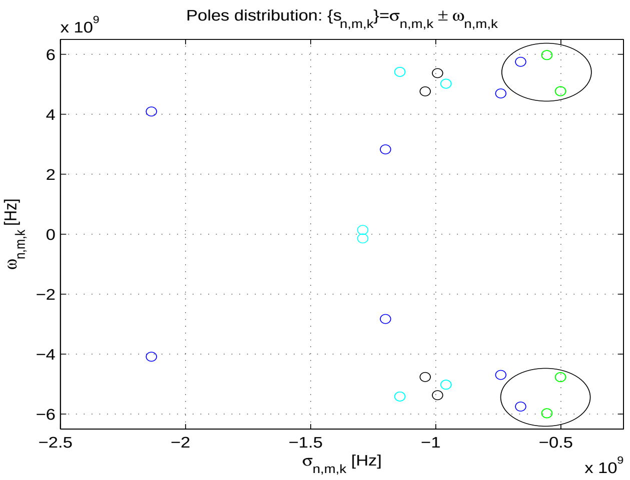

Figure 6.9: Pole distribution of 6 GHz dipole.

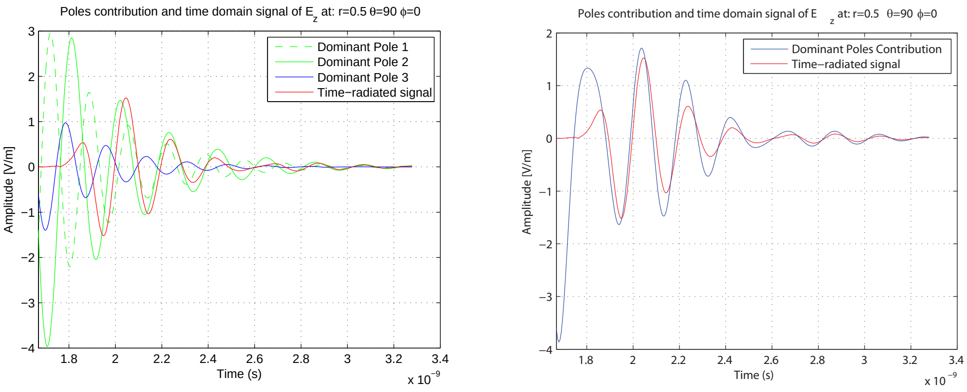

Figure 6.10: Dominant poles contribution to the time-radiated electric field of Z component.

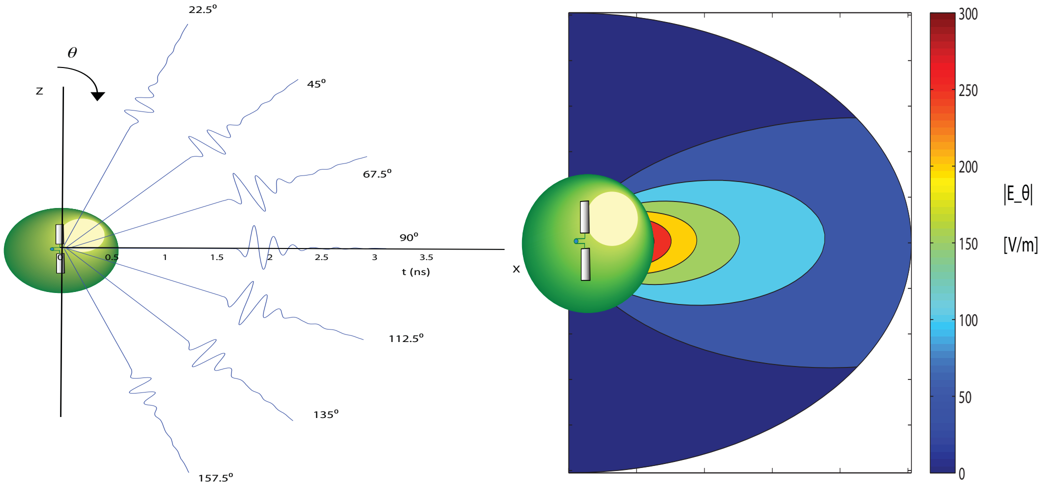

Figure 6.11: a) Spatial-time distribution of the θ component of the radiated field at E-plane. b) Spatial-frequency distribution of the θ component of the radiated field at E-plane. Radius going from $R_{min} = 0.025$ to $R_{min} = 0.1$ m

6.3.2 Radiation patterns

Having discussed the poles distribution in the complex plane, a study of the spatial-time behavior of the electromagnetic field radiated should be investigated. Both domains, time and frequency will be taking into account. Generally speaking, a larger length of the dipole will provide time domain signals longer in time. In other words, as long as the length increases the traveling time of the pulse in the antenna becomes longer and reflections are spreader in time. According to frequency domain, a enlargement of the antenna derives in the arising of extra resonant frequencies. Therefore, the radiation patterns should experienced the apparition of side-lobes.

In Fig.6.11a, a spatial time distribution of the radiated field can be shown for the 6 GHz dipole. As expected, the radiated field along the z axis is zero since the structure is aligned along this axis. Moreover, a symmetry property can be observed at elevation angle variations. In Fig.6.11b, the spatial frequency domain is displayed supporting the afore-mentioned symmetry. Recalling results outlined in [1], Fig.6.12 shows the spatial distribution of θ-component of the electric field at different elevation angles of a dipole excited by a pulse which fits roughly four times along the dipole arm. As pointed out along this work, in this case the dipole holding this characteristic is the one

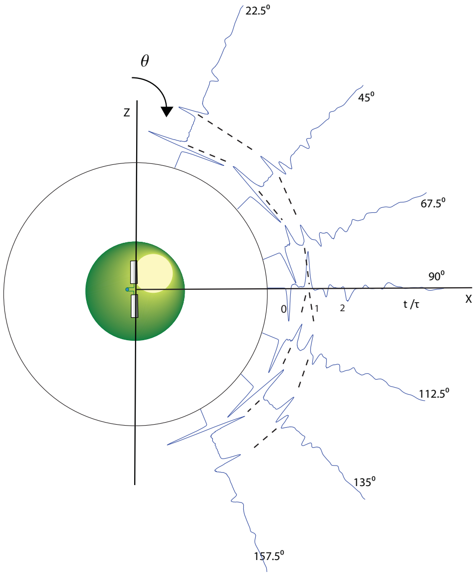

Figure 6.12: Dipole 0.3 GHz: Spatial-time distribution of the θ component of the radiated field at E-plane. $\tau = h/c_0$ being h the arm-length and c_0 the speed of light.

designed to operate at 0.3 GHz. It can appreciated how the reflected waves occurring at the upper and lower terminations approach each other as the elevation angle $\theta \rightarrow 90^{\circ}$. At this spatial point, the reflected waves interfere constructively since the time of arrival of those waves for an observer situated at that point is the same.

In order to provide a better understanding about the relation of the pulse-length/dipole-length ratio and the time radiated fields, similar figures are displayed for the other cases. As it can be observed in Fig.6.11a-Fig.6.13, the separation between the reflected waves and the pulse originated in the drive point of the antenna is directly related with the ratio pulse-length/dipole-length. In those cases where the excited pulse signal is larger compare to the structure, the reflected waves arise instantaneously and reduces the level of the main pulse. Those signals, would look like cosines attenuated and therefore, as mentioned before just a little number of exponentials is needed to characterize its time behavior and specially the late-time. On the other hand

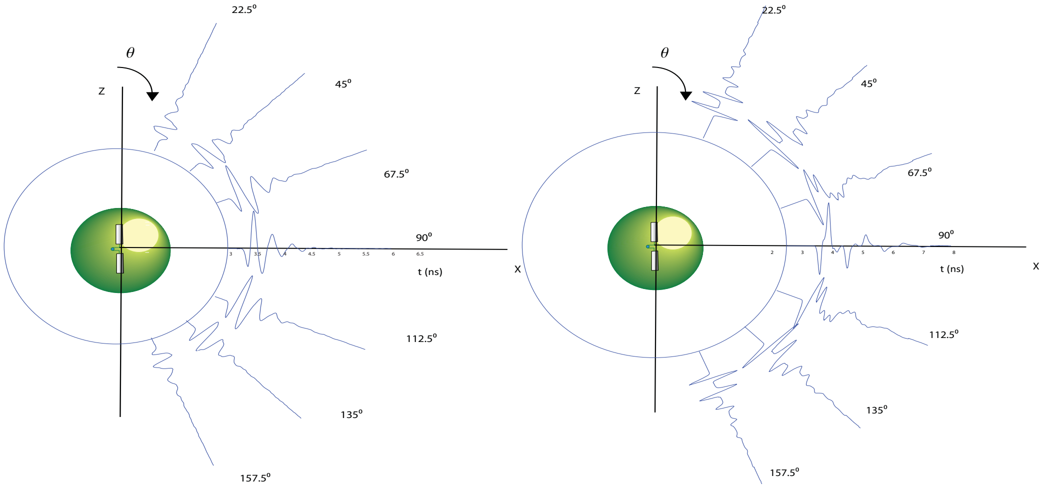

Figure 6.13: a) Dipole 3 GHz and b) 1 GHz: Spatial-time distribution of the θ component of the radiated field at E-plane.

, those dipoles which the pulse-signal is not large compare to its length the time signal becomes more complex and a characterization using exponential functions would require higher expansion orders and a great higher number of exponentials.

It must be noticed that the results displayed for the 6 GHz and 3 GHz dipoles have been acquired using the pole/residue model whereas the results for the 1 and 0.3 GHz dipoles have been done using the SST equation due to the large computation time and different problems derived from the high harmonic expansion and pole orders in Matlab computation. In Fig.6.14 is shown the similarity between the results obtained for the SST and the pole/residue model of the former dipoles. Although having not able to present the same figures for the latter, different versions of the density currents excited on the Huygens sphere are presented in Fig.6.15. Blue line correspond to the currents obtained from CST evaluation, red line corresponds to the time-variant coefficient version and the green one to the pole/residue version. As it can be observed, the expansion order for both cases is chosen correctly since the recovered version of the current perfectly fits the original one. Regarding the pole order K, in both cases a set of 40 poles were used in the pole relocation technique. The recovered version in the 1 GHz dipole case perfectly fits the original one whereas in the case of the 0.3 GHz a ripple is observed indicating

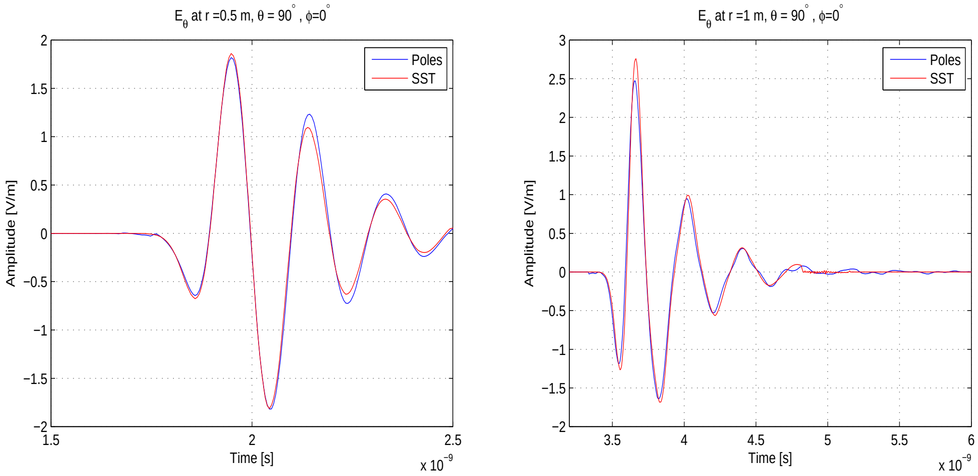

Figure 6.14: (a) Dipole 6 GHz and (b) 3 GHz: Transient behavior of the θ component of the electric field computed by SST equation and the proposed pole/residue model.

that a higher K order would be needed. However, this increase will become the algorithm slower getting to very large computation times.

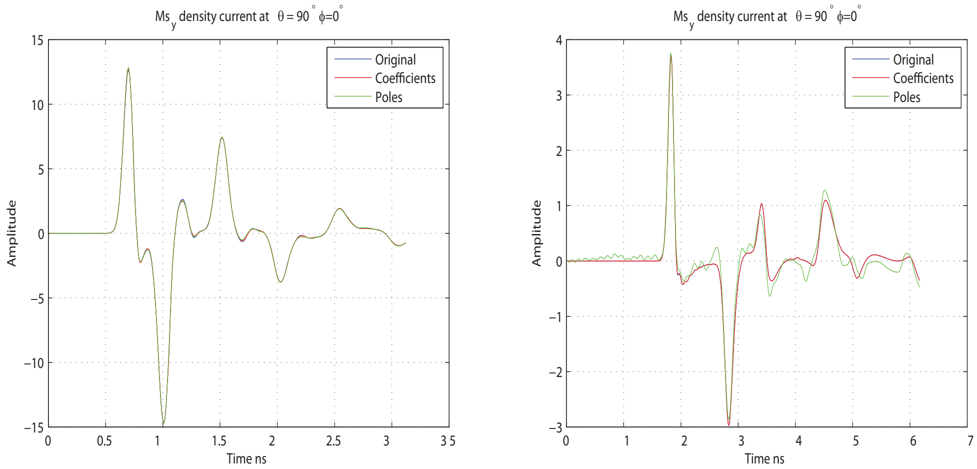

Figure 6.15: (a) Dipole 1 GHz and (b) 0.3 GHz: y-component of the Magnetic density current at $\theta = 90°, \phi = 0°$ computed by CST software, time harmonic expansion and pole/residue model.

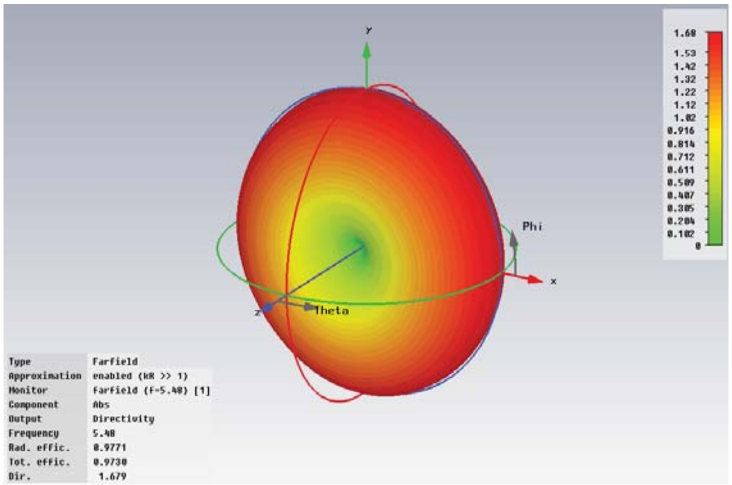

Type	Farfield
Approximation	enabled (kR >> 1)
Monitor	farfield (f=5.48) [1]
Component	Abs
Output	Directivity
Frequency	5.48
Rad. effic.	0.9771
Tot. effic.	0.9730
Dir.	1.679

Figure 6.16: Three-dimensional pattern of $\lambda/2$ dipole at operation frequency (f= 5.5GHz). Directivity provided in linear units.

6.3.3 Radiation patterns: Frequency domain

Transient radiation have been thoroughly studied so far. However, talking about antennas a frequency domain point of view can not be skipped. To this end, radiation in frequency domain and radiation patterns should be shown. Although dipole antenna radiation patterns are well-known would worth bring them up to this report. In that way, a relation between the time domain results already obtained and frequency radiation patterns can be derived. As discussed half-wave dipole antenna because of its simple geometry and radiation resistance (near the 50-ohm and 75-ohm characteristic impedance of transmission lines) is one of the most commonly used antennas. Then, let us focus now on the half-wave dipole operating at 6 GHz. As expected, the radiation pattern obtained in 3-D is a donut-like shape along the XY-plane (see Fig.6.16). Furthermore, the maximum directivity is practically identical to the value obtained theoritically $D_0 \simeq 1.64$.

In Fig.6.17 is also shown the two-dimensional radiation pattern at XZ cutting plane ($\phi = 0°$). In that way it can be readily noticed that the revolution of the latter diagram turns out in the three-dimensional radiation pattern in Fig.6.16. Therefore, the radiated field in frequency domain should be maximum at the operation frequency and at the direction given by the elevation angle $\theta = 90°$. Indeed, this can be observed in Fig.6.18 where the θ-component absolute value of the electric field is displayed at several elevation

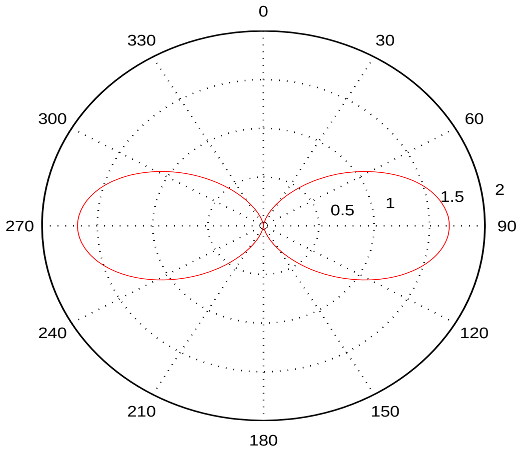

Figure 6.17: Two-dimensional pattern of $\lambda/2$ dipole at operation frequency (f= 5.5GHz). Directivity provided in linear units.

angles. The antenna response peaks at roughly the operating frequency where the length of the dipole is about $\lambda/2$. Furthermore, the magnitude of the electric field becomes maximum at the direction given by an elevation angle of $\theta = 90°$.

Earlier in this chapter, it has been discussed the consequences of increasing the dipole-length in a time-domain sense. Let us now switch to the frequency domain. Thinking about the dipole antenna, it can be readily inferred that as the length increases newer resonant frequencies arise since additional λ will hold $l = 3\lambda_2/2, 5\lambda_3/2...$ besides $l = \lambda/2$. Therefore, since more frequencies are involved, regarding the pole distribution in the complex plane, more poles will be needed to characterize the radiated field. Let us focus on the largest dipole simulated operating at 0.3 GHz. In Fig.6.19, it can be observed the radiation patterns for three frequencies holding different relation $l \sim \lambda$. Even though do not exactly resemble to the radiation patterns expected for dipoles obeying $l = 3\lambda/2, 5\lambda/2$ it does for those ones holding $l = 1.4\lambda/2, 2.4\lambda$. Then, besides the requirement of using a higher pole order because new frequencies have shown up, one might think that different set of poles belonging to different spherical harmonics will account now for those radiation patterns. In order to picture up this result, let us now focus in the dipole antenna previously named as 1 GHz dipole. Recalling the matching region for this antenna in Fig.6.5 was found to be about 0.9 GHz and 2.8

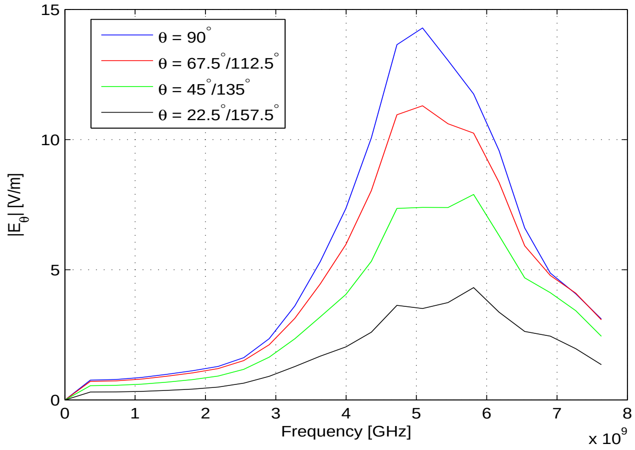

Figure 6.18: Radiated field in frequency domain at different elevation spatial points.$|E_\theta|$ at $\boldsymbol{r} \equiv \{0.5, \theta, 0°\}$

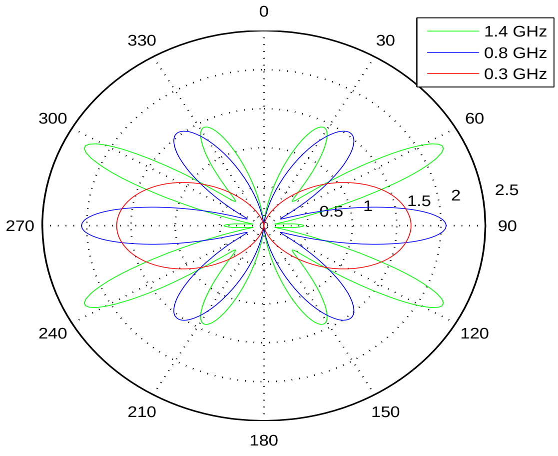

Figure 6.19: Two-dimensional patterns of $\lambda/2$ dipole at operation frequency (f= 0.3GHz). Directivity provided in linear units.

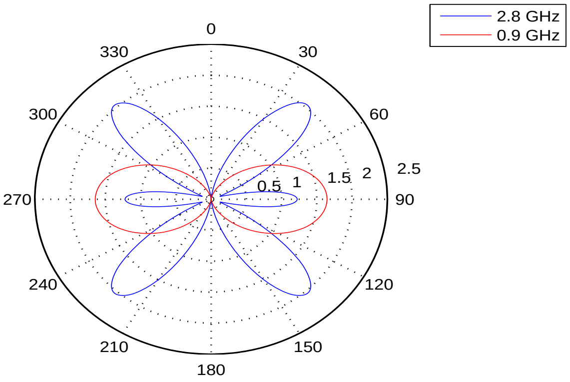

Figure 6.20: Two-dimensional patterns of "1GHz dipole". Directivity provided in linear units.

GHz. Two-dimensional radiation patterns at both frequencies are presented in Fig.6.20. In this case, the operating frequencies as well as the radiation patterns resemble to dipoles $l = 0.5\lambda$ and $l = 1.5\lambda$ respectively.

Let us gaze the poles distribution in the complex plane for this antenna case. As it can be observed, two group of dominant poles are highlighted accounting roughly for the resonant frequencies 0.9 GHz (blue ellipse) and 2.8 GHz (black ellipse) respectively. Investigating the origin of this poles has been found that those ones with imaginary part close to 0.9 GHz belong to the spherical harmonic with orders $n = 1, m = \pm 1$. On the other hand, those poles responsible for the 2.8 GHz resonant frequency response belong to the spherical harmonic holding n and m orders such as $n = 3, m = \pm 1$. In order to provide a better understanding of this phenomena let us take a look to the spherical harmonics holding this orders. As shown in Fig.6.22b, seems fair to relate the distribution of this spherical harmonics to the radiation patterns of each frequency. In particular, as observed in Fig.6.20 the main lobe in blue line (2.8 GHz) is about 45 degrees from Z axis. Looking now the absolute value of harmonic $n = 3, m = \pm 1$ the maximum is achieved about $\theta = 58°$ which is near to the angle describing the direction of maximum radiation.

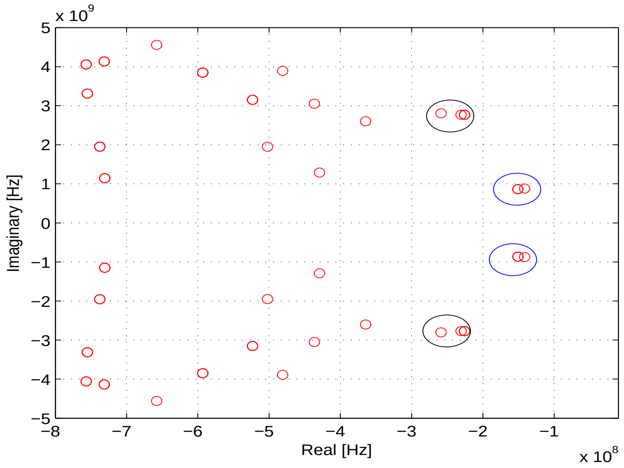

Figure 6.21: Poles distribution in complex plane for "1GHz dipole". Poles which energy holds $\varepsilon_{n,m,k}/\varepsilon_{max} \geq 0.1$ are displayed.

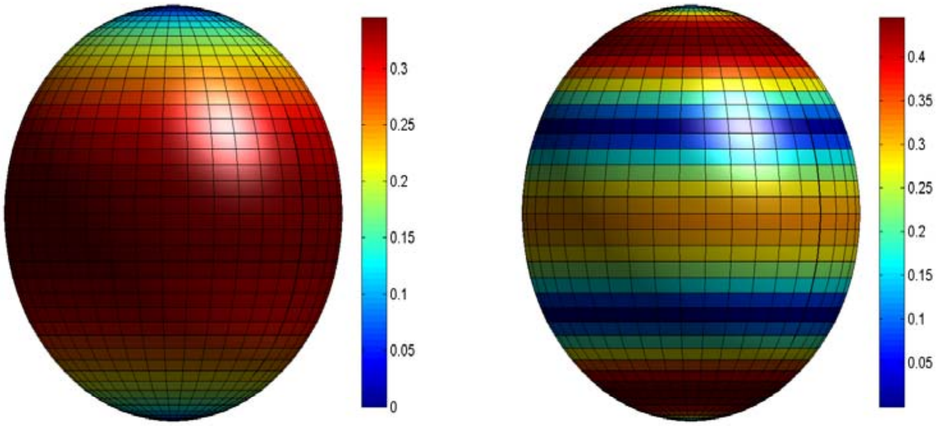

(a) $n = 1, m = \pm 1$

(b) $n = 3, m = \pm 1$

Figure 6.22: Absolute value of Spherical harmonics with orders : (a) $n = 1, m = \pm 1$ and (b) $n = 3, m = \pm 1$

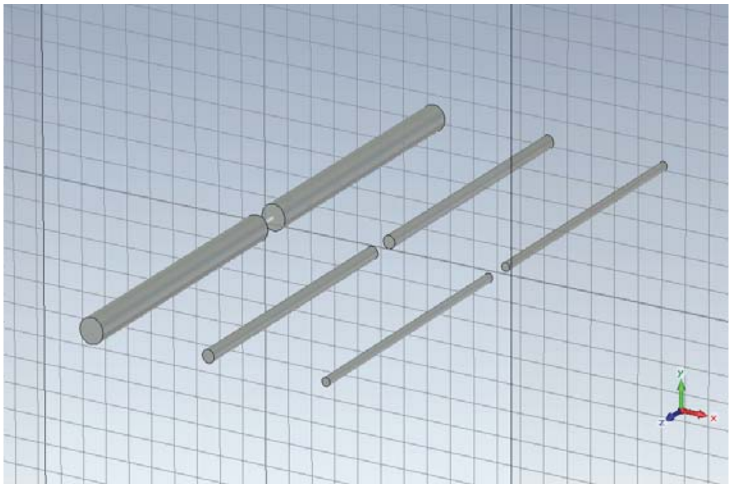

Figure 6.23: CST model of different dipoles holding different l/d ratio.

6.4 Radius wire parameter

A glance to Fig.6.2 reveal us how by increasing the radius of the wire of a dipole antenna the impedance variation becomes less sensitive as a function of frequency. Then by decreasing the l/d ratio (increasing diameter of the wire) a enlargement of the frequency bandwidth should be experienced improving the broadband characteristics of the antenna. Therefore, for a given length dipole different thicknesses of the wire has been studied. The lower the l/d ratio the thicker is the wire of the dipole.

Dipole-length $l = \lambda/2$ (m)	Operating Frequency (GHz)	l/d ratio
0.025	6	75
0.025	6	50
0.025	6	25

Table 6.3: Dipole physical parameters.

6.4.1 Poles Distribution in frequency complex plane

Following the recommendations previously discussed, dipoles with different thicknesses have been simulated. As it can be shown in Fig.6.24, the bandwidth enlargement expected is not clear. In addition, the pole distribution

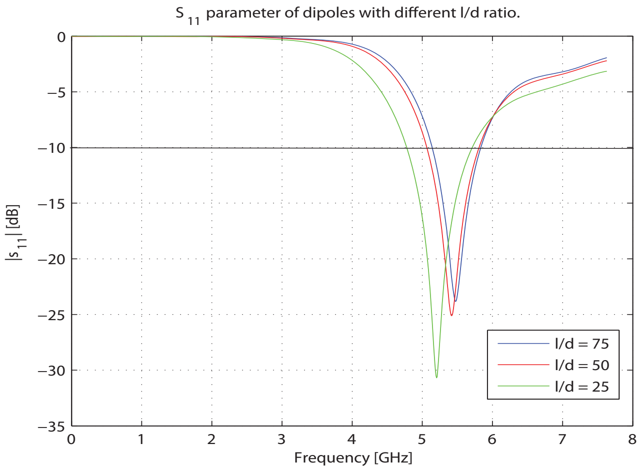

Figure 6.24: S_{11} parameter of half-wave dipoles with different wire thickness.

in the complex plane do not provide information enough to make an statement about this parameter. Indeed, the dominant poles lay on the region where the antennas resonate but the behavior of the poles is unclear. In other words, it can be observed how the poles corresponding with the thicker dipole ($l/d = 25$) move to the left in the complex plane but the ones corresponding to ($l/d = 50$) are more right positioned than the poles corresponding to the thinner dipole.

Let us now focus on the time radiation signals. From the previous results might be expected that the time radiated field would look similar. Indeed, this phenomena can be checked looking Fig.6.26 where a similar frequency behavior is observed. However, signals corresponding to the thicker dipole have a higher level in the early time than the rest. However, at the late time the level is lower and that might be explained as the higher value of the attenuation of the dominant poles.

6.5 Conclusions

In this chapter a thorough study of transient radiation and poles distribution in complex plane for a dipole antenna has been performed. As a result, some conclusions have been stated. In particular, a relationship between the physical characteristics of the antenna in matter and its complex resonant processes has been derived. Having studied the location on the complex

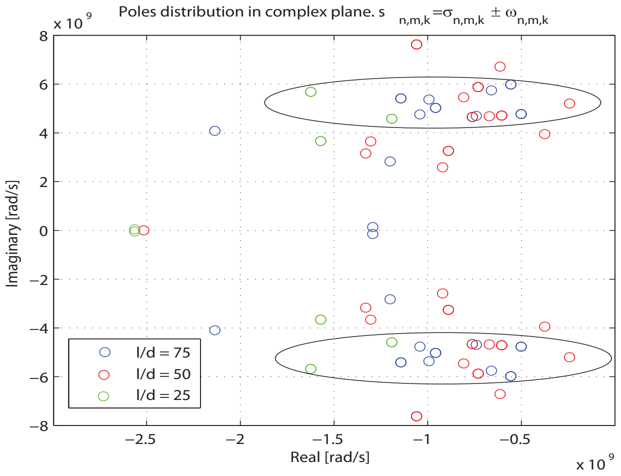

Figure 6.25: Poles distribution in complex frequency plane. Poles which energy holds $\varepsilon_{n,m,k}/\varepsilon_{max} \geq 0.1$ are displayed

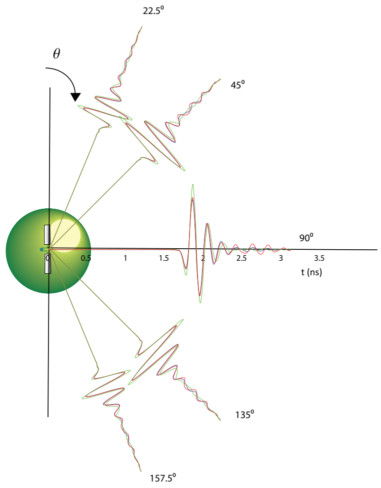

Figure 6.26: Dipole 0.3 GHz: Spatial-time distribution of the θ component of the radiated field at E-plane. Dipoles with different wire thickness are shown: $l/d = 75$ (blue), $l/d = 50$ (red), $l/d = 25$ (green)

frequency plane of the dominant poles mainly responsible for the radiated response, a travel from higher to lower attenuations and from higher to lower resonant frequencies when the length of the antenna increases has been observed. Furthermore, a higher pole relocation order K in the algorithm performed is required for antennas which length is comparable to the excitation signal length meaning that longer radiated signals in time and new frequencies are excited.

Chapter 7

Bow-tie Antenna

In this chapter as it has been done before for dipole antenna, the transient radiation and poles distribution in the complex plane of bow-tie antenna should be thoroughly studied. Bow-tie antennas are basically geometrical approximations of solid biconical antennas. This approach tries to retain the electrical features of the latter but achieving practical geometry and size. At the end, a bow-tie antenna is a flat version of the dipole. By increasing the conductor surface the transition between the antenna and the air is smother resulting in wider band response.

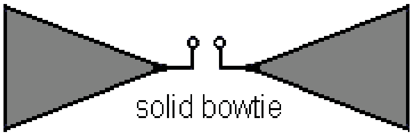

Figure 7.1: Bow-Tie Antenna geometry

7.1 Geometry

According to Fig.7.2 different bow-tie antennas can be designed to operate at a certain frequency. In this work, the length of the antenna has been chosen in those points where the reactance is equal to zero (resonate condition) and the resistance has a reasonable value. In Fig.7.2

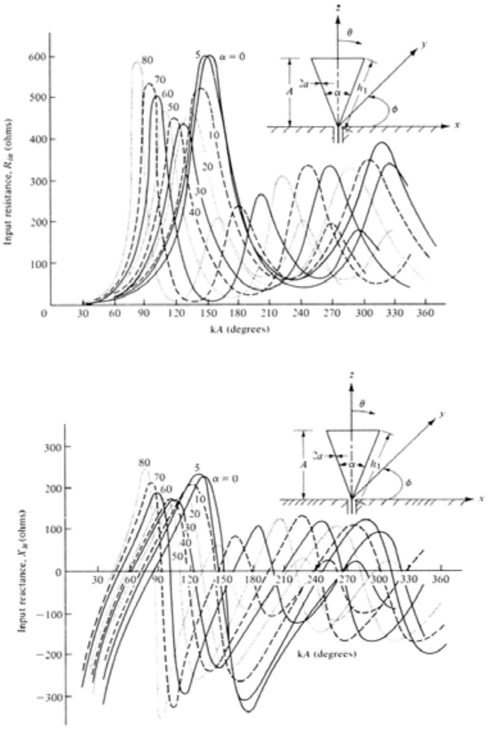

Figure 7.2: Computed impedance of wire bow-tie (or wire unipole) as a function of the length for various included angles.[27]

Then, there are two parameters to take into consideration: flair angle and length of the antenna.

7.2 Gaussian Pulse selected

In this study case the Gaussian pulse excitation signal has been selected to fulfill the frequency range of study from 300 MHz to 6 GHz. As it has been done previously the minimum frequency will be set at 0 GHz in order to get a non-derivative Gaussian pulse in CST and the maximum frequency will be set to be 6 GHz.

7.3 Flair angle study

Regarding Fig.7.2 it can be noticed that flair angle and length of the arm are related in terms of reactance. In other words, for a fixed angle there are different lengths where the antenna will resonate and not necessary equivalents for another flair angle. Therefore, the following study procedure has been set. A operating frequency within the range of study has been chosen, $f = 3\text{GHz} \rightarrow \lambda = 0.1\text{m}$. Then, according to Fig.7.2, the first length where resonance occurs has been selected for several flair angles. As it can be seen in Tab.(7.1) the length of the antennas is not equal but similar. The resulting structures are supposed to radiate at 3 GHz in a certain bandwidth. Although having different lengths a study of the poles distribution in the complex plane and transient radiation characteristics should be done.

λ (m)	Length $kA = \frac{2\pi}{\lambda}A(°)$	Length A (m)	Flair angle (°)	Input resistance (Ω)
0.1	65	0.0181	20	50
0.1	60	0.0166	40	50
0.1	50	0.0138	60	50
0.1	50	0.0138	70	50
0.1	45	0.0125	80	50

Table 7.1: Bow-tie antenna physical parameters.

7.3.1 Poles Distribution in frequency complex plane

As it can be observed in Fig.7.3 resonances occur at roughly 3 GHz. The reason of the shifting might be that the length is not exactly the one taken from the graph as well as inaccuracies in the full wave procedure solver adopted. It can be also noticed how the operational bandwidth increases as the flair angle does. This result might be expected since the smaller the flair angle the closer is the bow-tie antenna to a dipole antenna adopting its narrow-band characteristics. The more surface of conductor material the smoother transition between the antenna and the propagating medium. Once having observed the matching impedance behavior of the antennas simulated, let us pay attention to the pole distribution obtained by applying the pole/residue model used along all this thesis work. In Fig.7.4 it can be appreciated how dominant poles lay on the region corresponding with the resonant region shown by Fig.7.3. Resonance for the 40° bow tie antenna

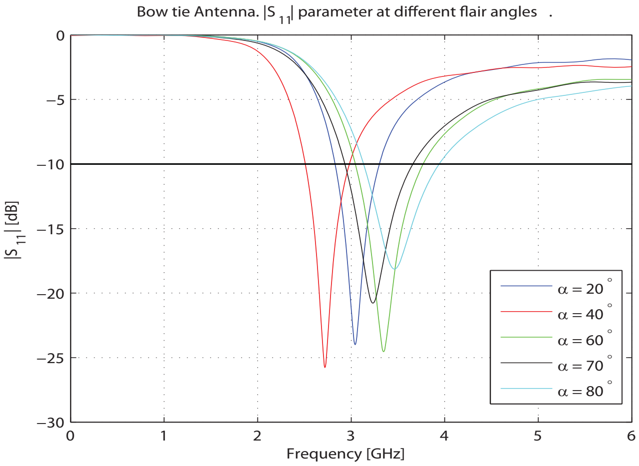

Figure 7.3: S_{11} parameter of bow-tie antennas with different flair angle.

occurs slightly at lower frequency and that can be observed in the poles distribution as well. Regarding the differences in the poles distribution for the different flair angles a interesting result can be noticed and its physically meaning must be investigated. Paying attention to dashed line drawn in front of the group of poles describing 20° behavior (blue circles) seems that as long as the flair angle increases those poles tend to move outwards in a sort of radially way. There are poles intercalated such as the corresponding to the 70° bow-tie.

In Fig.7.5 the mean value of the real and imaginary part of the poles displayed in Fig.7.4 are evaluated in an attempt to relate them to the flair angle.As mentioned before this behavior,though unclear, must be investigated in order to find out either is related to a physical meaning meaning or just has to do with mathematical reasons.

To this end, a research of the time-radiation patterns must be carried out. Since every antenna has been simulated assuming the same orientation and local coordinate system reference (see Fig.7.6) the X-component of the electric field would be selected as the co-polarized component.

In that way, knowing the bow-tie radiation characteristics the direction of maximum radiation in the adopted system reference must be $\theta = 90°$ and $\phi = 90°$. From Fig.7.7 it can not be extract enough information for understanding the behavior of the poles along the complex plane. On the other hand, paying attention to the 40°-curve it can be noticed that the

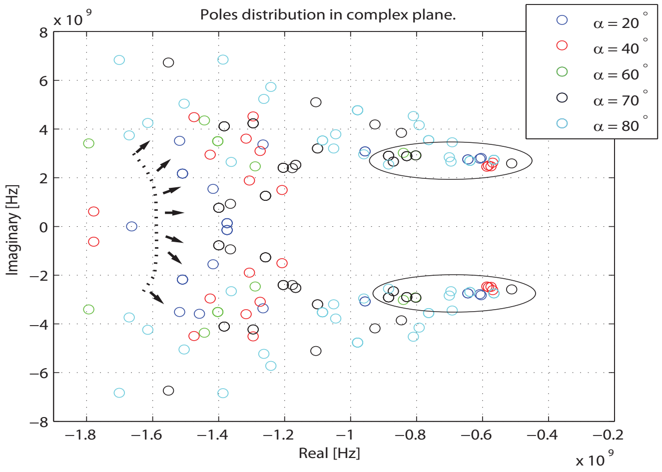

Figure 7.4: Poles distribution in complex frequency plane. Poles which energy holds $\varepsilon_{n,m,k}/\varepsilon_{max} \geq 0.1$ are displayed

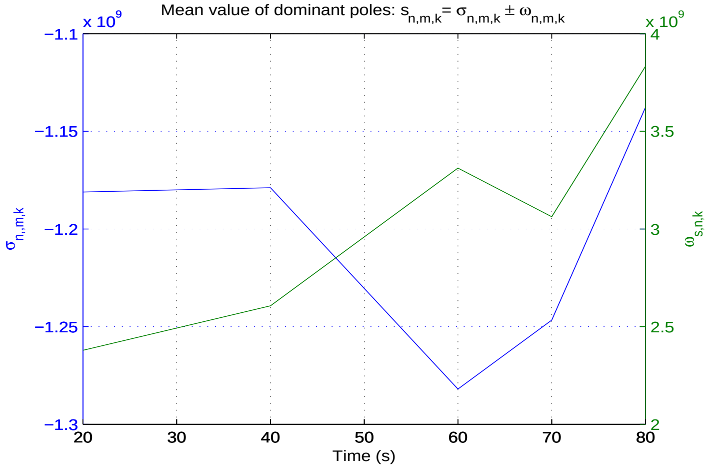

Figure 7.5: Mean values of real and imaginary part for the pole distribution for bow-tie antennas with different flair angle.

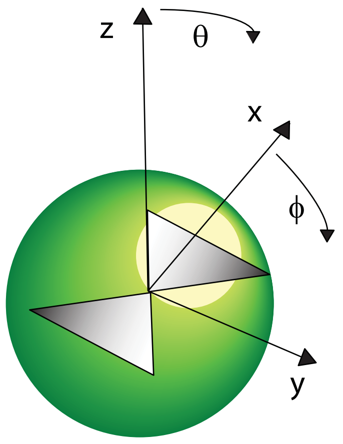

Figure 7.6: Bow-tie antenna enclosed by a spherical Huygens surface. Reference system selected.

radiative signal is slightly longer in time and the reason can be found in Fig.7.3 and Fig.7.4. In one hand, the S_{11} curve reveals resonance at lower frequency than the rest of the antennas yielding time signals wider. Besides, a group of dominant poles with weak attenuation is found providing as well contribution to the late time signal.

7.3.2 Radiation patterns: Time domain

In order to provide a better understanding of the time domain distribution of the radiated field, let us focus in the spatial distribution along the XY-plane. As expected, the radiation along the broad side of the antenna (X axis) is negligible since is close to zero. In Fig.7.8 the spatial distribution in time- and frequency-domain for 70° flair bow-tie antenna is shown. The radiation is maximum at the end fire of the antenna and symmetry along Y-axis is held. In addition, a spatial frequency domain distribution is displayed denoting the usual radial attenuation behavior.

In order to figure out the existence of any relationship between the flair angle of a bow-tie antenna and its radiated field response, it could interested repeat the graph in Fig.7.8a for each antenna case. A priori, one might think that as long as the flair angle increases more energy will concentrate to the direction of maximum radiation. This can be slightly appreciate for the 70°

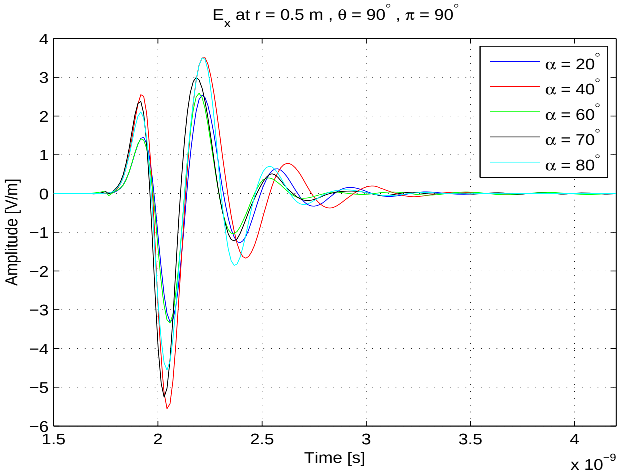

Figure 7.7: E_x at direction of maximum radiation: $\theta = 90°, \phi = 90°$ for several bow-tie antennas with different flair angles.

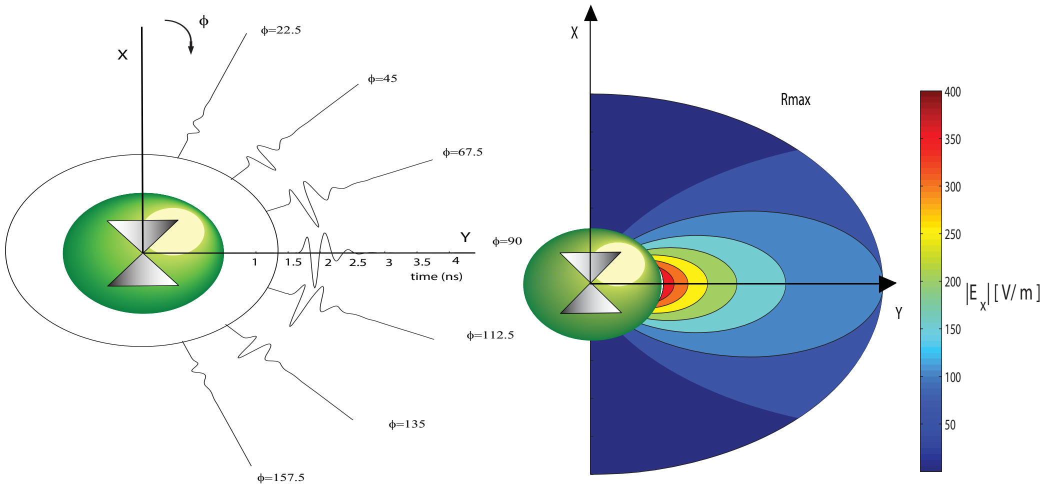

(a) Time domain (b) Frequency domain

Figure 7.8: Radiated field spatial distribution of E_x component of bow-tie antenna with a flair angle of 70°

and 80° bow-tie antennas in comparison with the rest. On the other hand, 40° antenna breaks this tendency presenting radiated field responses larger that 60° bow-tie antenna for instance. Therefore, the impact of the flair-angle in the transient radiation is not clear yet as well as the pole distribution in complex frequency plane.

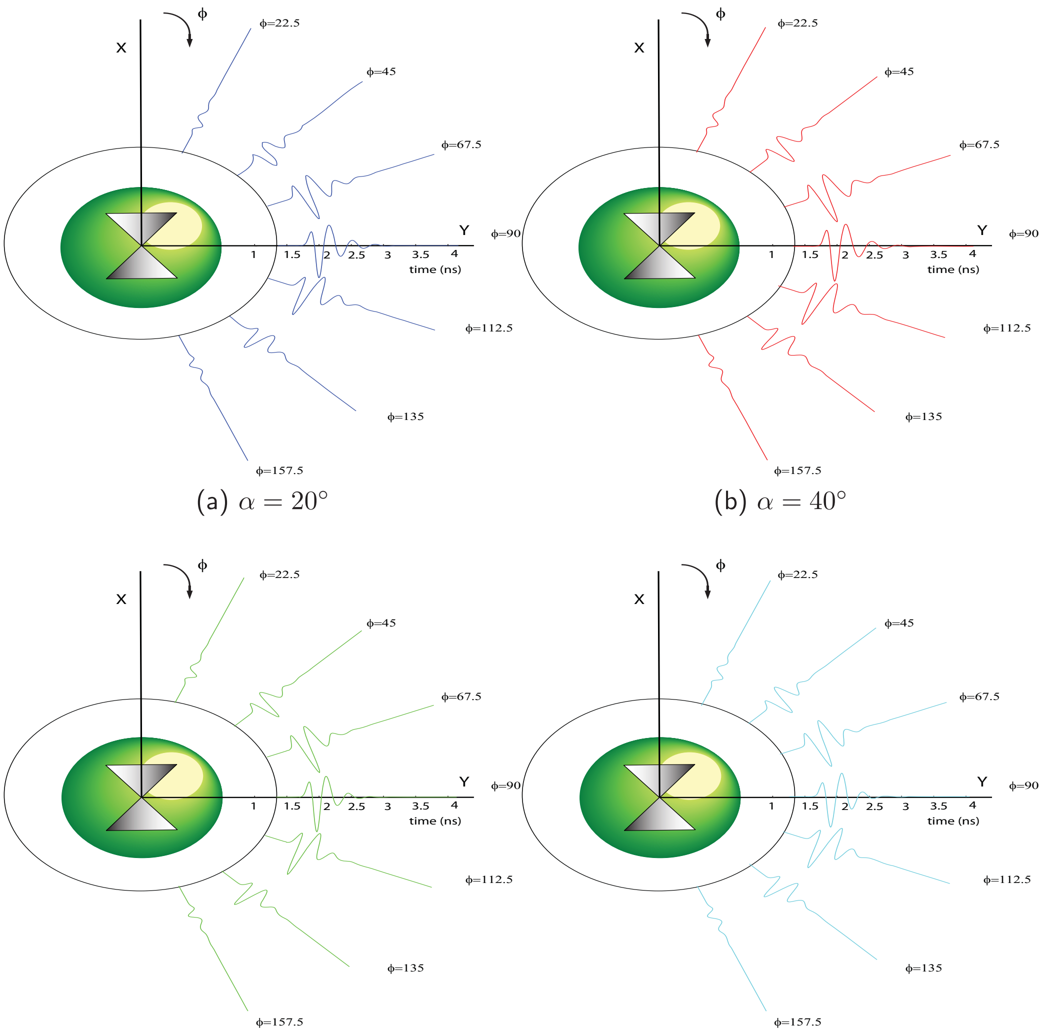

(a) $\alpha = 20°$ (b) $\alpha = 40°$

(c) $\alpha = 60°$ (d) $\alpha = 80°$

Figure 7.9: Radiated field spatial distribution of E_x component for different bow-tie antennas

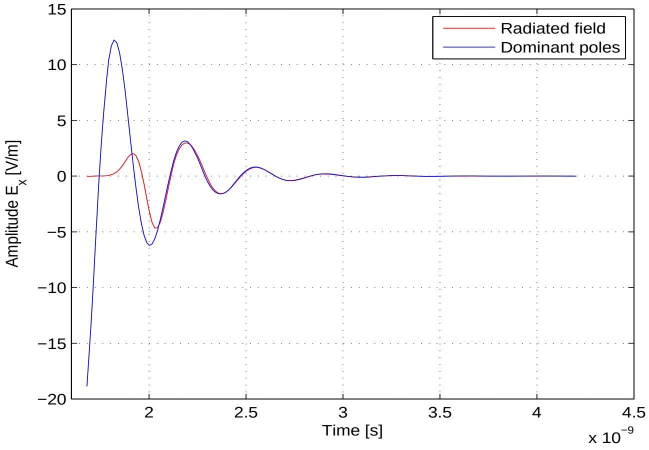

Figure 7.10: 20° flair angle Bor-tie antenna: E_x at direction of maximum radiation: $\theta = 90°, \phi = 90°$ and contribution provided by the dominant poles.

In order to gain a better understanding to the phenomena described, let us now focus in one specific case from the ones already analyzed. In particular, 20° flair angle bow-tie antenna poles distribution will be thoroughly studied. By focusing uniquely in the group of dominant poles, it has been observed how they are totally responsible for the late time response of the antenna (see Fig.7.10). Of course, since more modes are propagating at the earlier time more poles are needed to reconstruct the radiated signal in that region. In addition, the poles responsible for the early-time response are those owning stronger damping coefficients. In fact, one might think that the early-time response belongs to the excitation signal more than the antenna response itself. Consequently, the behavior of the poles accounting for the early time in Fig.7.4, may has to do more with the excitation signal than the antenna response itself. As observed in (see Fig.7.10), with a few of pairs of complex poles (dominant poles) the late time response is perfectly characterized and those dominant poles lay on practically the same region for every antenna case.

7.3.3 Radiation patterns: Frequency domain

In this section, attention will be focused on the frequency domain behavior of the bow-tie antenna. As known, the radiation patterns resemble a donut-

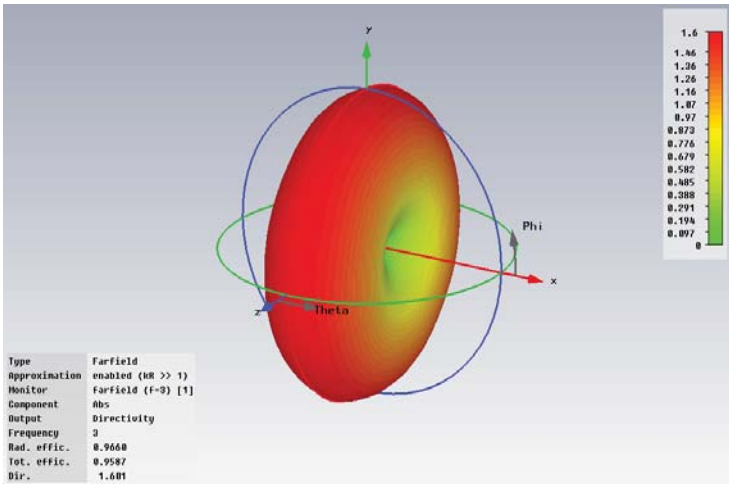

```
Type            Farfield
Approximation   enabled (kR >> 1)
Monitor         farfield (f=3) [1]
Component       Abs
Output          Directivity
Frequency       3
Rad. effic.     0.9660
Tot. effic.     0.9587
Dir.             1.601
```

Figure 7.11: Three-dimensional radiation pattern of a "20°" flair angle Bow-tie antenna. Directivity in linear units.

like shape along the H-plane, in our case corresponding with the YZ-plane, and has deep nulls along the bow-tie axis. This radiation characteristics can be checked by seeing Fig.7.11. In this case, the variations in the physical parameter of the antenna do not provide any meaningful differences in the far field radiation patterns.

Nevertheless, in Fig.7.12 it is shown the spatial distribution in frequency domain for different antennas. As seen, all the cases show the typical $1/r$ spatial decay with global maximum along the end-fire direction $\phi = 90°$. Only it is worth to mention that the differences between the magnitudes are due to the different R_h adopted for each antenna case.

7.4 Antenna-length study

Proceeding as done in the previous section by varying a physical parameter of the bow-tie antenna a relation between this variation and the location of the poles in the complex plane should be investigated. Now, the flair angle will be fixed and by seeking where resonance is achieved the arm length will be set then. In that way, looking back at Fig.7.2 and choosing a flair angle to be $\alpha = 80°$ three antennas with different length have been simulated as shown in Tab.(7.2)

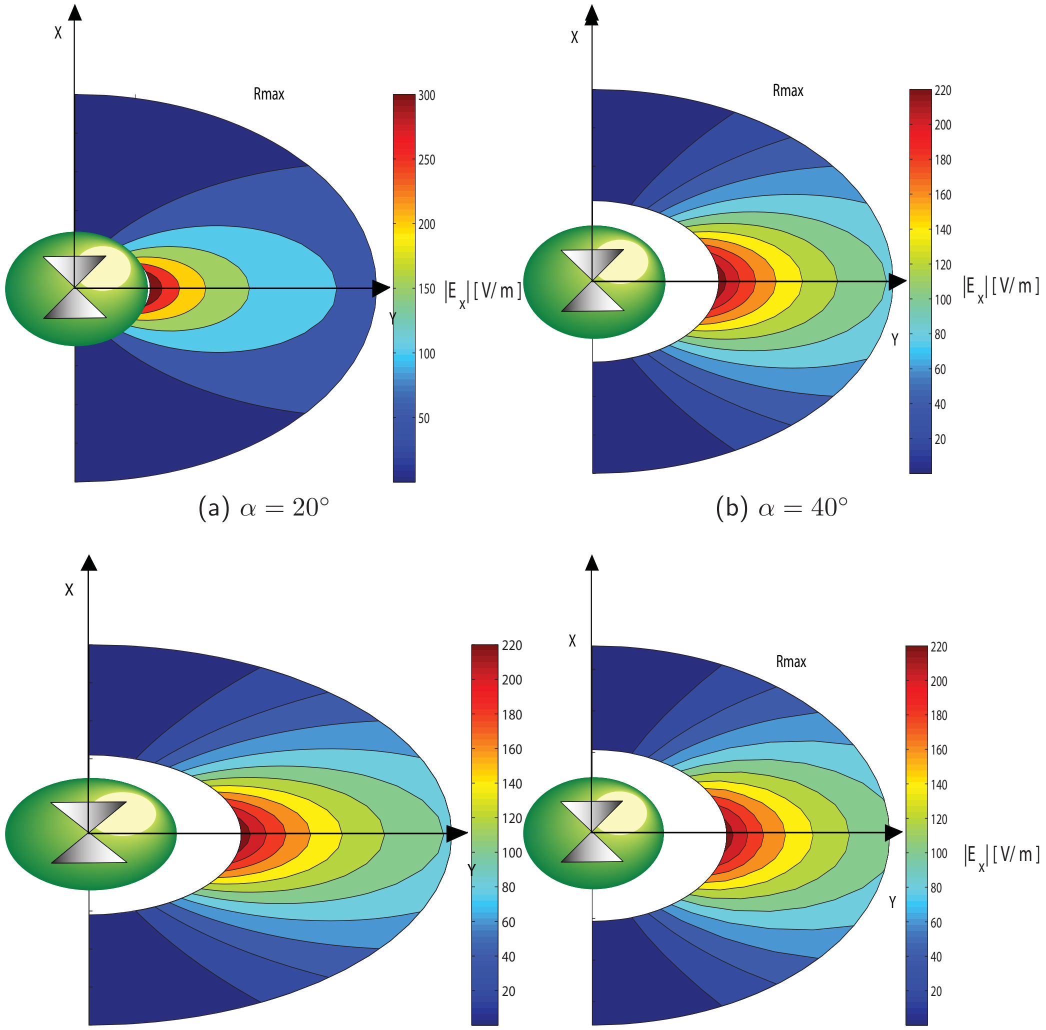

(a) $\alpha = 20°$

(b) $\alpha = 40°$

(c) $\alpha = 60°$

(d) $\alpha = 80°$

Figure 7.12: Radiated field spatial distribution for $R_h \leq r \leq 0.01m$ in frequency domain of E_x component for different bow-tie antennas.

$l = \lambda$ (m)	Length $kA = \frac{2\pi}{\lambda}A(^\circ)$	Length A (m)	Flair angle (°)	Input resitance (Ω)
0.1	45	0.0125	80	50
0.1	130	0.0361	80	50
0.1	155	0.0431	80	200

Table 7.2: Bow-tie antenna physical parameters.

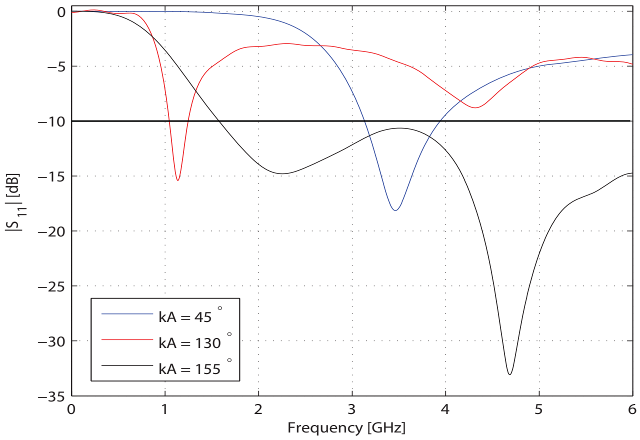

Figure 7.13: S_{11} parameter of bow-tie antennas with different length.

7.4.1 Poles Distribution in frequency complex plane

Before proceeding with the poles distribution analysis, let us first investigate the matching behavior of the antennas which parameters are outlined in Tab.(7.2). In that way, in Fig.7.13 it can be observed the $|S_{11}|$ parameter. Several comments must be done. As long at the length increases, more λ are able to hold any electrical length value where the reactance is zero.

As it can be seen, the largest antenna shows a pretty good matching along the frequency range. On the other hand, the antenna which its length is 130 electrical degrees, just shifted the first resonant frequency to a lower value. Let us now focus the attention to the pole distribution and the transient responses of these antennas. As shown in Fig.7.14, poles which energy holds that $\varepsilon_{n,m,k}/\varepsilon_{max} \geq 0.1$ are displayed. It seems that as long as the length increases those poles move inwards (to lower real and imaginary parts) the complex plane. According to the behavior of S_{11} parameter observed in Fig.7.13 this make sense for the $kA = 130^\circ$ antenna since it resonates at

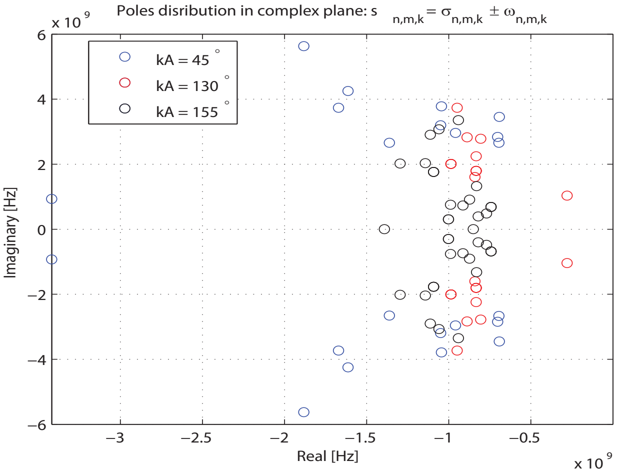

Figure 7.14: Poles distribution in complex frequency plane. Poles which energy holds $\varepsilon_{n,m,k}/\varepsilon_{max} \geq 0.1$ are displayed

roughly 1 GHz. It can be noticed a pair of dominant poles accounting for that frequency. However, for the antenna holding $kA = 155°$ which presented a strong resonance at 4.8 GHz, not any group of poles at that frequency are found. It must be noticed that in this case the antenna is not behaving in a typical resonant way since it has wideband performance. In addition, the traveling time of the excitation signal along the structure has increased and consequently the radiated signals are spread in time needing higher number of poles in the pole/residue representation. Indeed, poles with smaller damping coefficients will be needed to characterize longer signals in the late time.

In order to provide a better understanding about this discussion a look to the transient radiation can not be skipped. In Fig.7.15, the E_x component at the direction of maximum radiation is shown for each antenna considered in this section. It can be readily noticed how as increasing the length the reflected waves observed in the signals become smaller. In particular, while the shorter bow-tie provides a signal close to a cosine and then by a few exponentials at the operating frequency the late-time response can be perfectly reconstructed, the other two present more complex responses. In addition, the reason of the larger value in the first peak for the larger antennas is that the reflected wave in the short case antenna arise earlier in time ”eating” part of the main pulse.

By looking at Fig.7.16, an idea about the spatial distribution in time

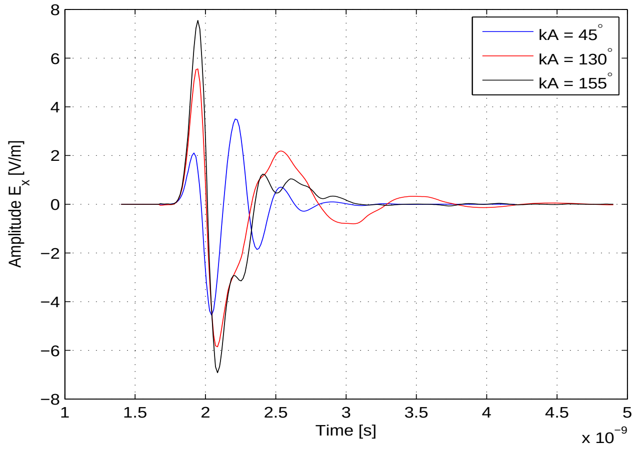

Figure 7.15: E_x at direction of maximum radiation for bow-tie antennas with different electrical length.

domain is given. Again, the direction of maximum radiation is at $\theta = 90°$, $\phi = 90°$ and as long as we move to the bow-tie axis the radiated field decreases till being negligible.

So far, it has been found meaningful relation between the dominant poles and the resonant frequency for the antennas with electrical length $kA = 45°$ and $kA = 130°$. On other hand, it has been found difficult to find out a physical explanation for the third antenna in matter.

7.5 Conclusions

In this chapter a bow-tie antenna has been analyzed. Although, a clear relationship between the physical parameters studied and the pole distribution in complex plane has not been achieved, it seems that in those antennas with a resonant behavior group of poles appeared at the expected resonance frequencies taking care mainly for the late-time response.

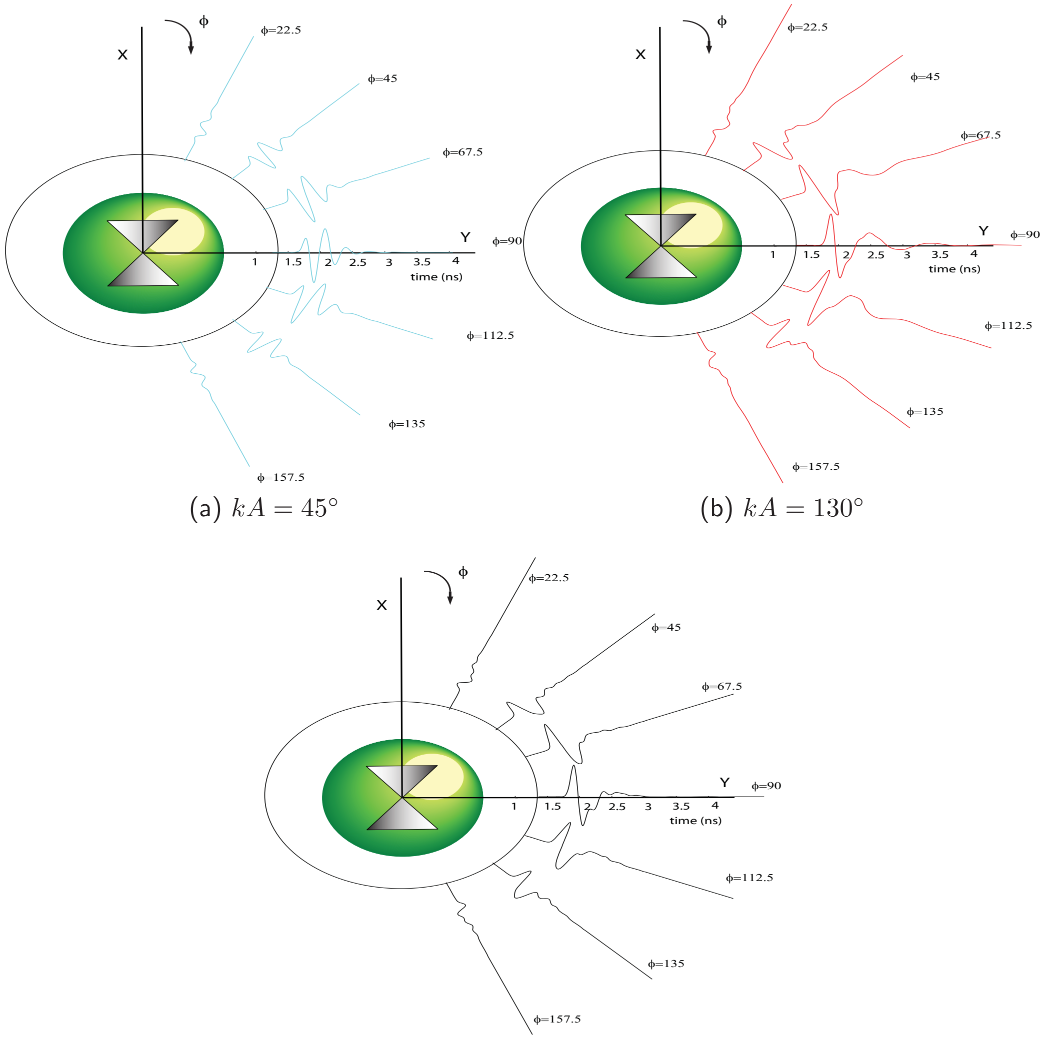

(a) $kA = 45°$

(b) $kA = 130°$

(c) $kA = 155°$

Figure 7.16: Radiated field spatial distribution of E_x component for different bow-tie antennas

Chapter 8

Loop Antenna

The aim of this chapter is to provide a thorough transient study and a physical reason for the poles location of another simple and very versatile structure such the loop antenna. Regarding bibliography about this sort of antenna and it characteristics, geometry and behavior, an electrically large antenna configuration has been chosen. This sort of antennas are used in UHF applications from 300 MHz to 3GHz which it is within the frequency range under study in this work. Furthermore, as discussed in 2.2.3 the bend of the loop antenna originates radiation but in a different way as a discontinuity of a dipole does. For this reason, it would be interesting to attempt to characterize such antenna as it has been done with the dipole antenna.

8.1 Geometry

The circular loop antenna is nothing more that a wire bend forming a circle and fed at the junction of the two ends. As it can be easily inferred from Fig.8.1, there are two parameters which describe the loop antenna behavior: circumference diameter and radius of the wire. In this study a variation of both characteristics would be carried out in order to extract a better understanding of the complex resonant procedures occurring in that kind of structures. Being mainly interesting in resonant loop antennas looking at Fig.8.1 the reactance of the loop antenna approaches to zero when $\beta b = 0.5, 1.5, 2.5$ (antiresonant points) and $\beta b = 1, 2, 3$(resonant points) being $\beta b = 2\pi b/\lambda$ (circumference/wavelength) . The resistance obtains relative maximum near the antiresonant points and relative minimum near the resonant points.

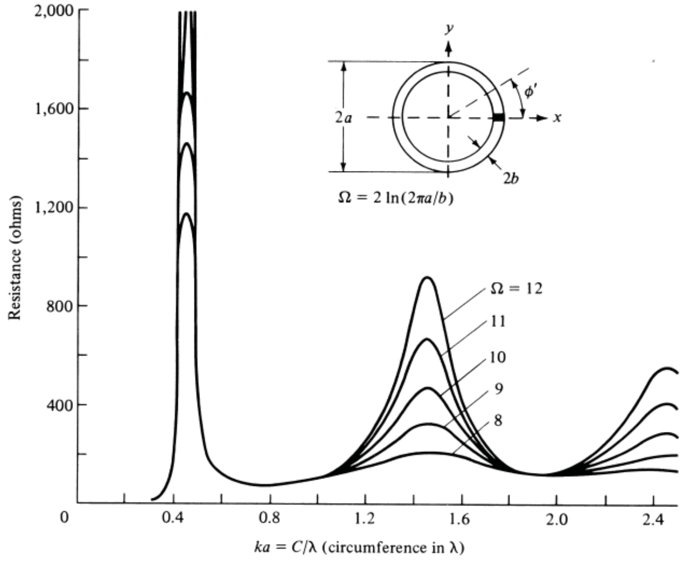

(a) Impedance

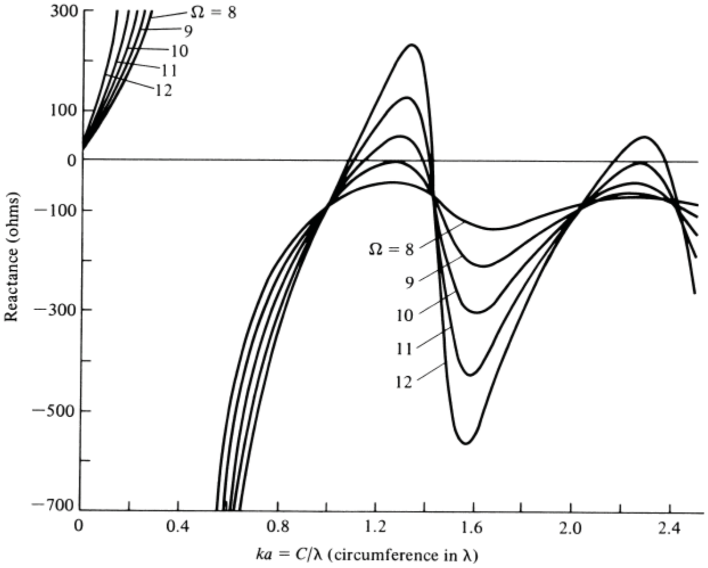

(b) Reactance

Figure 8.1: Input impedance of circular-loop antennas

Firstly, the radius of the loop a has been set, which would determine the electrical behavior of the loop in terms of electrically small (circumference much lower than the wavelength) or large (circumference of free-space wavelength order). Furthermore, depending of the thickness of the wire the resistance will change its value. According to different bibliography we have set parameter Ω to be equal to 12. In that way, given the radius of the loop a and Ω parameter, b can be easily obtained.

8.2 Gaussian Pulse selected

Recalling 2.2.3 the Gaussian pulse selected was set to be as $\tau/\tau_a = 0.076$ where $\tau_a = 2b/c_0$ being b the radius of the loop and c_0 the speed of light. Taking as circumference of the loop barely one wave-length which means the first resonant length for a electrically large antenna and making some calculations the maximum frequency of the Gaussian pulse that fulfill the former condition is 5.5 GHz. This is valid for the lower frequency limit in the frequency range $0.3GHz \rightarrow \lambda = 1m$

8.3 Loop radius

Regarding Fig.8.1 has been decided to proceed as follows. A wave-length within the range of study is selected such as $f = 3GHz \rightarrow \lambda = 0.1m$. Then, a curve for the resistance and reactance in Fig.8.1 has to be chosen. In this case, the curve corresponding with $\Omega = 12$ has been selected since it can be appreciated several lengths where the reactance is equal to zero. Although at certain circumference lengths the resistance is large and derives in impractical antennas, in this research antiresonant points have been also simulated by selecting a proper internal resistance. In addition, following [1],a loop antenna which length holds $\tau/\tau_a = 0.076$ where $\tau_a = 2b/c_0$ being b the radius of the loop and c_0 the speed of light has been also simulated. In that way, λ has been set to be equal to 1.

λ (m)	Circumference $kA = C/\lambda$ (λ)	Circumference (m)
0.1	1.1	0.11
0.1	1.5	0.15
0.1	2.2	0.22
1	1.1	1.1

Table 8.1: Loop antenna physical parameters.

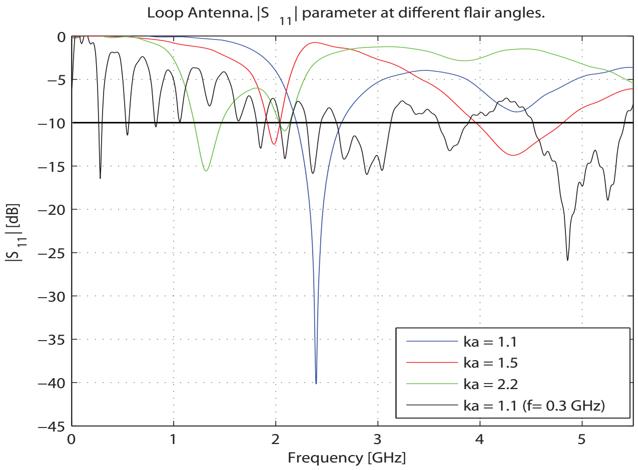

Figure 8.2: S_{11} parameter of bow-tie antennas with different flair angle.

8.3.1 Poles Distribution in frequency complex plane

Firstly, let us focus the attention on the S_{11} parameter in order to figure out the behavior of the structures simulated in terms of impedance matching along the frequency bandwidth. As it can be observed in Fig.8.2 resonance for the first loop occurs at roughly 2.4 GHz instead of 3 GHz. The reason of the shifting might be that the length has not been exactly selected and possible inaccuracies in the full wave procedure solver adopted. As long as the circumference of the loop increases the first resonance lies on larger wave-lengths and consequently at lower frequencies. The loop designed to operate at 0.3 GHz is found to resonate at several frequencies along the whole frequency range.

Let us now focus on the pole distribution of these antennas. As it can be observed in Fig.8.3, the group of dominant poles enclosed by ellipses seem to appear at the same frequencies as the antennas resonate. However, in the case of the loop with $kA = 1.5$ a crowded set of poles at roughly 1 GHz appears with larger damping coefficients than the dominant poles though. Regarding the pole distribution of the largest antenna seems that several poles show up at different frequencies.

Assuming that all the loop antennas simulated are electrically large is well-known that the direction of maximum radiation for the system reference adopted (see Fig.8.4) is along the Z-axis. However, the radiated electric

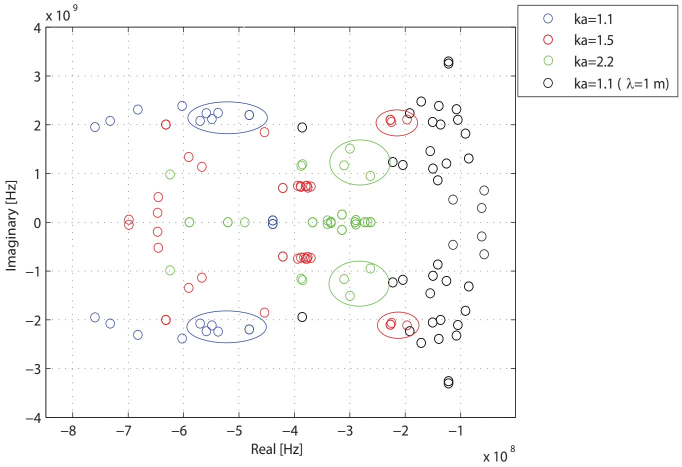

Figure 8.3: Poles distribution in complex plane of loop antennas with different size. Poles which energy holds $\varepsilon_{n,m,k}/\varepsilon_{max} \geq 0.1$ are displayed.

field has both components θ and ϕ to take into account at different azimuth angles though. The cutting plane given by $\phi = 0°$ meets E_ϕ-component as the dominant component. On the other hand, at the cutting plane given by $\phi = 90°$ has as most important component E_θ. Then, both components of the transient radiated fields will be studied at the direction of maximum radiation for each loop antenna.

Let us now take a look to the radiated field at direction of maximum radiation. In Fig.8.5 the E_ϕ-component for each loop antenna is shown denoting that the time behavior matches with the frequency one. The loop antennas resonating at lower frequencies present a time response wider. In addition, in the larger loops seems to appear contributions from the second resonant frequency. In Fig.8.6 is shown the spatial distribution of E_ϕ-component for the loop antenna $kA = 1.1$ at the plane ZX. As expected, the maximum radiation lies on Z-axis.

Although, apparently dominant poles have been found to appear at resonant frequencies, a clear relation between the length of the loop radius and the poles distribution has not been concluded. The high number of poles needed makes difficult to retrieve those ones responsible uniquely for the antenna response. In fact, the poles analyzed might be also related with the excitation signal making even harder the interpretation.

Having analyzed different loop antennas and having not reached to any

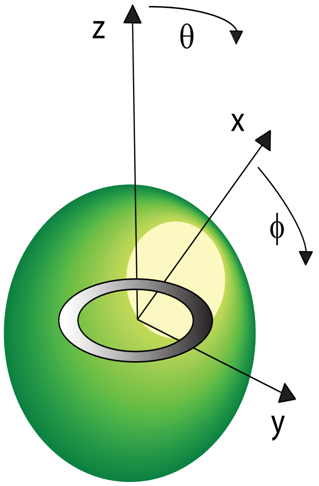

Figure 8.4: Loop antenna enclosed by a spherical Huygens surface. Reference system selected.

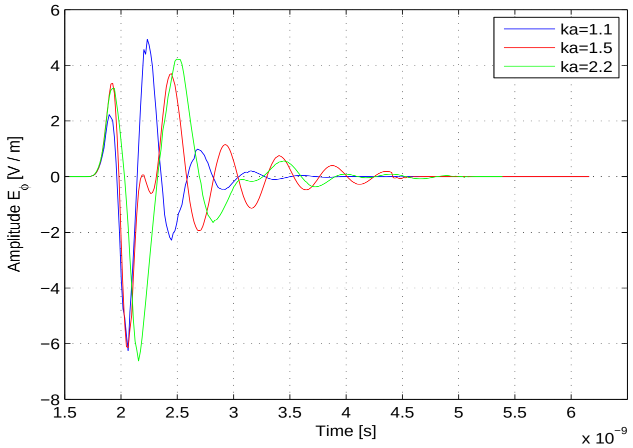

Figure 8.5: E_{phi}-component for each loop antenna at the direction of maximum radiation. $\boldsymbol{r} = \{r = 0.5, \theta = 0, \phi = 0\}$

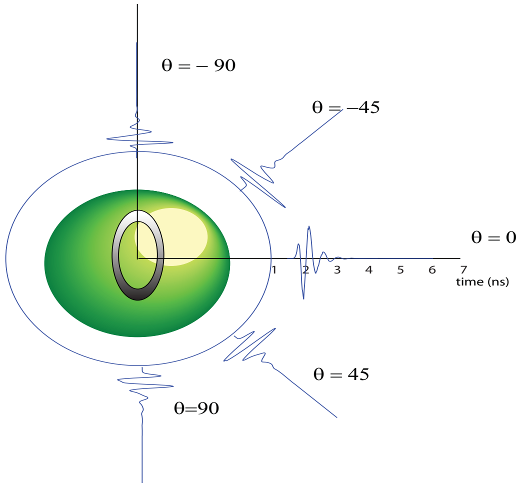

Figure 8.6: Spatial distribution of E_ϕ-component for the loop antenna $kA = 1.1$

trend that defines the impact of changing the loop radius on the response of the device, three additional structures with finer step increment of the radius have been analyzed. In Tab.(8.2) it can be observed these new antennas simulated together with the already studied.

λ (m)	Circumference $kA = C/\lambda$ (λ)	Circumference (m)
0.1	0.5	0.05
0.1	0.6	0.06
0.1	0.8	0.08
0.1	1.1	0.11
0.1	1.5	0.15
0.1	2.2	0.22
1	1.1	1.1

Table 8.2: Loop antenna physical parameters.

So, let us focusing, as it has been done along all this thesis, in the matching behavior first. Observing Fig.8.7, it can be derived that as long as the radius increases the resonant frequency decreases its values. Although not every antenna is perfectly matched, in this research the main interest is not design excellent radiators.

Then, looking at Fig.8.8, it might be inferred that dominant poles are found to be in the negative complex frequencies belonging to the matched frequencies displayed in Fig.8.7. In addition, it can be noticed that besides

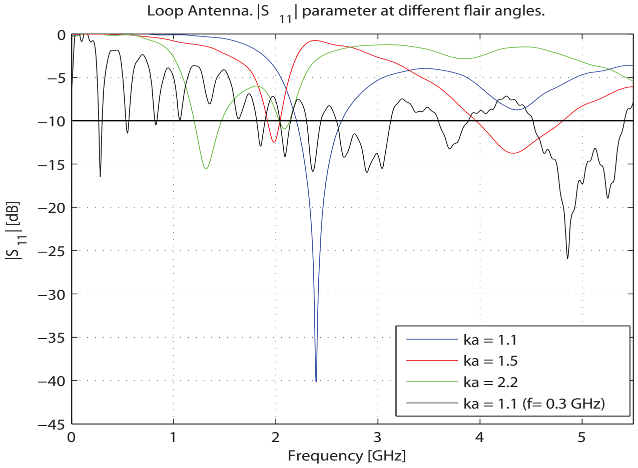

Figure 8.7: S_{11} parameter of bow-tie antennas with different flair angle.

the case which $kA = 1.1$ the dominant poles own similar damping coefficients. Then the attenuation of the dominant poles is pretty similar. This result differs from the dipole antenna case where the attenuation decreased from smaller to larger structures.

8.4 Wire radius

In this section, by changing the thickness of the wire an attempt to figure out the consequences in the location of the pole representation in the complex plane has been done. To this end, loop with barely the same length but different wire thickness have been simulated (see Fig.8.3). Following Fig.8.3, there are two cases of study. The first one ($kA \simeq 1.2$) involves first and second rows from afore-mentioned table and the second case ($kA \simeq 2.2$) takes third and fourth. Firstly, its matching characteristics must be studied.

λ (m)	Circumference $kA = C/\lambda$ (λ)	Circumference (m)	Ω
0.1	1.1	0.11	12
0.1	1.3	0.13	10
0.1	2.2	0.22	12
0.1	2.3	0.23	10

Table 8.3: Loop antenna physical parameters.

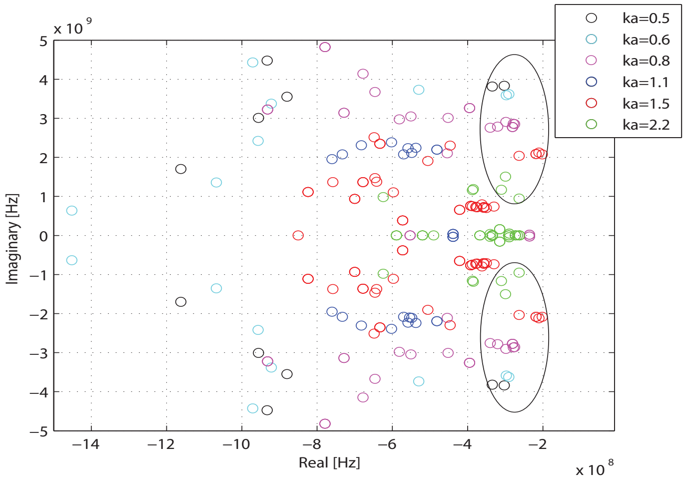

Figure 8.8: Poles distribution in complex plane of loop antennas with different size. Poles which energy holds $\varepsilon_{n,m,k}/\varepsilon_{max} \geq 0.1$ are displayed.

A priori, it is known that by increasing the wire thickness a enlargement of the bandwidth must be experienced. Then, in Fig.8.9 this phenomena can be observed. A bandwidth enlargement denotes a reduction in late-domain contribution. Thus, the dominant poles displayed in Fig.8.10 tend to move to the right side of the complex plane acquiring larger damping coefficients and then shorting the time response.

In order to provide a better understanding let us focus on the radiated field at the direction of maximum radiation. As it can be seen in Fig.8.11, those results are consistent with the pole distribution and $|S_{11}|$ parameter study. The late-time ringing is reduced due to the thicker wire allowing wider frequency bandwitdh.

8.5 Conclusions

In this chapter a loop antenna has been analyzed. Along this analysis it has been found that indeed dominant poles seem to appear at the resonant frequencies. However, the pole distribution of this kind of structure has not been found easy to interpret since several poles account for the transient response of this antenna. Then, a clear relation between the pole distribution and the loop physical parameters has not been achieved.

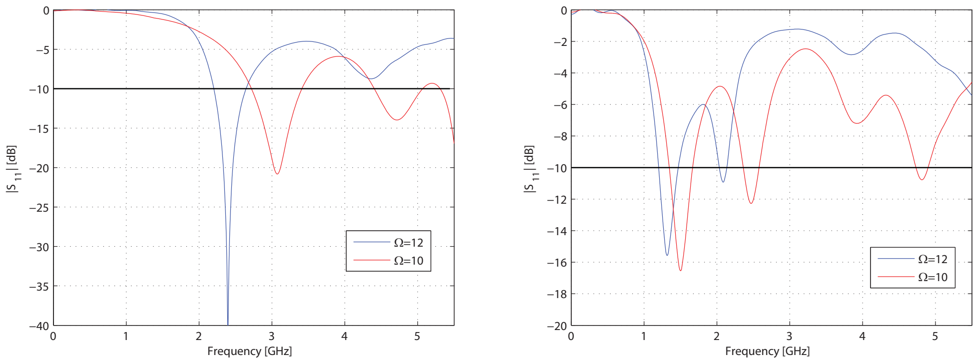

(a) $kA = 1.2$ (b) $kA = 2.2$

Figure 8.9: S_{11} parameter of loop antennas with different radius and wire thicknesses.

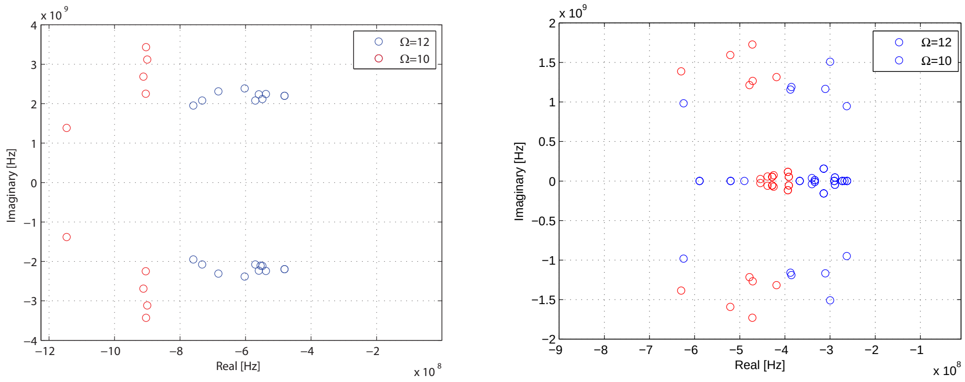

(a) $kA = 1.2$ (b) $kA = 2.2$

Figure 8.10: Poles distribution in complex plane of loop antennas with different radius and wire thicknesses.Poles which energy holds $\varepsilon_{n,m,k}/\varepsilon_{max} \geq 0.1$ are displayed.

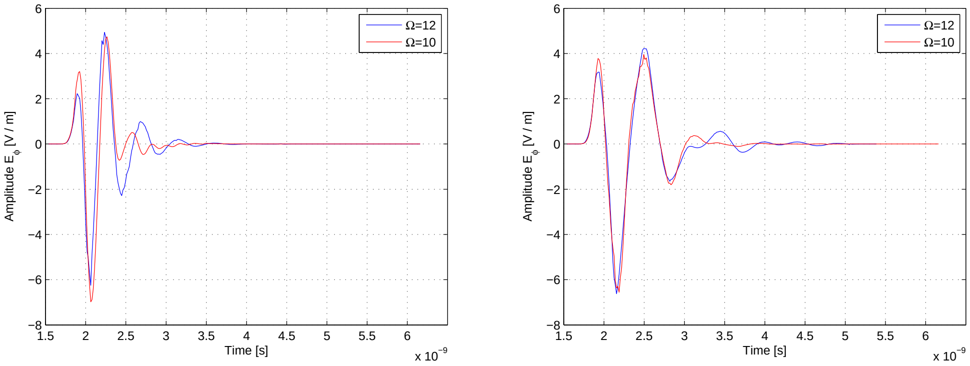

(a) $kA = 1.2$ (b) $kA = 2.2$

Figure 8.11: E_ϕ-component of radiated field at direction of maximum radiation. $\boldsymbol{r} = \{r = 0.5, \theta = 0, \phi = 0\}$

Chapter 9

Conclusions and Future Work

In this thesis different antennas have been characterize by a pole/residue representation denoting the complex resonant processes occurring in those structures. This new formalism developed by the IRCTR as far as the knowledge of the author of this report has not been implemented in a commercial software before. In addition, a analytical and numerical way of implementing such algorithm has been provided. In terms of antenna study, at least three kind of antennas have been analyzed: dipole antenna, bow-tie antenna and loop antenna. However, only in the first case a clear physical relation between the dominant complex poles and the antenna geometry has been found. On the other hand, the other two cases it would be recommended further investigation.Furthermore, it has been observed that the pole order has to be set considering the length of the time signal as well as the frequencies involved. Since more frequencies are accounting for the antenna response likely more exponential functions would be needed for an accurate representation.

To summarize, some of the goals predefined in this thesis has been achieved:

- Implementation of a new formalism for represent radiated fields as outgoing non-uniform spherical waves which decay is given by the spatial distance and the real part of the poles used in the representation.
- Characterization of dipole, bow-tie and loop antennas.
- Relationship between the length of the dipole antenna and the pole distribution in the complex frequency plane.

As consideration of the author, future work in this field would require a further investigation of bow-tie and loop antennas as well as more sophisticated structures. In addition, as commented along this thesis work the representation of the pole distribution may content poles accounting for the excitation signal. Then, a different excitation signal may be considered for the study. Another option might be, deconvolve the density currents splitting the impulsional response of the antenna and the excitation signal.

Bibliography

[1] Glenn S. Smith ”Teaching antenna radiation from a time-domain perspective” *American Journal of Physics*, Atlanta, USA, 2001.

[2] First Report and Order (FCC 02-48). ”New Public Safety Applications and Broadband internet access among uses envisioned by FCC authorization of Ultra-Wideband Technology” Action by the Comission, February 14, 2002.

[3] M. Pausini, ”Autocorrelation Receivers for Ultra Wideband Wireless Communications”, pp 10-12, 2007.

[4] D. Caratelli, A. Yarovoy and L. P. Ligthart, ”Unified time- and frequency-domain approach for accurate modelling of electromagnetic radiation processes in ultra-wideband antennas,” *European Microwave Conference 2009*, Rome, Italy, pp. 946-949, Oct. 2009.

[5] L. B. Felsen and N. Marcuvitz, ”Radiation and Scattering of Waves” New York:Prentice-Hall/IEEE,1994.

[6] A. Shlivinski, E. Heyman, and R. Kastner, ”Antenna characterization in the time domain” *IEEE Trans. Antennas Propagat.*, vol.45, no.7, pp. 1140-1149, July 1997.

[7] T. M. MacRobert and L. N. Sneddon, ”Spherical Harmonics: An Elementary Treatise on Harmonic Functions, with Applications” 3rd ed. Oxford, U.K.:Pergamon Press,1967.

[8] S. Grivet-Talocia, F. Canavero, I. Maio, and I. Stievano, ”Reduced-order macromodeling of complex multiport interconnects.” in *Proc. URSI General Assembly*, Maastrictht, Aug, 19-23, 2002.

[9] S. Grivet-Talocia, "Generation of passive macromodels from transient port responses." in *Proc. IEEE Topical Meeting on Electrical Performance of Electronic Packaging*, Princeton,NJ, Oct. 27-29, 2003.

[10] S. Grivet-Talocia, "Packaged macromodeling via time-domain vector fitting." *IEEE Microwave Wireless Comp. Lett.,*, vol. 13, pp. 472-474,Nov. 2003.

[11] O. M. Bucci and G. Franceschetti, "Approximate calculation of time-domain effective height for aperture antennas" *IEEE Trans. Antennas Propagat.*, vol.53, no.3, pp. 1054-1061, March 2005.

[12] S. Licul and W. A. Davis, "Unified frequency and time-domain modeling and characterization" *IEEE Trans. Antennas Propagat.*, vol.53, no.9, pp. 2882-2888, Sep. 2005.

[13] O. M. Bucci and G. Franceschetti, "On the spatial bandwidth of scattered fields" *IEEE Trans. Antennas Propagat.*, vol.35, no.12, pp. 1445-1455, Dec. 1987.

[14] O. M. Bucci, C. Gennarelli and C. Savarese, "Optimal interpolation of radiated fields over a sphere" *IEEE Trans. Antennas Propagat.*, vol.39, no.11, pp. 1633-1643, Nov. 1991.

[15] Y. Hua and T. K. Sarkar, "Matrix pencil method for estimating parameters of exponentially damped/undamped sinusoids in noise" *IEEE Trans. Acoust. Speech, Signal Processing.*, vol.38, no.5, pp. 814-824, May. 1990.

[16] T. K. Sarkar and O. Pereira, "Using the Matrix Pencil method to estimate the parameters of a sum of complex exponentials." *IEEE Trans. Antennas Propagat.*, vol.37, no.1, pp. 48-55, 1995.

[17] I. S. Gradshteyn and I. M. Ryzhik, "Table of Integrals, Series, and Products" 7th ed. New York:Academic Press, 2007.

[18] D. B. Davidson, "Computational Electromagnetics for RF and Microwave Engineering" 1st ed. Cambridge:university Press, 2005.

[19] J. A. Stratton, "Electromagnetic Theory" Piscataway, NJ:IEEE Press, 2007.

[20] D. Caratelli and A. Yarovoy, "Accurate Evaluation of the Time-Domain Gain of Transient Antennas" Delft University of Technology, IRCTR.

[21] CST Helps contents

[22] B. Gustavsen and A. Semlyen, "Rational approximation of frequency domain responses by Vector Fitting" *IEEE Trans. Power Delivery*, vol. 14, no. 3, pp. 1052-1061, July 1999.

[23] B. Gustavsen, "Improving the pole relocating properties of vector fitting" *IEEE Trans. Power Delivery*, vol. 21, no. 3, pp. 1587-1592, July 2006.

[24] D. Deschrijver, M. Mrozowski, T. Dhaene, and D. De Zutter, Macromodeling of Multiport Systems Using a Fast Implementation of the Vector Fitting Method *IEEE Microwave and Wireless Components Letters*, vol. 18, no. 6, pp. 383-385, June 2008.

[25] Se-Jung Moon and A.C. Cangellaris, "Order estimation for time-domain vector fitting" *IEEE 18th Conference on Electrical Performance of Electronic Packaging and Systems* pp. 69-72, 2009.

[26] Constantine A. Balanis "Antenna Theory" 3rd ed. Wiley-Interscience

[27] C.E. Smith, C. M. Butler and K. R. Umashankar, "Characteristics of Wire Biconical Antenna" *Microwave Journal* pp. 37-40, September 1979.

Analysis of Antenna Transient Radiation

Master Thesis Defense

Pablo Rodriguez Ulibarri

Committee Members:
Prof. A. Yarovoy
Prof. B.J. Kooij
Dr. D. Caratelli
Dr. R. Remis

30-8-2010

Delft
University of
Technology

CONTENTS

INTRODUCTION

- Characterization of UWB antenna radiation: Frequency-domain
  - Does not provide physical insight into the electromagnetic behavior.
  - Large computational resources.
- Different approach: Time-domain
  - Superposition of non-uniform spherical waves ➔ Complex resonant processes.
- Goals:
  - Gain physical insight into the natural processes occurring in different antennas.
  - Find out relationship between those processes and the relevant geometrical characteristics of the structure.

INTRODUCTION

Time-Domain Perspective

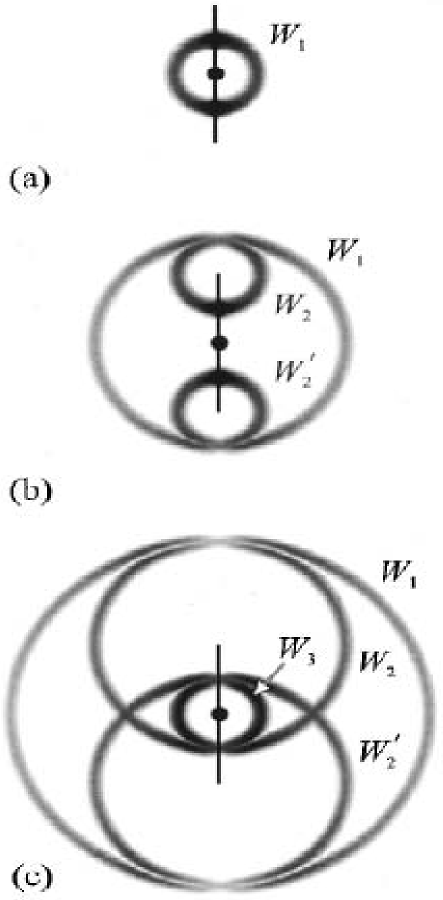

- Physical insight understanding.
- Gaussian pulse as excitation signal.
- Moving point charge.
  - Acceleration ➔ Radiation
- Antennas
  - Truncation, bending, discontinuity…
- Example:
  - Dipole Antenna
  - Gaussian pulse fitting four times in dipole arm.

INTRODUCTION

Problem description

- Problem: Analysis of transient radiation of different antennas using commercial available software.
- Block-Scheme:

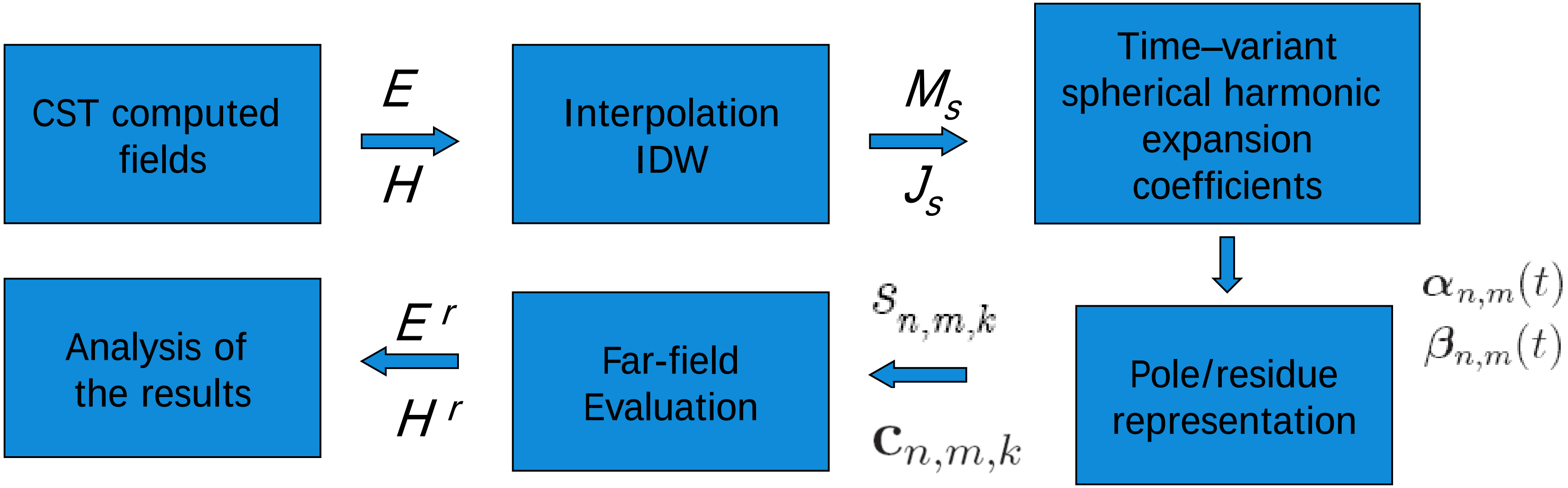

CST computed fields

E

H

Interpolation IDW

M_s

J_s

Time–variant spherical harmonic expansion coefficients

$\alpha_{n,m}(t)$

$\beta_{n,m}(t)$

Pole/residue representation

$s_{n,m,k}$

$\mathbf{c}_{n,m,k}$

Far-field Evaluation

E^r

H^r

Analysis of the results

POLE/RESIDUE MODELING

- Near to far-field transformation.
  - Free-space dyadic Green's functions
  - Equivalent Density currents

$$\mathbf{J}_s(r,\vartheta,\varphi) = \hat{\mathbf{r}} \times \mathbf{H}(R_h,\vartheta,\varphi,t),$$
$$\mathbf{M}_s(r,\vartheta,\varphi) = \mathbf{E}(R_h,\vartheta,\varphi,t) \times \hat{\mathbf{r}}.$$

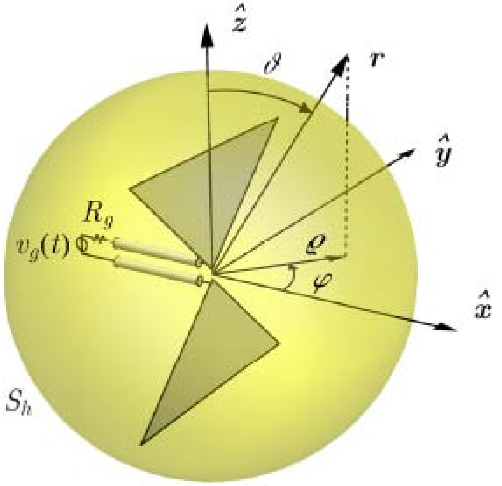

- Vector Slant-Stack Transform

$$\mathbf{E}(\mathbf{r},t) \simeq \frac{1}{4\pi r c_0} \int\!\!\int_{S_h} \hat{\mathbf{r}} \times [\eta_0 \hat{\mathbf{r}} \times \dot{\mathbf{J}}_\mathbf{s}(\vartheta',\varphi',\tau + t_h \cos\gamma) + \\ + \dot{\mathbf{M}}_\mathbf{s}(\vartheta',\varphi',\tau + t_h \cos\gamma)] dS',$$

$$\mathbf{H}(\mathbf{r},t) \simeq \frac{1}{\eta_0} \hat{\mathbf{r}} \times \mathbf{E}(\mathbf{r},t)$$

$t_h = R_h / c_0$

τ : Spherical wave delayed time

POLE/RESIDUE MODELING

- Spherical Harmonics
  - Set of solutions of Laplace equation.
  - Orthonormal Basis

$$Y_n^m(\vartheta,\varphi)=\sqrt{\frac{2n+1}{4\pi}\frac{(n-m)!}{(n+m)!}}P_n^m(\cos\vartheta)e^{-jm\varphi},$$

- Harmonic Expansion
  - Expansion/Projection
  - Reconstruction

$$\boxed{\left\{\begin{array}{c}\alpha_{n,m}(t)\\ \beta_{n,m}(t)\end{array}\right\}}=\int_0^{2\pi}\int_0^{\pi}\left\{\begin{array}{c}\mathbf{J}_s(\vartheta,\varphi,t)\\ \mathbf{M}_s(\vartheta,\varphi,t)\end{array}\right\}Y_n^{m*}(\vartheta,\varphi)\sin\vartheta d\vartheta d\varphi$$

$$\left\{\begin{array}{c}\mathbf{J}_s(\vartheta,\varphi,t)\\ \mathbf{M}_s(\vartheta,\varphi,t)\end{array}\right\}=\sum_{n=0}^{N}\sum_{m=-n}^{n}\left\{\begin{array}{c}\alpha_{n,m}(t)\\ \beta_{n,m}(t)\end{array}\right\}Y_n^m(\vartheta,\varphi),$$

Time-variant expansion coefficients

POLE/RESIDUE MODELING

- SEM-based Representation of time-variant expansion coefficients:

$$\left\{\begin{array}{c}\mathbf{a}_{n,m}(t)\\ \mathbf{b}_{n,m}(t)\end{array}\right\} = \sum_{k=1}^{K}\left\{\begin{array}{c}\mathbf{a}_{n,m,k}\\ \mathbf{b}_{n,m,k}\end{array}\right\} e^{s_{n,m,k}t}u(t) + \cancel{\left\{\begin{array}{c}\mathbf{A}_{n,m}(t)\\ \mathbf{B}_{n,m}(t)\end{array}\right\}} \longrightarrow \boxed{\begin{array}{c} s_{n,m,k}\\ \mathbf{a}_{n,m,k}\ ,\ \mathbf{b}_{n,m,k}\end{array}}$$

- Combining and substituting equations:

$$\left\{\begin{array}{c}\mathbf{E}(r,\vartheta,\varphi,t)\\ \mathbf{H}(r,\vartheta,\varphi,t)\end{array}\right\} \simeq \frac{R_h^2}{4\pi r c_0}\sum_{n=0}^{N}\sum_{m=-n}^{n}\sum_{k=1}^{K} s_{n,m,k}e^{s_{n,m,k}\tau}\left\{\begin{array}{c}\mathrm{e}_{n,m,k}\\ \mathrm{h}_{n,m,k}\end{array}\right\}\cdot$$

$$\cdot\int\int_{\Omega_h} e^{s_{n,m,k}t_h\cos\gamma}Y_n^m(\vartheta',\varphi')\sin\vartheta' d\vartheta' d\varphi',$$

Where:

$$\left\{\begin{array}{c}\mathrm{e}_{n,m,k}\\ \mathrm{h}_{n,m,k}\end{array}\right\} = \hat{\mathrm{r}}\times\left\{\begin{array}{c}\eta_0\hat{\mathrm{r}}\times\mathrm{a}_{n,m,k}+\mathrm{b}_{n,m,k}\\ -\mathrm{a}_{n,m,k}+\hat{\mathrm{r}}\times\mathrm{b}_{n,m,k}/\eta_0\end{array}\right\}$$

POLE/RESIDUE MODELING

- Evaluation of radiation integrals:

$$\iint_{\Omega_h} e^{\frac{s_{n,m,k}}{c_0} R_h \cos\gamma}\, Y_n^m(\vartheta',\varphi')\, d\Omega' =$$

$$= 4\pi\, i_n\left(\frac{s_{n,m,k}}{c_0} R_h, \min\left\{1, \frac{c_0\tau}{R_h}\right\}\right) u\left(\frac{c_0\tau}{R_h}\right) Y_n^m(\vartheta,\varphi)$$

Incomplete modified Spherical Bessel functions

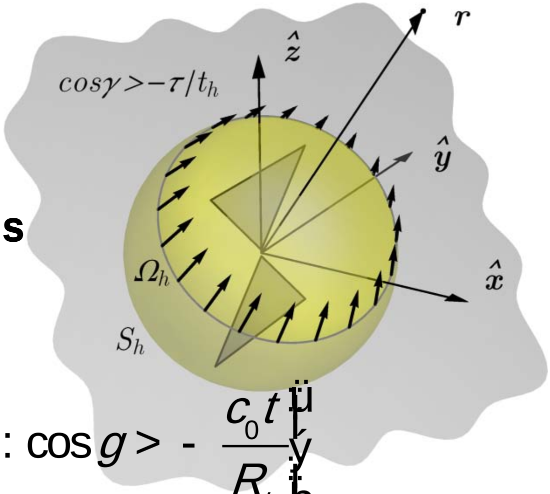

$$\Omega_h = \left\{(\vartheta',\varphi') : \cos\gamma > -\frac{c_0\tau}{R_h}\right\}$$

- Radiated field

$$\left\{\begin{array}{c}\mathbf{E}(r,\vartheta,\varphi,t)\\ \mathbf{H}(r,\vartheta,\varphi,t)\end{array}\right\} \simeq \frac{t_h R_h}{r} \sum_{n=0}^{N} \sum_{m=-n}^{n} \sum_{k=1}^{K} s_{n,m,k} e^{s_{n,m,k}\tau} u\left(\frac{c_0\tau}{R_h}\right) \cdot \hat{i}_n\left(s_{n,m,k} t_h, \frac{\tau}{t_h}\right) Y_n^m(\vartheta,\varphi) \left\{\begin{array}{c}\mathbf{e}_{n,m,k}\\ \mathbf{h}_{n,m,k}\end{array}\right\}$$

Spherical waves attenuating along with the radial distance and the real part of the complex poles

POLE/RESIDUE MODELING

Analytical Evaluation of Spherical expansion coefficients

- Evaluating Density currents.
  - Evaluating electromagnetic field.
    - CST Microwave Studio
      - FIT technique
      - Time domain solver
  - IDW interpolation technique.

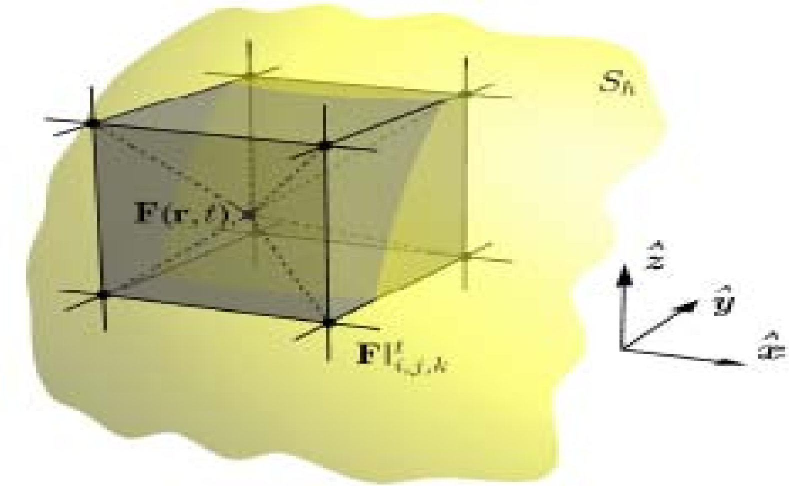

$$\mathrm{F}(\mathrm{r},t) \simeq \frac{\sum_{i,j,k} w(\bar{\mathrm{r}}\mid_{i,j,k} - \mathrm{r})\mathrm{F}\mid^{t}_{i,j,k}}{\sum_{i,j,k} w(\bar{\mathrm{r}}\mid_{i,j,k} - \mathrm{r})}$$

$$w(\mathbf{R}) = |\mathbf{R}|^{-2}$$

ANALYTICAL PROCEDURE

Analytical Evaluation of Spherical expansion coefficients

- Cardinal Series representation (CS).

$$\mathbf{I}_S(\vartheta,\varphi,t) \simeq \mathbf{I}_S(0,\varphi,t)\Pi_N(\vartheta) + \sum_{n=1}^{N}\Big\{\Pi_N(\vartheta-\vartheta_n)\cdot\sum_{m=-M}^{M_n}\mathbf{I}_S(\vartheta_n,\varphi_{n,m},t)\Pi_{M_n}(\varphi-\varphi_{n,m})$$

$$-\Pi_N(\vartheta+\vartheta_n)\sum_{m=-M_n}^{M_n}\mathbf{I}_S(\vartheta_n,\varphi_{n,m},t)\cdot\Pi_{M_n}(\varphi+\pi-\varphi_{n,m})\Big\}$$

- Expansion Orders

$$N = \left\lceil \frac{2\pi\chi R_h}{c_0 T_g} \right\rceil$$

X =1.1

Rh: Huygens radius

Tg : Pulse-length

$$\longrightarrow \quad \vartheta_n = \frac{2\pi n}{2N+1}$$

Elevation angle

$$M_n = \left\lceil \frac{2\pi R_h[1+(\chi-1)\sin^{-\frac{2}{3}}(\vartheta_n)]}{c_o T_g} \right\rceil \quad \longrightarrow \quad \varphi_{n,m} = \frac{2\pi m}{2M_n+1}$$

Azimuth angle

- Time-variant expansion coefficients:

$$\boxed{\psi_{n,m}(t) = \left\langle \mathbf{I}_S(\vartheta,\varphi,t), Y_n^m(\vartheta,\varphi) \right\rangle}$$

ANALYTICAL PROCEDURE

Time-domain vector fitting

- Pole relocation technique:

Laplace Transform

$$\psi_{n,m}(t) = \sum_{k=1}^{K} \mathbf{c}_{n,m,k} e^{s_{n,m,k} t} u(t) \longrightarrow \Psi_{n,m}(p) = \mathcal{L}\{\psi_{n,m}(t)\} = \sum_{k=1}^{K} \frac{\mathbf{c}_{n,m,k}}{p - s_{n,m,k}}$$

$$\downarrow$$

$$\Upsilon_{n,m}(p) = 1 + \sum_{k=1}^{K} \frac{R_{n,m,k}}{p - q_{n,m,k}} = \frac{\prod_{k=1}^{K}(p - \zeta_{n,m,k})}{\prod_{k=1}^{K}(p - q_{n,m,k})} \longrightarrow \Upsilon_{n,m}(p)\Psi_{n,m}(p) \simeq \sum_{k=1}^{K} \frac{\mathbf{M}_{n,m,k}}{p - q_{n,m,k}}$$

Scalar Weighting function
with known initial poles

Cancellation between zeros of scalar function and resonant poles of time-variant spherical wave coefficients must occur

Mid-goal: $\{R_{n,m,k}\}$ $\longrightarrow$ *Final goal:* $\{s_{n,m,k}\}$

ANALYTICAL PROCEDURE

Time-domain vector fitting

- Evaluation of Current vector residues in a Least-square sense:

$$\boxed{\sum_{k=1}^{K} e^{q_{n,m,k}t}\mathbf{M}_{n,m,k}} = \mathcal{L}^{-1}\left\{\sum_{k=1}^{K}\frac{\mathbf{M}_{n,m,k}}{p-q_{n,m,k}}\right\} \simeq \mathcal{L}^{-1}\left\{\Upsilon_{n,m}(p)\boldsymbol{\Psi}_{n,m}(p)\right\} = \boxed{\boldsymbol{\psi}_{n,m}(t) + \sum_{k=1}^{K} R_{n,m,k}\boldsymbol{\Theta}_{n,m,k}(t)}$$

where

$$\boldsymbol{\Theta}_{n,m,k}(t) = \mathcal{L}^{-1}\left\{\frac{\boldsymbol{\Psi}_{n,m}(p)}{p-q_{n,m,k}}\right\} = \int_0^t e^{q_{n,m,k}(t-t')}\boldsymbol{\psi}_{n,m}(t')dt'$$

$$\begin{pmatrix} \vdots & & \vdots & \vdots & & \vdots \\ e^{q_{n,m,1}t_j} & \cdots & e^{q_{n,m,K}t_j} & -\Theta_{n,m,1}(t_j) & \cdots & -\Theta_{n,m,K}(t_j) \\ \vdots & & \vdots & \vdots & & \vdots \end{pmatrix} \begin{pmatrix} \mathbf{M}_{n,m,1} \\ \vdots \\ \mathbf{M}_{n,m,K} \\ \mathbf{R}_{n,m,1} \\ \vdots \\ \mathbf{R}_{n,m,K} \end{pmatrix} = \begin{pmatrix} \vdots \\ \psi_{n,m}(t_j) \\ \vdots \\ \psi_{n,m}(t_T) \end{pmatrix}$$

Quadratic recursive equation

- Stop Criterion:

ε=10^{-3}

$$\frac{\sum_{k=1}^{K}\left|s_{n,m,k}-q_{n,m,k}\right|^2}{\sum_{k=1}^{K}\left|q_{n,m,k}\right|^2} < \varepsilon^2 \longrightarrow \sigma_{n,m,k} = -\left|\mathrm{Re}\left\{s_{n,m,k}\right\}\right|$$

Check and enforce passivity

- Energy indicator: $\varepsilon_{n,m,k} = \dfrac{1}{\eta_0}\displaystyle\int_0^{+\infty}\left|e^{s_{n,m,k}\tau}\mathbf{e}_{n,m,k}\right|^2 d\tau.$ $\quad \varepsilon_{n,m,k}/\varepsilon_{max} \geq \delta_\varepsilon$

ANTENNAS ANALYZED

- Canonical Antennas
  - Dipole Antenna
    - Length and wire radius.
  - Bow – Tie
    - Length and flair angle
  - Loop antenna
    - Loop radius and wire radius.

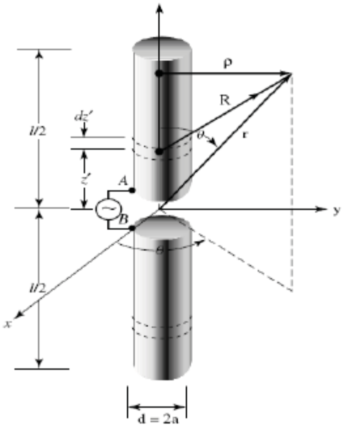

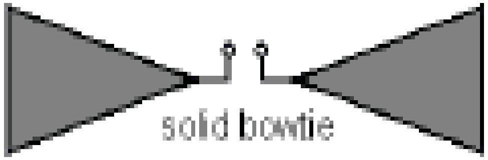

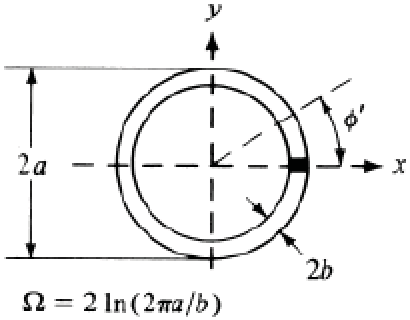

DIPOLE ANTENNA

Length study

- Half-wavelength dipole

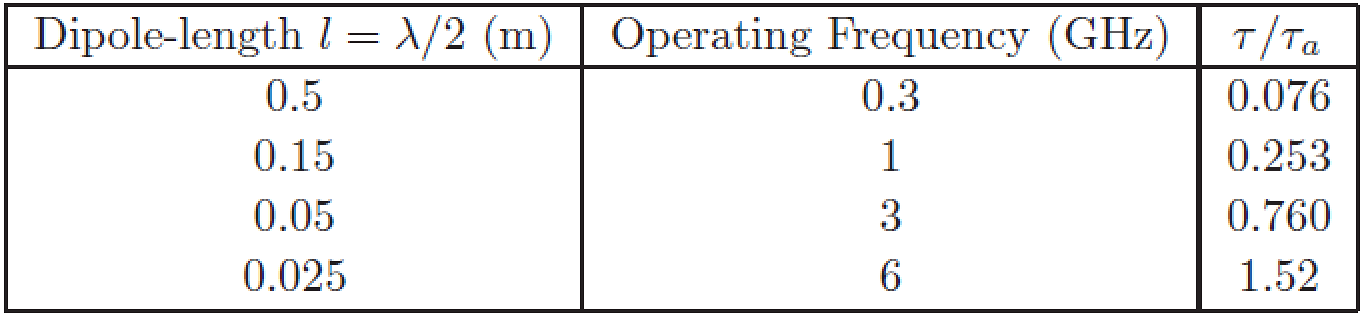

Dipole-length $l = \lambda/2$ (m)	Operating Frequency (GHz)	τ/τ_a
0.5	0.3	0.076
0.15	1	0.253
0.05	3	0.760
0.025	6	1.52

- Gaussian Pulse
  - τ/τ_a = Characteristic time / travel time
  - Frequency max = 7.63 GHz

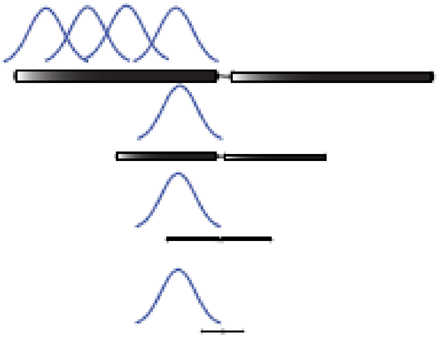

DIPOLE ANTENNA

Length study

$|S_{11}|$ Parameter of Dipoles with different length

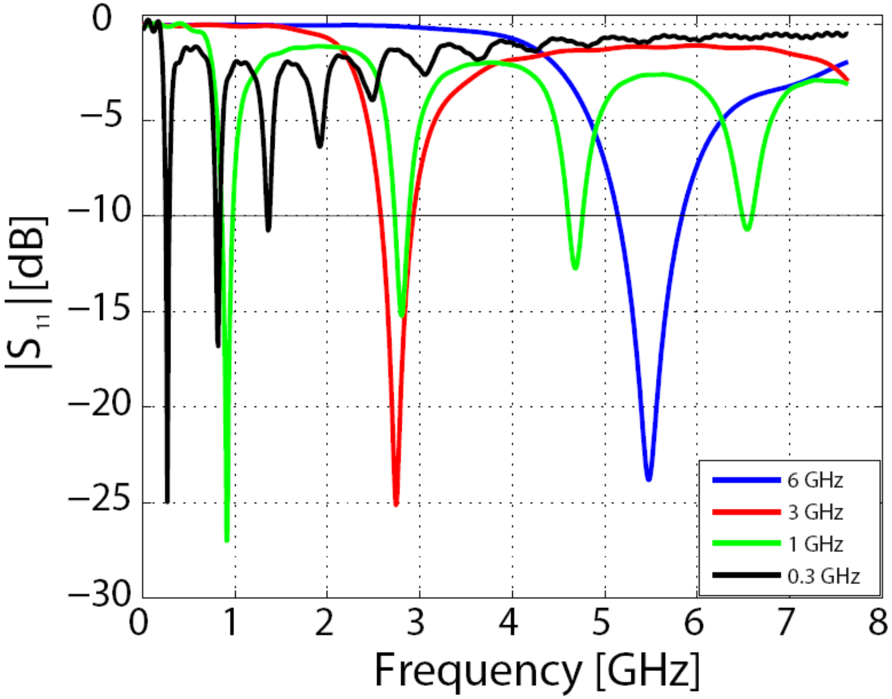

Poles distribution in complex frequency plane

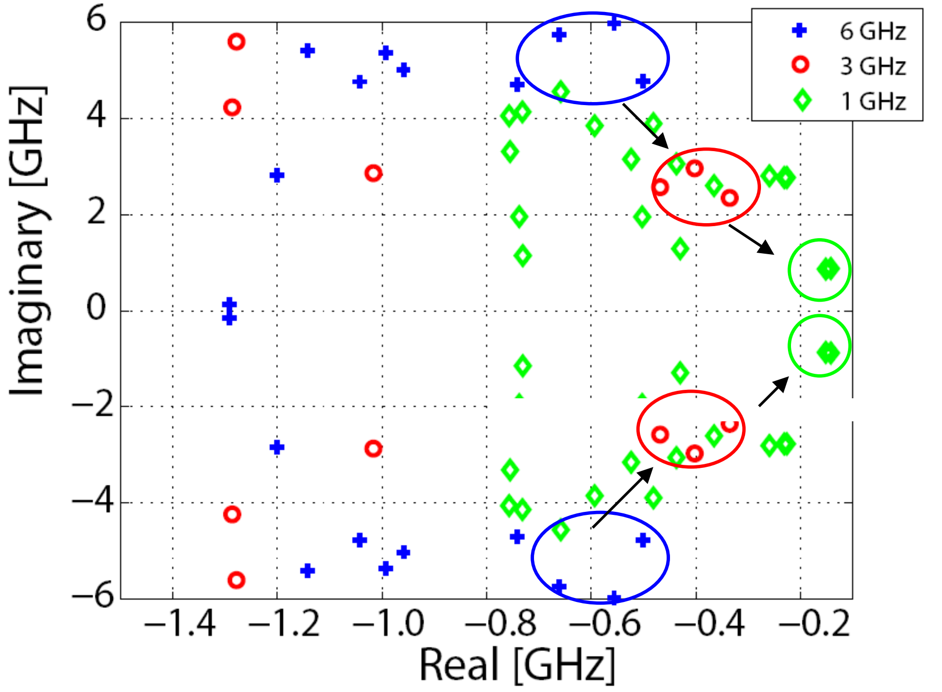

Dominant poles (weaker attenuation)

Poles Energy threshold 10^{-1}

DIPOLE ANTENNA

Length study

Larger dipoles need higher expansion and pole orders.

Larger dipoles have longer time responses.

Attenuation decreases as dipole length increases.

First resonance occurs at lower frequencies .

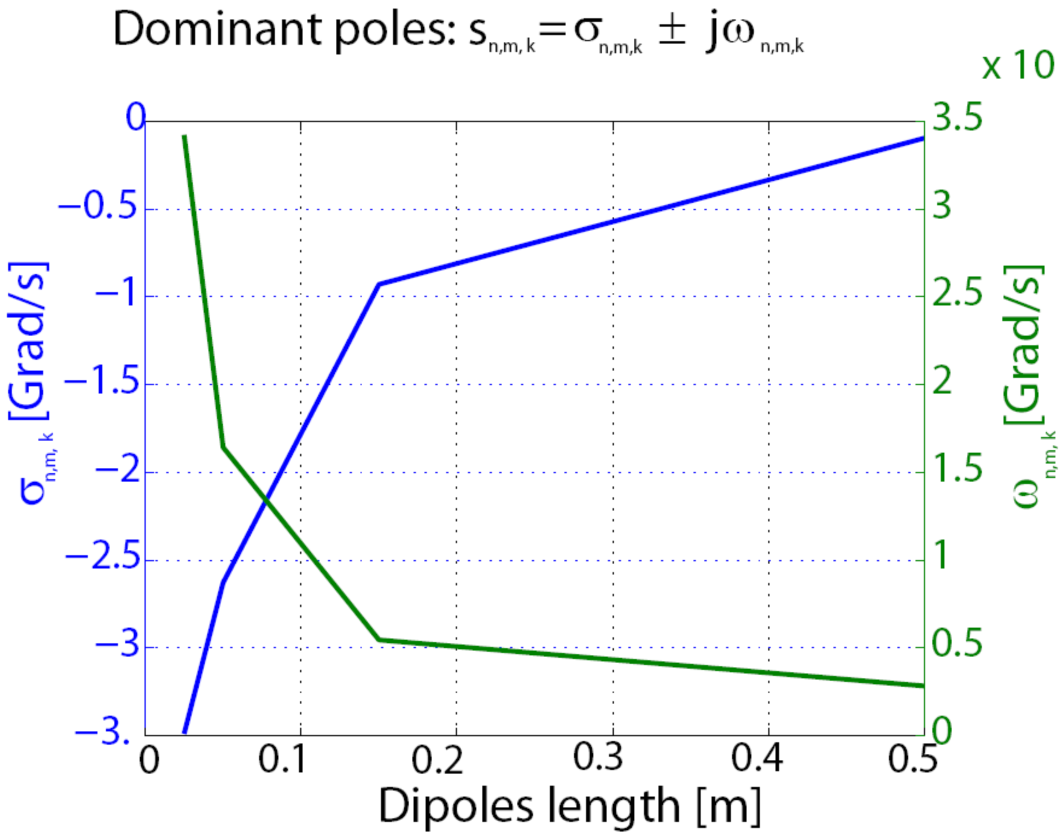

DIPOLE ANTENNA

Length study. Transient radiation

- Dipole operating at 6 GHz: Dominant poles contribution.

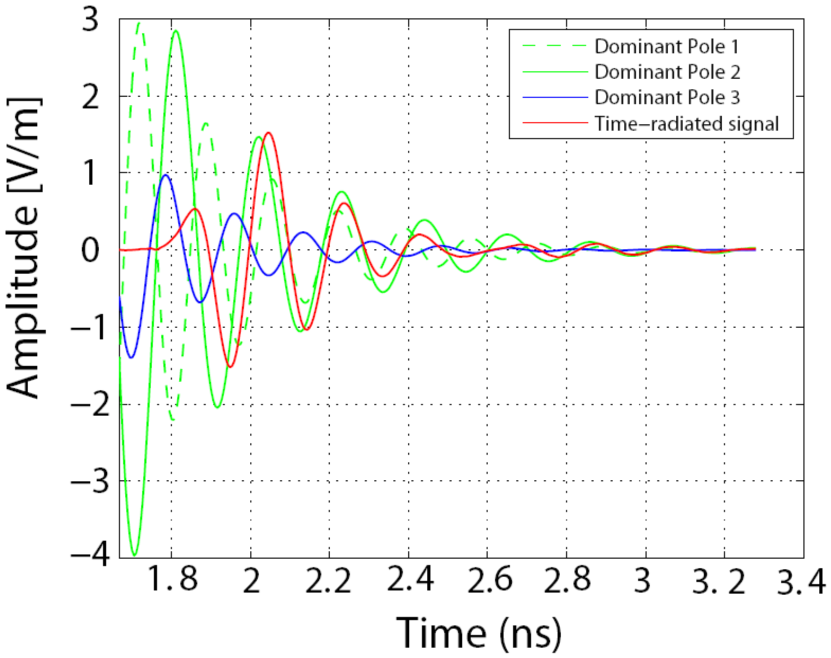

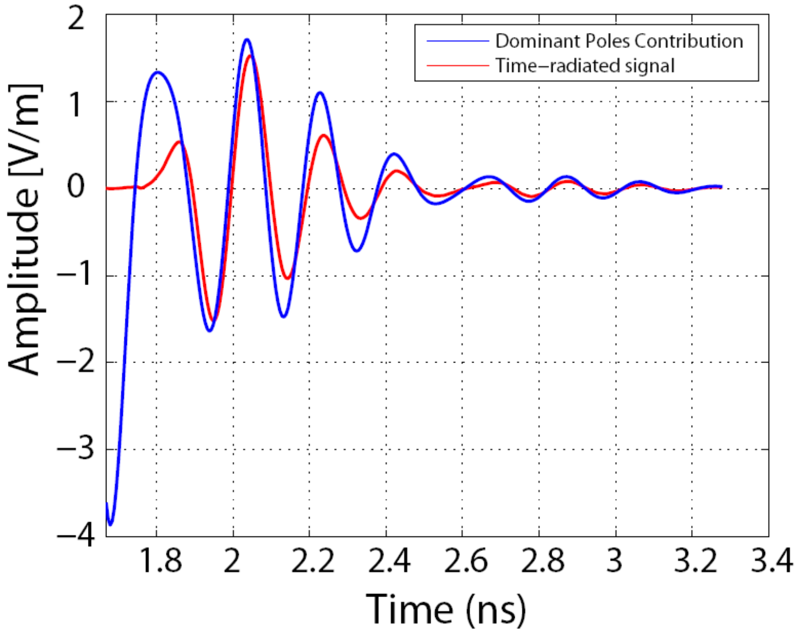

Three poles are mainly responsible for the late-time behavior.

DIPOLE ANTENNA

Length study. Transient radiation

- Spatial Distribution.

Outgoing non-uniform spherical waves.

Reflections appear instantaneously

Reducing the level of the feeding pulse.

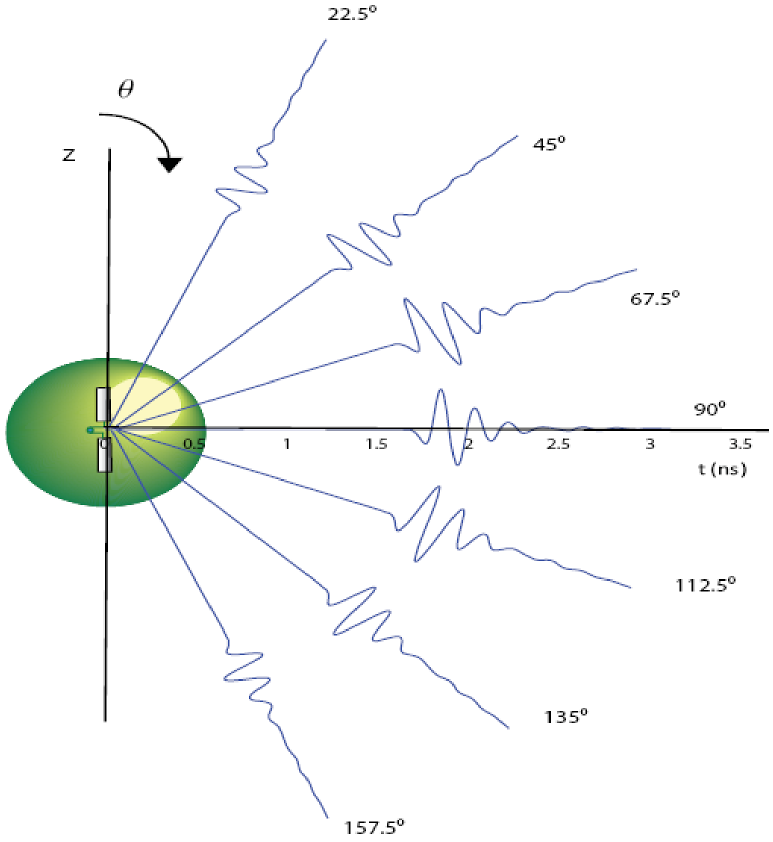

DIPOLE ANTENNA

Length study. Transient radiation

- Spatial Distribution.

Outgoing non-uniform spherical waves.

Reflected waves due to diffraction phenomena at the antenna ends.

Interfered constructively at the direction of maximum radiation.

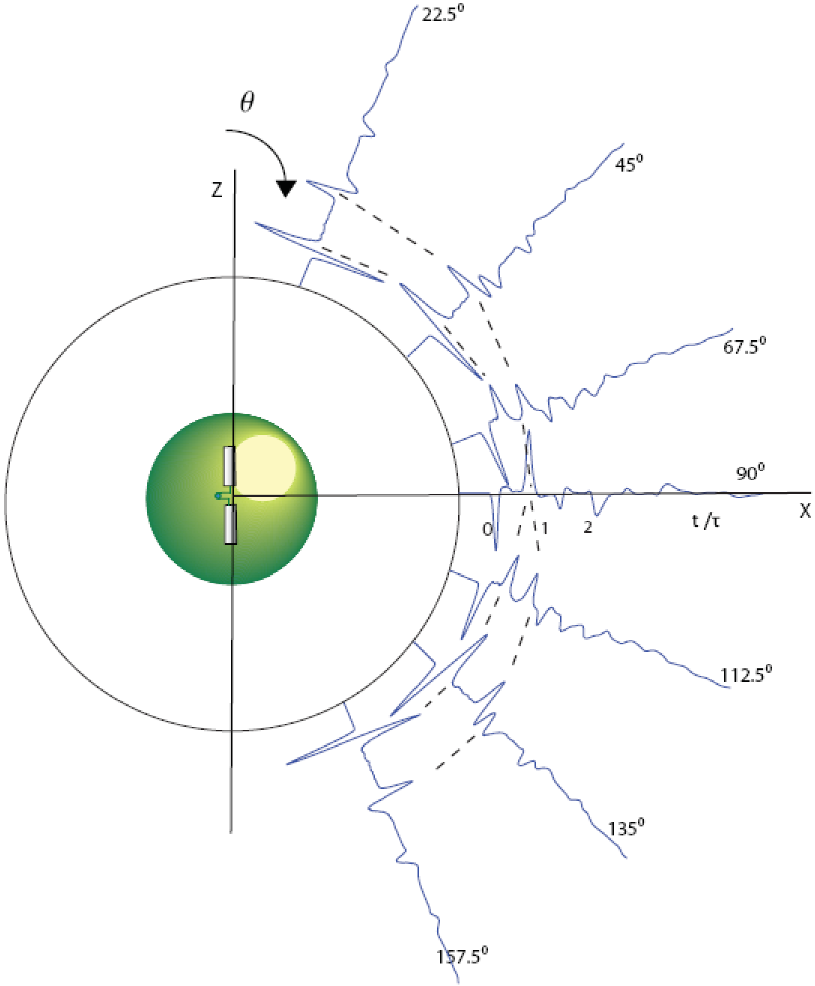

DIPOLE ANTENNA

Length study. Dipole 1 GHz

- Radiation patterns

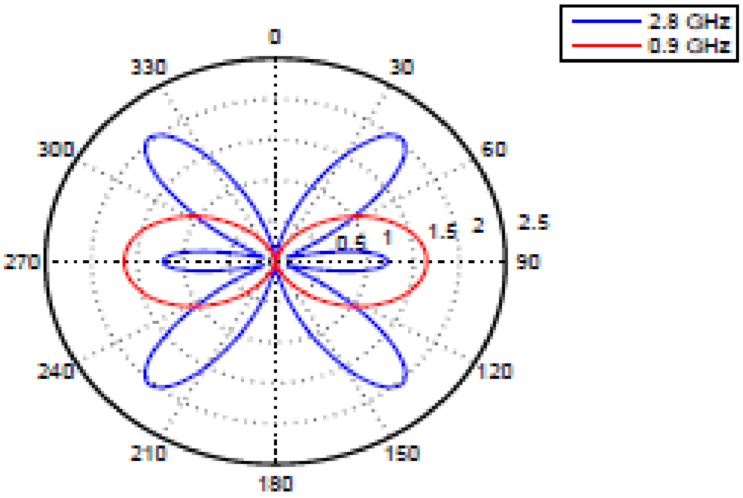

Dominant Poles 1st and 2nd resonances.

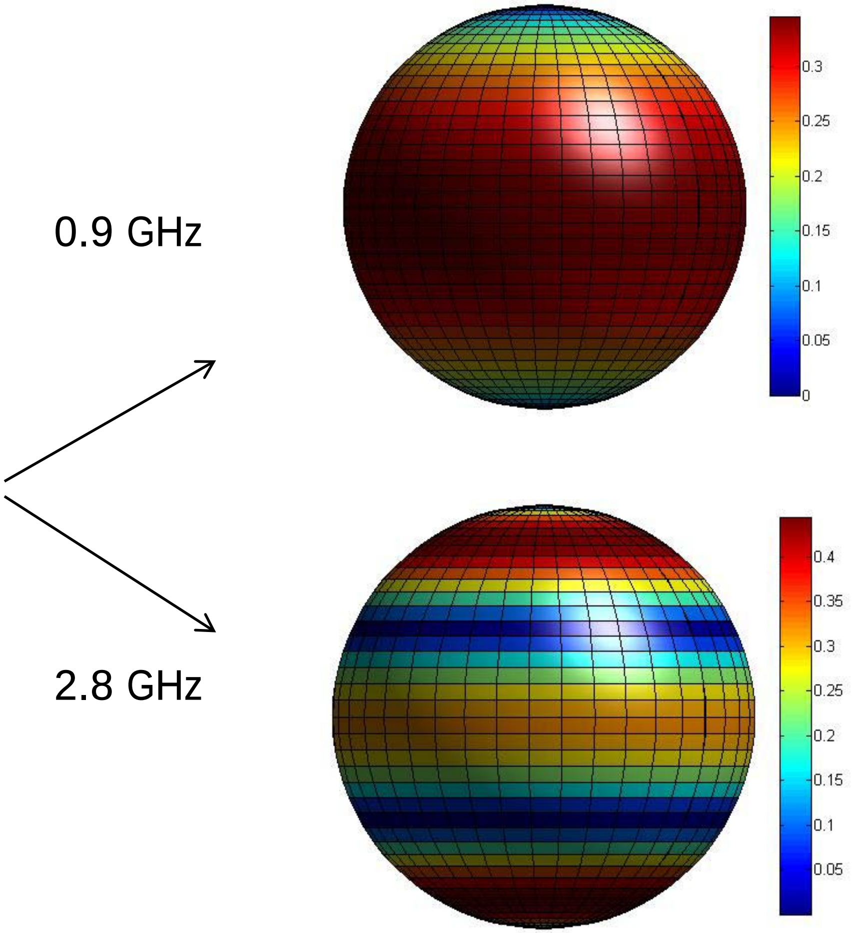
0.9 GHz

2.8 GHz

DIPOLE ANTENNA

Radius study.

- Radius wire parameter

Dipole-length $l = \lambda/2$ (m)	Operating Frequency (GHz)	l/d ratio
0.025	6	75
0.025	6	50
0.025	6	25

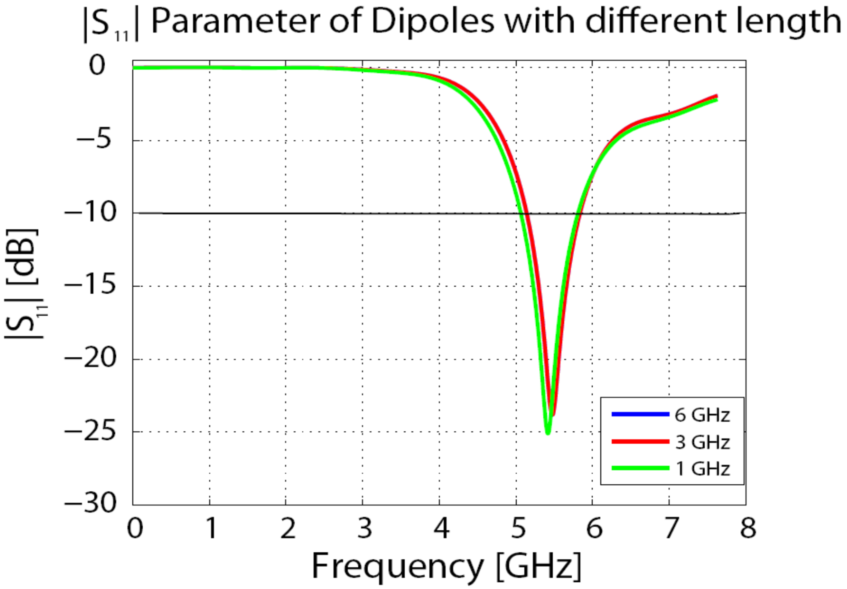
$|S_{11}|$ Parameter of Dipoles with different length

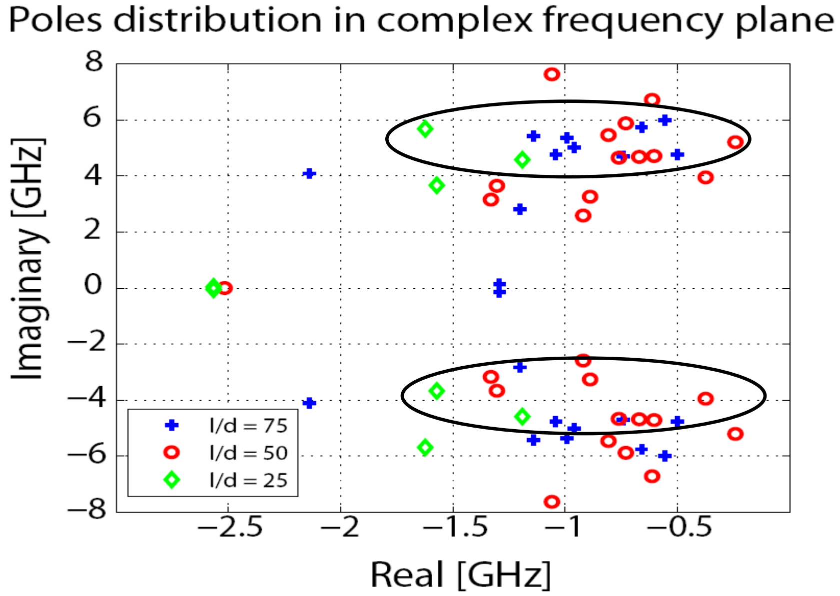
Poles distribution in complex frequency plane

BOW-TIE ANTENNA

Flair angle study.

- Bow-tie antenna placed in XY-plane.
- Selected to operate at 3 GHz

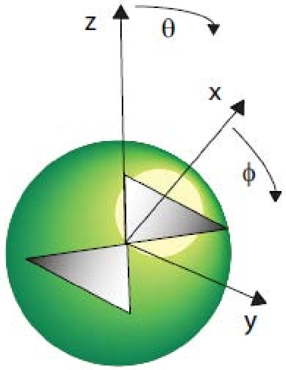

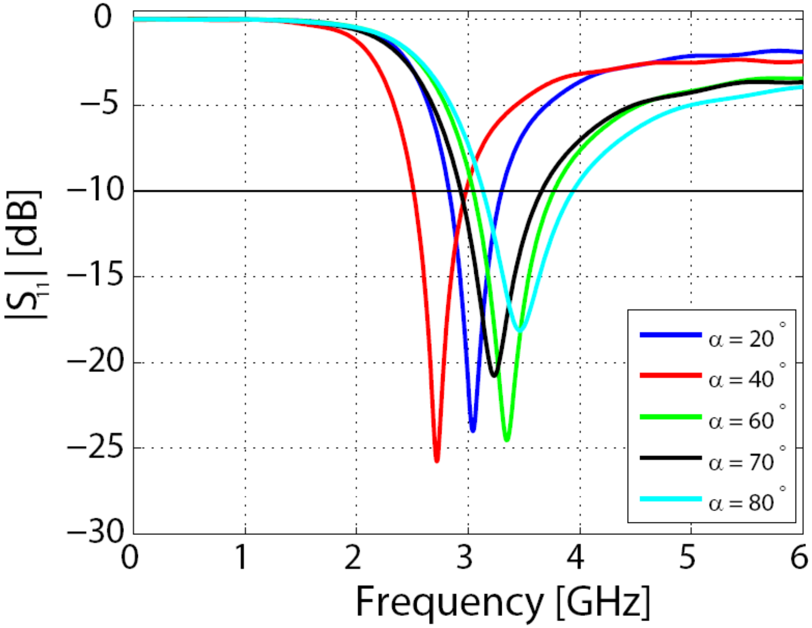
|S_{11}| Parameter of Dipoles with different length

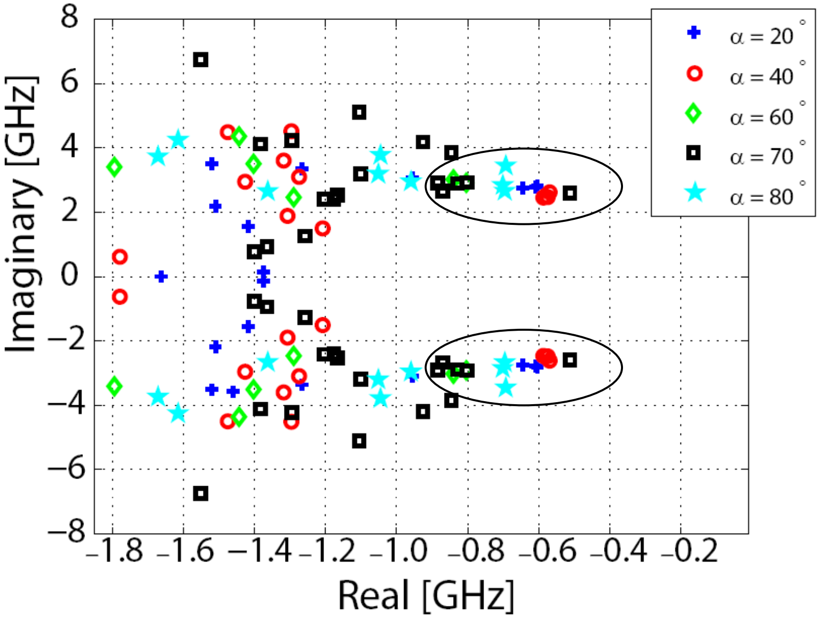
Poles distribution in complex frequency plane

BOW-TIE ANTENNA

Flair angle study. Transient radiation.

- Spatial distribution on XY-plane. 20º flair–angle Bow-tie

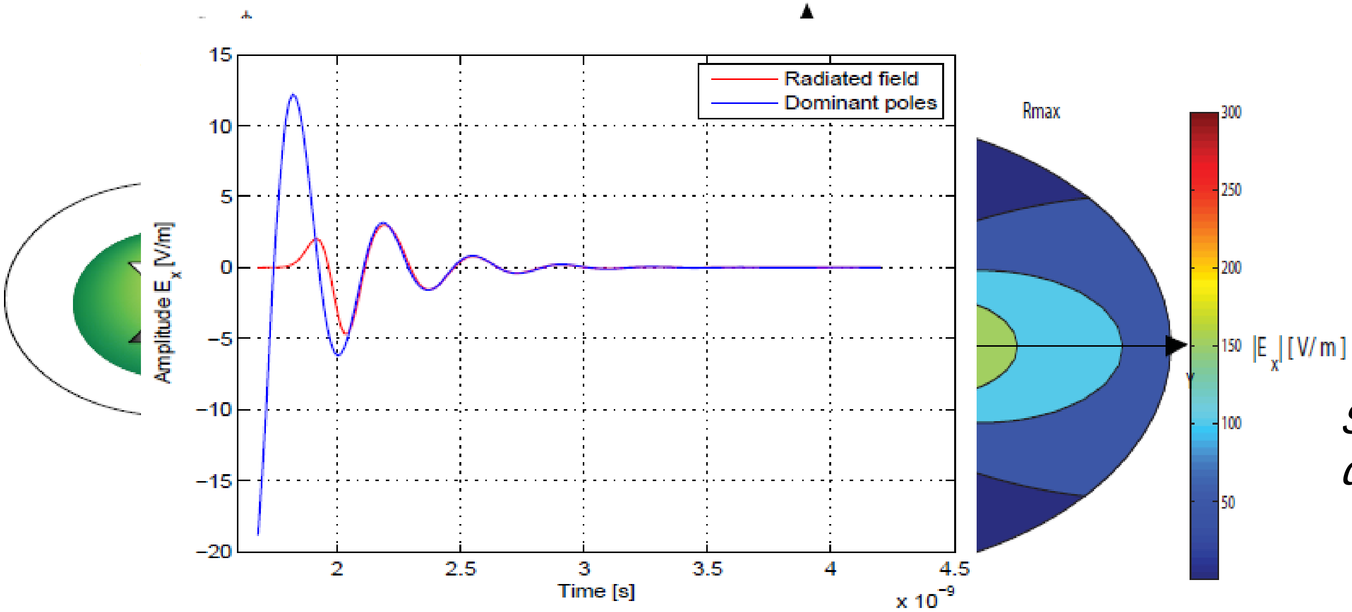

Time domain

Frequency domain f=3GHz

Spatial decay: 1/r

Negligible field along X axis and maximum radiation along Y axis.

BOW-TIE ANTENNA

Flair angle study. Transient radiation

Spatial distribution similar for each antenna case.

Maximum radiation along the end-fire direction.

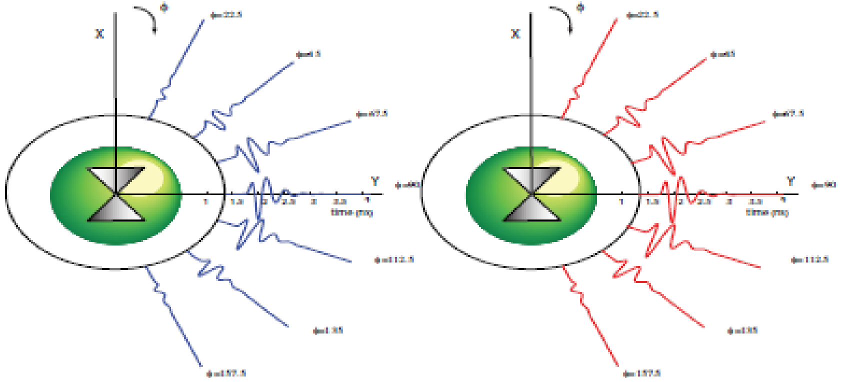

(a) $\alpha = 20^\circ$ (b) $\alpha = 40^\circ$

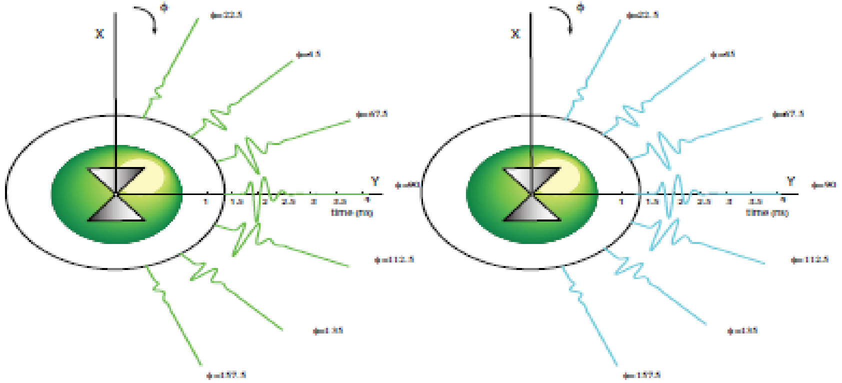

(c) $\alpha = 60^\circ$ (d) $\alpha = 80^\circ$

LOOP ANTENNA

Loop radius study.

λ (m)	Circumference $kA = C/\lambda$ (λ)	Circumference (m)
0.1	0.5	0.05
0.1	0.6	0.06
0.1	0.8	0.08
0.1	1.1	0.11
0.1	1.5	0.15
0.1	2.2	0.22

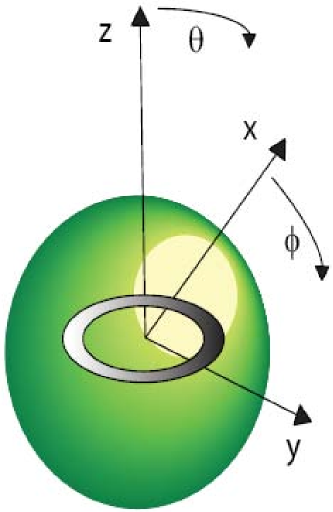

- Loop antenna placed in XY-plane.
- Selected to operate at 3 GHz.
- $\Omega = 2\ln(2\pi a / b) = 12$

LOOP ANTENNA

Loop radius study.

- $|S_{11}|$ parameter and poles distribution in complex plane

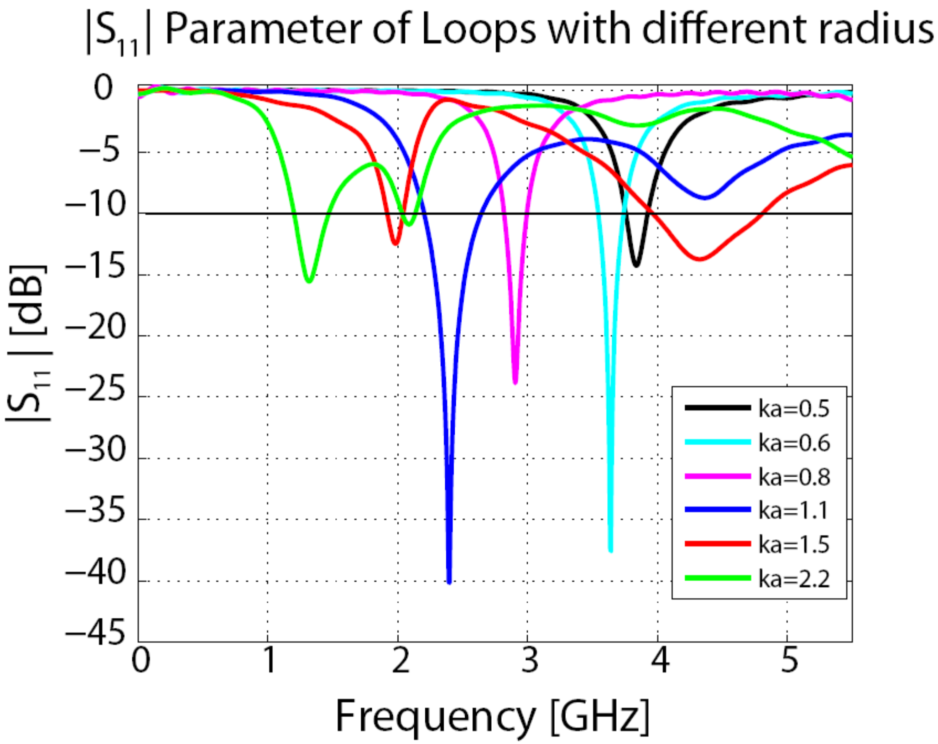

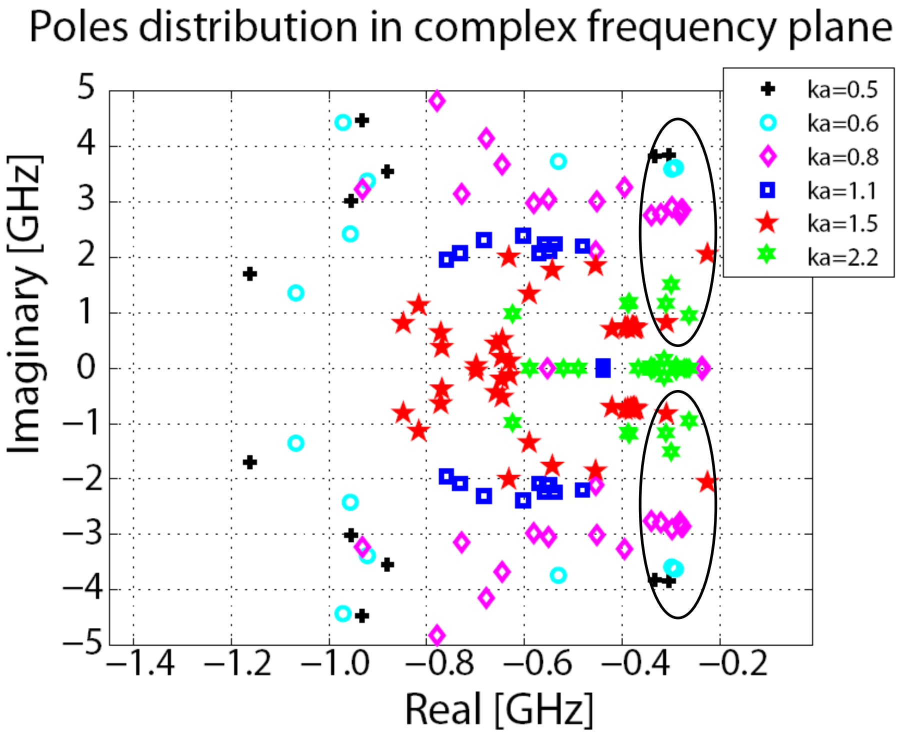

CONCLUSIONS

- Implementation of a new formalism, using **commercial** available **software**, for representing radiated field as **outgoing non-uniform spherical waves** which **attenuation** is given by the **radial distance** and the **real part** of the complex poles.

- Characterization of basic canonical antennas such as **dipole, bow-tie and loop antennas** gaining **physical insight** into the electromagnetic behavior.

- Relationship between complex natural processes and physical characteristic of the dipole antenna.

FUTURE WORK

- Further investigation considering more sophisticated antennas .
- Extraction of the complex resonant from a limited set of experimental data.
- Investigation of the antenna response itself deconvolving the excitation signal (Gaussian pulse).

$$y(t) = h(t) * x(t)$$

Thank you for your attention!